Large-Scale Analysis of Microtubule Pharmacology via Phosphoproteomics and High-Content Imaging

Large-scale Analysis of Microtubule Pharmacology via Phosphoproteomics and High-content Imaging

A dissertation presented

by

Javier Jesus Pineda

to

The Committee on Higher Degrees in Chemical Biology

in partial fulfillment of the requirements

for the degree of

Doctor of Philosophy

in the subject of

Chemical Biology

Harvard University

Cambridge, Massachusetts

June 27, 2018

Page intentionally left blank

Dissertation Advisor: Dr. Timothy J. Mitchison Javier J. Pineda

Large-scale Analysis of Microtubule Pharmacology via Phosphoproteomics and High-content Imaging

Abstract

The dynamic instability of microtubules is a critical phenomenon that regulates several biological processes. Chemical perturbation of microtubules disrupts these processes and is known to stimulate phosphorylation of downstream substrates. Despite decades of research into microtubule pharmacology, unanswered questions remain regarding the relationship between anti-tubulin drugs and downstream signaling and phenotypes. The following work addresses and answers three outstanding questions regarding the biology of anti-tubulin drugs. It first addresses an important metric for anti-tubulin drug efficacy – site occupancy – and relates classic drug-induced phenotypes to drug occupancy of the taxane site on microtubules in live cells and tissues. The data presented suggest that, when considering site occupancy, the spindle-assembly checkpoint is relatively insensitive to microtubule-stabilizing drugs. Next, after probing the relationship between site occupancy and drug-relevant phenotypes, work is described which utilized mass spectrometry-based phosphoproteomics to elucidate differences in phospho-regulation induced by microtubule-stabilizing and destabilizing drugs. Analysis of this data revealed a large wave of rapid phosphorylation that was common to both classes of drug and highlighted the prominent activity of a protein phosphatase stimulated by microtubule destabilization. Furthermore, the data demonstrated a surprising increase of JNK activity without additional JNK activation in response to microtubule stabilization. Lastly, after comparing drug effects on phospho-signaling in an averaged cell population, work is presented which involved high-content analysis at the single-cell level to elicit information regarding cell heterogeneity in anti-tubulin drug responses. This required development of a novel approach to quantify microtubule dynamics, namely EB3 comet counting in segmented single cells. The data revealed drug-induced single-cell heterogeneity with respect to microtubule dynamics upon treatment with a panel of drugs. Moreover, this occurred in the presence of a pan-efflux pump inhibitor, suggesting that drug-induced heterogeneity can occur independently of drug pump action. This biological finding, along with those mentioned above, is likely important for understanding the therapeutic efficacy of these drugs in cancer chemotherapy.

Table of Contents

Acknowledgements

Reflecting on my PhD years, I have come to learn that I am a person that does not shy away from the help of others. With that being said, I am indebted to all the people I sought for advice, and who supported me and aided me in one way or another, ultimately allowing me to come to the point of even writing this thesis.

I firstly thank my thesis advisor, Dr. Tim Mitchison, who has always been a very supportive and engaging mentor, encouraging me to try my hand at the latest cutting-edge technologies while at the same time giving me the perfect amount of direction: enough independence that I might learn from my own successes and failed experiments but also enough guidance that I might never stray too far off the scopes of my projects. In the same breath, I will also thank my dissertation advisory committee – Dr.s Nathanael Gray, Peter Sorger, and Jagesh Shah – for their critical advice in advancing my projects, and also for their vital role in helping me experience the scene of science in the private sector, which I am now drawn to and intend to take part in.

I am additionally indebted to my lab mates, and especially the post-docs. I believe that the number of failed experiments during my PhD was significantly reduced thanks to their guidance. Zoltan Maliga, I owe you so much for your time, patience, and general care for me as a mentee, colleague, and friend. I have always looked up to you and find your advice rich with insight and wisdom. I cannot imagine what kind of scientist I would be today without your mentorship. Jui-Hsia Weng, you arguably had the most open and discerning mind for what were good ideas, bad ideas, or tractable vs. intractable ideas. You always had the second opinion which impacted the work I would perform over the following weeks. Collectively, you and Zoltan probably shaved a year off the duration of my PhD. Yuyu Song, I always enjoyed working with you and looked to you as an older (and wiser) sister. Matt Sonnett, I thank you for helping me get started in my mass spectrometry-related work. James Pelletier, I am truly thankful for your help and initiation in carrying out the feat of a lab retreat, such that it could happen two years in a row. To the rest of the current lab members – Ivana Gasic, Kenichi Shimada, Sergine Brutus, Peter Koch, and Christine Field – I have learned something from all of you and I have enjoyed spending my PhD with you; it made it worth all the hard work to have such great lab mates. Thank you also to those who assisted our lab incessantly – Kathy Buhl and

other members of the lab-ops team. I am also indebted to past lab members – Stefan Florian, who taught me how to work with human cells, Aaron Groen, who gave me advice for joining the Mitchison Lab, as well as Keisuke Ishihara and Ani Nguyen, who were the past graduate students I overlapped with at the start of my PhD.

I am also thankful for the friendships I have developed within the Harvard Systems Biology community. Marc Presler, I am indebted to you for your critical help in supplementing my mass spec training such that I could perform phosphoproteomics sample prep. I also enjoyed our many scientific (and non-scientific) conversations, the critical mind you brought to those conversations, and our common enthusiasm for jazz and trumpet. To Victor Li, Sharon Wang, Evi Van Itallie, and Jose Reyes, I enjoyed all of our interactions, whether in the cell culture room or in the kitchen during lunch time. John Biddle, it was great knowing you during the final year of my PhD and sharing our common love for our alma mater (University of Notre Dame), though I wish we could have overlapped more! Naren Tallapragada, I doubt I will meet many people quite as intelligent. I always knew one thing: if you knew the answer to any of my scientific questions, you knew the answer comprehensively and had the ability to teach it to me. I enjoyed working with you, whether as teaching fellows or as collaborators. To the members of the Laboratory of Systems Pharmacology –Matt Berberich, Robert Everley, Clarence Yapp, Marian Kalocsay – I am so grateful for having had the opportunity to work with each of you. Thank you for your patience in helping me with either microscope trouble or mass spectrometry-related trouble shooting.

To all of my PhD program mates (i.e. those in the Chemical Biology PhD Program), I am grateful for all of our friendships and interactions, which have enriched my PhD experience. Zhi Wei Tan, I am thankful for our board game nights which brought about much needed work-life balance. Thank you also for taking the initiative to gather a group of regular attendees to play volleyball at Harvard Medical School. On that note, I am also thankful to Liz Ransey and Marina Orman who allowed me to be their volleyball coach a couple years ago for intramural volleyball. To Yolanda Huang and Nienke Moret – I will cherish our talks about PhD life. To the rest of my classmates - Daniel Cohen, Zebulon Levine, Haoxin Li, Dave Remillard, Andy Shumaker, Matt Sonnett, Emma Spady, and Blake Tye – I am happy that I had the opportunity to get to know you over the past five years.

I would also like to acknowledge those whose guidance was instrumental in helping me choose to even pursue a PhD. These include my former undergraduate research advisors, Dr. Olaf Wiest and Dr. James Bradner, as well as my mentors at the Broad Institute who provided much guidance about graduate school during my undergraduate summer internships – Dr. Bruce Birren, Eboney Smith, and Francie Latour.

Finally, I would like to thank my family for their incredible support during the past five years and my life in general. This support started with my parents, Gloria and Ricardo Pineda, who always encouraged us to make the most of our education. I thank my oldest brother Luis for demonstrating this for the rest of the Pineda kids by going straight to university (UCSD) after high school. I thank my sisters, Vanessa and Sr. Agnes Maria, O.P., who have always provided additional encouragement for their younger brothers, me included. To my brother, Fr. Ricardo, C.P.M., I am indebted to you for your own solid efforts, which motivated me to also do my best in school, wanting to be just like my older brother. I am sure that I would not have excelled in school quite as much if it were not for the solid model you gave me to follow.

To my wife, Louen Pineda, I cannot properly express in words how much I appreciate your love and support over the past couple years. As soon as you came into my life, I saw a wave of additional motivation come upon me such that my productivity in lab increased, as did my passion for science – I know this is not coincidence. You played the most critical role during this time in supporting my endeavors and taking interest in my experiments, and sometimes giving me the solutions to make them work, whether knowingly or unknowingly. I thank you for your great patience as I continuously thought about experiments at home, and while I wrote this thesis and prepared to defend it. At this point, I cannot imagine having to complete my PhD without you by my side, and I am excited at the thought of what we will accomplish together in the future.

To my baby boy in my wife's womb. The thought of meeting you brings me great joy and excitement. You are a product of love, God, and science, and your existence marks the beginning of our family life.

How much better to get wisdom than gold,
To get insight rather than silver!

Proverbs 16:16
New International Version

Chapter 1

Introduction

1.1 Preface

1.1.1 Drugs before proteins

The beginnings of protein biochemistry date back to the 18th century in France when a French chemist, Comte de Antoine Fourcroy, isolated a nitrogen-containing compound from plants with similar properties to egg albumin[1]. By the early 19th century, it was appreciated that protein was a chemical compound, though much larger than compounds chemists were accustomed to working with. By the middle of the 20th century, it was understood that many proteins exist and that they contain spiral structures – courtesy of Linus Pauling[2]. Today, the concept of the protein has changed from being a single, large, chemical compound to being thousands of unique, globular structures, which are dynamically made, degraded, and modified, and which are present in every living cell on Earth.

In stark contrast, the first drugs that we have record of were prescribed in the Egyptian empire ca. 1550 BC or even earlier. The autumn crocus plant, for example, is described in ancient Egyptian texts as being used to treat inflammation[3]. The active ingredient of this plant, which is relevant to this thesis, is colchicine. Unbeknownst to ancient Egyptians, this drug would still be used more than 3000 years later for the same purpose.

Until recent years, drugs have always been discovered before their protein targets, whether for the treatment of inflammation (e.g. colchicine), diabetes (e.g. metformin), or cancer (e.g. paclitaxel). Most commonly, these drugs have been extracted from trees, plants, marine sponges, or microbes. Only after decades, if not millennia, of using these drugs are we now starting to understand how they work on the mechanistic level, enough to finally design our own drugs. As we have continued to study drugs, they have begun to serve, not just as medicines necessary for human comfort and survival, but as chemical tools that teach us more about biology than we ever knew before – drugs that target microtubules are no exception, as it was through the use of colchicine that tubulin was discovered to be the subunit of microtubules[4]. This is the overarching theme of chemical biology, the lens through which I view microtubule biology, and the light that has guided my study of the biology surrounding microtubule pharmacology.

1.2 Principles of tubulin biology

1.2.1 From protein to polymer

Tubulin is a 50 kDa protein that comes in several isoforms and rarely exists by itself. In the cell, monomeric α- and ß-tubulin are brought together by protein chaperones directly after synthesis into a stable heterodimeric structure[5–8]. Tubulin is also a GTPase protein, in that it can hydrolyze guanosine triphosphate (GTP) into guanosine diphosphate (GDP). Tubulin is an inefficient GTPase, however, in that the GTP nucleotide bound between the α-ß interface only serves a structural role and is never hydrolyzed[9,10]. At the same time, tubulin is a self-sufficient GTPase in that it activates its own GTPase activity – GTP hydrolysis at the end of ß-tubulin is catalyzed upon association with another tubulin heterodimer[11]. That being said, hydrolysis occurs when tubulin self-assembles into a microtubule polymer.

Microtubules (MTs) are tubular structures made up of hundreds of tubulin dimers. They are polar structures, in that the α ends of tubulin dimers reside at the so-called *minus end* whereas the ß ends reside at the *plus end*. MTs are made up of multiple protofilaments, each of which is a long filament of tubulin dimers strung together longitudinally. Typically, an MT will contain thirteen laterally-bound protofilaments[12]. In order for a tubulin dimer to be incorporated in an MT, however, it must be GTP-bound at its ß end. In other words, it is not energetically favorable to incorporate a GDP-bound tubulin dimer into MTs as this would generate an unstable structure. In line with this reasoning, when MT-incorporated ß-tubulin hydrolyzes its GTP, the structure surrounding the hydrolysis becomes unstable and, eventually, the lattice disassembles[13]. Note that disassembly only occurs once GTP hydrolysis in the lattice reaches the plus end. If GTP hydrolysis has not occurred at the plus end, then this population of tubulin dimers serves as a protective cap (or “GTP cap”) that keeps the MT from falling apart like a peeling banana[14].

MT nucleation is slow compared to assembly and disassembly. Nucleation of MTs occurs at a microtubule-organizing center (MTOC), which generally resides at the centrosome[15], though MTOCs can also be recruited to the Golgi[16]. At the MTOC, another tubulin isoform, γ-tubulin, forms a complex with other proteins to form a conical structure known as the γ-tubulin ring complex (γ-TuRC), which has 13-fold symmetry and thus acts as a scaffold to catalyze tubulin growth on the plus end[17]. The minus end of the nucleating/growing MT is thus protected from disassembly by the γ-TuRC.

1.2.2 Dynamic instability and the role of microtubule-associated proteins

One fascinating aspect of MTs that astounded the microtubule community in 1984 is their intrinsic *dynamic instability*, or tendency to grow and shrink stochastically[18]. The now-conventional model of MT dynamics is one that is comprised of four primary parameters. *Growth* and *shrinkage* of MTs are self-explanatory concepts, though it should be noted that these can occur with varied rates. Furthermore, growing MTs possess a cap of GTP-bound tubulin dimer at their plus ends whereas shrinking MTs do not. *Catastrophe* is described as the event during which a growing MT stalls growth and begins to disassemble whereas *rescue* is the term employed when a shrinking MT stalls disassembly and begins to reassemble. The dynamic instability of MTs is critical for several cell processes, most notably cell division and motility, and is largely dependent on cytosolic concentration of tubulin dimer – the greater the local concentration of soluble tubulin dimer, the more likely an MT is to grow.

The dynamics of MTs are further modulated by regulatory proteins. Proteins that have a stabilizing effect on MTs are called *microtubule-associated proteins* (MAPs). These proteins induce stability via direct interaction with the MT lattice[19]. Other proteins bind to the GTP cap at the plus end of growing MTs and are therefore called *plus-end tracking proteins* (+TIPs). These +TIPs also have a stabilizing effect on MTs[20]. Additionally, there are proteins that serve to destabilize MTs. Among these are *catastrophe factors*, which bind to MTs or soluble tubulin dimers[21,22], and *severing proteins*, which can literally cut MTs in half and thereby induce disassembly[23].

1.2.3 The role of post-translational modifications in microtubule dynamics

To add an extra layer of complexity, tubulin and its associated regulatory proteins are chemically modified *in vivo* by post-translational modifications (PTMs). Tubulin can be modified by a plethora of PTMs, most of which occur on the exposed C-terminal tails of MT-incorporated α- and ß-tubulin and some of which affect interactions with MT-regulatory proteins[24]. Detyrosination, which occurs at the C-terminal residue, provides stability to MTs by preventing kinesin-mediated disassembly[25]. Polyglutamylation, which also occurs at the C-terminal residue, regulates interactions with both MAPs and severing enzymes in a tunable

manner[26–29]. Acetylation also occurs on MT-incorporated tubulin, though this generally occurs on a luminal facing lysine – this PTM is typically associated with stable MTs[24]. Other tubulin PTMs exist – phosphorylation, glycosylation, polyamination, arginylation, methylation, palmitoylation, ubiquitylation, sumoylation – though the functionalities of these modifications are not fully understood[24].

MT-regulatory proteins are also post-translationally modified. Phosphorylation is arguably the most ubiquitous – and interpretable – PTM that modifies these proteins and, consequentially, MT dynamics. Most studies support the idea that phosphorylation acts to inhibit the interaction between MTs and these regulatory proteins. For example, phosphorylation of MAPs (e.g. MAP2, MAP4) tends to weaken the affinity of MAPs toward the negatively charged MT lattice, and this ultimately has a destabilizing effect on MTs – this is especially the case when the phosphorylation occurs within the MT-binding domain of these MAPs[30,31]. Conversely, phosphorylation of catastrophe factors such as stathmin inhibit the protein's ability to sequester tubulin dimers, which has a stabilizing effect on MTs[32–36]. The effects of these biological modifications on MT dynamics, however, pale in comparison to the effects of MT-targeting small molecule compounds.

1.3 Principles of tubulin pharmacology

1.3.1 A myriad of tubulin drugs for a highly druggable protein target

When tubulin was revealed to be the protein subunit of MTs in 1967, it was concomitantly discovered that colchicine was a tubulin-binding, or anti-tubulin, drug[4,37]. Now anti-tubulin drugs exist with a wide variety of scaffolds, several modes of binding, and different mechanisms of action. These drugs all have one thing in common, however – they inhibit dynamic instability, either by stabilizing or destabilizing MTs. At higher concentrations these drugs can fully polymerize or depolymerize MTs, while at lower concentrations it is conventionally accepted that these drugs can inhibit MT dynamics without affecting MT polymer amount. The latter claim is based on *in vitro* experiments performed with reconstituted *bovine* brain MTs or after lysis of cells arrested in mitosis[38–40]. It would be worth revisiting this claim with more robust modern technologies, however, as data contained in this thesis may challenge this conventionally accepted hypothesis, especially with regard to interphase MTs (see Chapter 2).

To date, there are 6 known drug binding sites on tubulin dimers – the three latest sites were discovered during the tenure of this dissertation work (i.e. within the past 4 years). The first site, termed the *colchicine site*, resides at the α-ß interface of a soluble of a soluble tubulin dimer – colchicine does not bind directly to MTs[41]. This interaction serves to lower the effective concentration of GTP-bound tubulin in the cytosol, which inhibits MT assembly, allows GTP hydrolysis to catch up to the GTP cap, and ultimately results in greater MT instability. Other drugs that bind to this site include nocodazole[42], a routinely-used synthetic drug, and combrestatin-A4[43], which somewhat resembles colchicine but has a faster off-rate with respect to tubulin binding[44].

The second site, termed the *taxane site*, is where paclitaxel and other taxanes bind to ß-tubulin on the inner lumen of MTs[45]. Drug binding at this site serves to stabilize GDP-bound portions in the MT lattice[46], which prevents disassembly at lower concentrations of drug and induces MT polymerization at higher concentrations. The epothilone class of drugs also binds to this site, though with a slightly different different binding mode[47].

The third site is the *vinca site*, so called because it was first discovered to interact with the vinca alkaloid class of drugs[48], which includes vinblastine and vincristine, two drugs widely used in the treatment of child and adult cancers. Vinca site drugs bind to the very plus-end of MTs where they serve as a molecular wedge to inhibit further tubulin incorporation. When GTP hydrolysis catches up to the GTP cap, MTs are destabilized. That being said, these drugs have also been found to sequester tubulin dimers into helical oligomers that are incompatible with MT incorporation[49], though this may be a secondary effect[50]. Eribulin, another clinically approved therapy for breast cancer, also binds to the vinca site[51]. Surprisingly, there is one vinca site drug that is known to stabilize MTs[52].

The fourth binding site, the *maytansine site*, was discovered recently in 2014 and is adjacent to the vinca site[53]. In contrast to vinca site binders, structures of maytansine in complex with tubulin suggest that the drug may have the same affinity for the plus ends of MTs and soluble tubulin dimer[53]. In the latter case, drug binding could lower the effective concentration of GTP-bound tubulin in the cytosol and inhibit MT assembly like colchicine binders. Although only a few drugs are known to bind this site, one is currently in Phase II clinical trials for colorectal cancer (i.e. PM 060184).

The fifth binding site, like the taxane site, is one that stabilizes MTs at low concentrations but polymerizes MTs at high concentrations. It is now known as the *peloruside site* and, unlike the taxane site, the peloruside site resides on the outer lumen of MTs[54]. Currently, few other drugs are known to bind this site, which was discovered just a few months after the maytansine site. Further study of this site is partially inhibited by the lack of commercial availability of representative ligands.

All binding sites mentioned thus far reside on ß-tubulin. The sixth and final known binding site is therefore unique in that it resides on α-tubulin. It is currently known as the *pironetin site* as the natural product pironetin is the only known scaffold to bind to this site, which destabilizes MTs[55]. Another unique aspect about the binding mode of pironetin is that it covalently binds to α-tubulin via cysteine S316. Currently it is proposed that pironetin either binds to soluble tubulin dimer, and thus lowers the effective concentration of GTP-bound tubulin, or binds to MT-incorporated tubulin that resides at minus-ends, which could inhibit addition of further tubulin dimers at the minus ends[56].

1.3.2 Anti-tubulin drug effects on mitosis and cell division

It has long been known that disruption of MT dynamics is toxic to mitosis. MTs are known to be much more dynamic in mitosis compared to interphase[57], which makes mitotic MTs especially sensitive to pharmacological disruption. In the vast majority of cases where cultured cells have been treated with MT-targeting drugs, the cells have died after a prolonged mitotic arrest due to activation of the spindle-assembly checkpoint (SAC)[58]. In these cases, the SAC is activated because disrupted MT dynamics inhibit the cell from correctly attaching all chromosomes to the mitotic spindle via kinetochores. In some cases, the mitotic cell is unable to even form a normal spindle[39].

Unsurprisingly, it has been postulated for decades that MT-targeting drugs possess therapeutic efficacy in cancer chemotherapy because of their ability to arrest cells in mitosis[59]. That being said, there are others who argue that therapeutic efficacy of MT-stabilizing drugs is more likely due to the ability of these drugs to induce chromosome missegregation and subsequent G1 cell cycle arrest, which occurs at lower nanomolar concentrations of drug[60]. The presence of micronuclei in cells is the most easily visualized

biomarker of this phenotype[39]. Along this line of reasoning, it has been recently demonstrated that the presence of micronuclei in a cell can stimulate immune signaling[61].

1.3.3 Anti-tubulin drug effects on cellular signaling

As mentioned previously, phosphorylation plays a major part in regulating MT dynamics, either by modifying tubulin itself or by modifying MT-regulatory proteins. For the last couple decades, however, it has also been known that MT-targeting drugs stimulate phosphorylation, in turn. It is known that the various MAPK signaling pathways are stimulated by MT-targeting drugs. For example, the c-Jun N-terminal kinase (JNK) has been shown to be activated in response to MT-stabilizing and destabilizing drugs in both cycling and non-cycling cells[62,63]. This suggests that MTs detect disruption of dynamic instability, not only in mitosis, but in interphase as well. Despite these findings, however, there seems to be little consensus on the nature of the stimulated MAPK signaling, which can have different kinetics and degrees of response depending on the cell type[62,64–66]. Other studies of phospho-signaling induced by these drugs have involved phosphorylation of a few MT-regulatory proteins, such as stathmin[67].

1.4 Tools for studying tubulin pharmacology

1.4.1 *In vitro* reconstitution

Among the classic tools for studying the effects of MT drugs, *in vitro* reconstitution of MTs has been in use for the past half-century[68–70]. Tubulin can be procured in abundance from bovine brains through a few polymerization/depolymerization cycles with high molarity piperazine-N,N′-bis(2-ethanesulfonic acid) (PIPES) buffer[70]. In this way, the extracted tubulin can be isolated from MAPs and then used in biochemical experiments. If desired, MTs can then be assembled *in vitro* and crosslinked for use in drug-binding experiments[71]. Classically, the binding affinities of MT-targeting drugs have been measured in this way, with the additional use of radioactively-labeled or fluorescently-labeled derivatives. The only drawback to using this method for drug-binding measurements is the fact that MTs differ between cell types, as do their response to MT-targeting drugs[72]. Therefore, depending on the drug and binding site in question, binding affinity and kinetics may differ from cell to cell.

1.4.2 High-content microscopy

Microscopy, like *in vitro* reconstitution, has been a standard method for analyzing MT biology. Many major findings in MT biology (e.g. dynamic instability) have been discovered using traditional microscopy. In addition, the development of microscopes such as the spinning disk confocal microscope[73], which uses pinhole technology to reject out-of-focus fluorescence, or the lattice light-sheet microscope[74], which uses a thin laser sheet to image samples with much less light exposure, afford much greater sensitivity in signal detection than traditional widefield microscopy. It is now possible to image the plus-ends of MTs using fluorescently-labeled +TIPs (e.g. EB1/3), which enables quantitative analysis of MT dynamics and can be combined with MT-targeting drugs[75]. Nevertheless, confocal microscopy, like traditional widefield microscopy, is very throughput limited – generally, scientists can only image a few conditions at a time.

In the last decade, high-content microscopy has offered a solution to improve imaging throughput. Now, with robust fluorescent readouts and appropriate software, one can image and quantify multiple phenotypes simultaneously in hundreds of conditions at once (e.g. using 384-well plates)[76]. High-content microscopes are designed to automatically shift from one well to another and can auto-focus with respect to a given image field and laser channel. In addition, one can use nuclear stains or other fluorescent markers that enable single-cell quantification, such that one can obtain information into the variability of a given biological phenomenon among single cells. The only potential drawback of high-content microscopy is that it is limited to the use of dry objective lenses, which naturally reduces signal-to-noise compared to state-of-the-art microscopes that use oil-immersion or water-immersion objective lenses. That being said, it is trivial to assess signal-to-noise. With the ability to image many replicates of control wells, one can calculate a *Z-prime* – also known as a *Z-factor* – which is a scaled value that measures the dynamic range of the assay signal and the data variation associated with single measurements[77]. The Z-prime can be measured by equation (1.1):

(1.1)
$$Z' = 1 - \frac{3\left(\sigma_p + \sigma_n\right)}{\left|\mu_p - \mu_n\right|}$$

Equation (1.1) makes use of the standard deviations (σ) and means (μ) of the positive and negative controls. Z-primes must be above 0 for high-content assay results to be useful, and Z-primes above 0.5 denote exceptional assays (i.e. ~12 standard deviations between positive and negative control).

1.4.3 Mass spectrometry-based (phospho)proteomics

Mass spectrometry (MS) has revolutionized proteomics in the past two decades. Instead of performing hundreds of laborious Western blots, one can now quantify thousands of proteins or peptides across multiple samples. The basic principle behind MS-based proteomics involves (electrospray) ionization, mass-detection (MS1), and subsequent fragmentation (MS2) of a peptide (via collision-induced dissociation) to obtain a distribution of smaller peptides, each of which retains a given mass-to-charge ratio, which can be detected and measure by the mass spectrometer. From the measured distribution of smaller peptides, it is possible to reconstruct the original sequence of the original ionized peptide. Based on this idea, genome sequencing has enabled the production of theoretical MS spectra for a given protein or peptide, which can be compared with the actual measured spectra to map the sequence of the original peptide[78–81]. In this way, even if the measured spectra are noisy, it is still possible to identify the original peptide through the comparison and the protein from which the peptide came. The concept of identifying proteins from constitutive peptides has been given the term *shotgun proteomics*.

There are certain drawbacks about MS-based proteomics, however, for which some solutions have been offered. For one, the peptide detection performed by MS is not inherently quantitative[82]. This is primarily due to the different efficiencies of ionization between peptides and differential detection bias across peptides. Due these issues, it is not possible to directly compare the absolute amounts of two different peptides. In addition, since the MS instrument cannot measure every single ionized peptide of a mixture due to time constraints, a peptide that is measured in one MS scan might not be measured in a technical replicate scan. The simple solution to this problem is that a peptide measured across two or more different conditions should be measured in the same MS scan. Stable isotope incorporation into cell media, and thus cellular proteins, was one approach that seemed to solve this problem (also known as SILAC)[82]. A similar approach was used to directly label proteins isolated from lysates through reductive

demethylation[83]. A more recent solution to this problem is the covalent labeling of isolated peptides with isotope-encoded chemical compounds (i.e. tandem mass tags, or TMTs[84]), which, though similar to reductive demethylation enables a greater degree of sample multiplexing[85,86] – currently, 11 samples can be multiplexed in a given sample set. The additional advantage of this technology is that the chemical tags possess identical mass until they are fragmented. Whereas additional multiplexing with the two previous technologies would complicate the MS1 scan, with the TMT technology, the same peptide across multiple conditions would be stacked as a single peak in the MS1 scan.

Another drawback that was not immediately solved by TMT-based multiplexing was that of signal distortion in the MS2 scan[87]. For this scan, a prominent peptide peak is isolated from the MS1 scan and subsequently fragmented to obtain the MS2 scan. In the MS2 scan, this peptide would be fragmented and sequenced, and the TMT ions would be used to quantify the relative peptide amounts between conditions. The problem is that completely different peptides with very similar mass would be co-isolated from the MS1 scan, leading to signal distortion from the latter peptide in the quantification of the former. The first solution offered for this problem involved an additional tandem MS scan (MS3)[87]. For this, the instrument would be programmed to isolate the most prominent peptide fragment (which would still retain covalently-labeled TMT) and then further fragment this peptide fragment (via high collision dissociation) to obtain a much purer measurement. Although this strategy proved successful, its implementation naturally reduced signal intensities. The strategy was substantially improved, therefore, by selecting multiple prominent fragments from the MS2 for the subsequent MS3, which is termed *multinotch selection*[88].

The principles of MS-based phosphoproteomics are similar to those mentioned above, though with additional caveats. First, phosphorylated peptides constitute 1-3 percent of peptides isolated from cell lysates. Therefore, to obtain useful data, it is necessary to procure a relatively large amount of lysate to being with. Not only that, but the isolated peptides must be enriched for phosphopeptides to bias the instrument into seeing mainly phosphorylated peptides[89–91]. Another difficulty is localizing the phosphate to the correct residue. This is due to the *neutral loss* problem, in which the phosphate falls off the peptide during the MS2 scan due to the phosphate bond being more labile than the peptide backbone[92]. With careful

fragmentation, it is possible to "get lucky" with most peptides and detect one fragment that still retains the phosphate bond, which allows localization, but this is not always possible.

To date, MS-based proteomics and especially MS-based phosphoproteomics have not been heavily used to study the pharmacology of MT drugs. That being said, one group used phosphoproteomics to study the response to nocodazole treatment across a panel of cancer cell lines[93]. This work, which focused on mitotic time-scales, did not use any isotopic labeling technology, however, thereby limiting its ability to make quantitative claims.

1.5 Summary of thesis

The pharmacology of MT-targeting drugs has been heavily studied over the past half-century. Much has been done to obtain information into the binding modes and affinities of these drugs and to quantitatively assess their effects on cellular phenotypes, signaling and MT dynamics. Nevertheless, there are a myriad of questions that remain unanswered with regard to their biological effects. High-content microscopy and MS-based phosphoproteomics are promising tools to answer these questions, but they have yet to see much use by the MT community. In this thesis, I was inspired by the promise of these two technologies to study unanswered questions in MT pharmacology.

For the work presented in chapter 2, my colleagues and I used high-content imaging to ask a critical pharmacological question: how much MT disruption is necessary to induce cellular phenotypes? Although this question sounds trivial enough to answer, previously it was impossible to answer quantitatively with respect to live cells. We conduct binding measurements of drugs in live retinal pigmented epithelial (RPE1) cells and use these to compute the amount of a given phenotypic signal – MT dynamics loss, mitotic arrest, chromosome missegregation – as a function of drug-bound sites on MTs (i.e. site occupancy). We were also able to make unprecedented quantitative comparisons in efficacy between drugs and in sensitivity among cell lines. We conclude by relating the site occupancy of paclitaxel to tumor regression in mice.

Chapter 3 details the TMT-based phosphoproteomics experiments I performed to globally compare the signaling changes induced by MT-stabilizing and destabilizing drugs. This approach enabled the quantification of several thousand phosphopeptides and revealed common and unique signaling to MT

stabilization and destabilization. More specifically, the work revealed the prominence of phosphatase action in the case of MT destabilization and demonstrated, for the first time, that MT stabilization can stimulate JNK activity without an increase in JNK activation.

Finally, in Chapter 4, I returned to high-content imaging and developed tools to study MT dynamics loss in the context of MT-targeting drugs at the single-cell level. This approach therefore afforded high-throughput and single-cell analysis of drug-induced effects on MT dynamics. My colleagues and I used a well-tolerated SiR-DNA dye in live cells to segment single cells, track cells over time, and score EB3 comets. Importantly, our approach made use of EB3 comet counting, as opposed to the conventional comet tracking, which requires higher frequency in image acquisition and limits image throughput. We demonstrate that MT-targeting drugs stimulate increased cellular heterogeneity with respect to MT dynamics and that this can occur independently of drug efflux pump action.

This thesis answers critical pharmacological questions regarding drugs that are thought to be well studied. It also reveals drug-induced phosphorylation-based signaling that may very well be relevant for the therapeutic efficacy of these drugs in the clinic. Lastly, this thesis show-cases newly developed approaches for answering throughput-demanding biological questions.

Chapter 2

Site occupancy calibration of taxane pharmacology in live cells and tissues

Javier J. Pineda, Miles A. Miller, Yuyu Song, Hallie Kuhn, Hannes Mikula,
Naren Tallapragada, Ralph Weissleder, Timothy J. Mitchison

2.1 Attributions

The following chapter has been reformatted from a manuscript that I submitted to *PNAS*. This manuscript delves into the pharmacology of MT-targeting drugs that bind to the taxane site. Using a live-cell ligand displacement assay, we were able to correlate taxane-site occupancy with MT-relevant phenotypes and derive new biological insights into MT pharmacology, such as the relative insensitivity of spindle-assembly checkpoint, or the variable biological efficacy of taxane-site drugs.

I designed and performed the ligand displacement assay that was pivotal for calibrating taxane-site occupancies with respect to the panel of drugs tested. I also designed and performed the other assays described below for measuring mitotic index, post-mitotic micronucleation, and EB3 comet loss in 384-well plate format. I also wrote all relevant Python and ImageJ coding for image processing and analysis. Dr. Miles Miller performed the ligand displacement assay in a HT1080 xenograft mouse model, and Dr. Yuyu Song performed the ligand displacement assay in a human neuronal model cell. Dr. Hallie Kuhn performed the paclitaxel dose escalation experiments on HT1080 xenograft mouse models. Dr. Hannes Mikula synthesized the SiR-tubulin probe, which was critical for the ligand displacement assay, and the SiR-eribulin probe, which we used to score mitotic index in HT1080 cells. Naren Tallapragada helped me formulate all of the statistical analysis necessary for procuring confidence intervals and I performed all of the necessary coding for implementing this. All experiments were performed with advice from Drs. Ralph Weissleder and Timothy Mitchison. I wrote the majority of the manuscript with edits from all authors.

2.2 Abstract

Drug receptor site occupancy is a central pharmacology parameter that quantitatively relates the biochemistry of drug binding to the biology of drug action. Taxanes and epothilones bind to overlapping sites in microtubules and stabilize the lattice. They are used to treat cancer and are under investigation for neurodegeneration. In cells they cause concentration-dependent inhibition of microtubule dynamics and perturbation of mitosis, but the degree of site occupancy required to trigger different effects has not been measured. We report the first live cell assay for taxane site occupancy, and relationships between site occupancy and biological effects across four drugs and two cell lines. By normalizing to site occupancy, we

were able to quantitatively compare drug activities and cell sensitivities independent of differences in drug affinity and uptake/efflux kinetics. Across all drugs and cells tested we found that inhibition of microtubule dynamics, post-mitotic micronucleation and mitotic arrest required successively higher site occupancy. We also found interesting differences, for example different sensitivities of the spindle assembly checkpoint to site occupancy between cells. By extending our assay to a mouse xenograft tumor model we measured the initial site occupancy required for paclitaxel to promote tumor regression as approximately 80 percent. Our data suggest that the most important cellular action of taxanes for cancer treatment is formation of micronuclei, which occurs over a broad range of site occupancies.

2.3 Introduction

A unifying concept in the pharmacology of protein-binding drugs is site occupancy, the fraction of specific binding sites in a population of protein receptors that is bound by drug. The concentration of unbound drug at a site occupancy of 0.5 is called the K_d, which is used to compare the affinity of different drugs to the same site. Site occupancy is especially important when comparing drugs with different effects on the receptor, e.g. full vs partial agonists. An efficacy parameter can be defined which quantifies the effect of a drug on receptor function at a given site occupancy, usually 0.5[94]. The most common methods for measuring site occupancy are ligand displacement assays in which unlabeled test ligands compete with an easily-measured labeled ligand for binding to the receptor. The labeled ligand is commonly radioactivity or fluorescence. If the K_d of the test ligand is known, the K_d of competing ligands can be inferred using the Cheng-Prusoff equation[95]. Ligand displacement assays were invented for pure proteins and cell surface receptors, but they can be extended to the interior of living cells, notably using fluorescence technology[96]. This allows direct measurement of biological actions as a function of site occupancy.

Here, we report a convenient fluorescent assay for measuring site occupancy of drugs that bind to the taxane and epothilone sites on microtubules (MTs) in living cells and use it to quantify biological effects as a function of site occupancy. The taxane site was defined using paclitaxel (Ptx), a natural product from the Pacific Yew tree[97]. Ptx and its derivative docetaxel are among the most active of solid tumor drugs and play a central role in combination chemotherapy[98]. Development of new taxanes continues, with interest in

derivatives with improved pharmacology and bioavailability[99], including improved brain penetration[100]. There is also great interest in clinical development of alternative scaffolds which bind to the taxane site[101]. Epothilones bind to an overlapping site in MTs and are naturally resistant to drug efflux pumps. One epothilone, ixabepilone (Ixa), is approved for cancer treatment[102].

Cancer is the only disease known to respond to taxanes or epothilones, but there has been significant interest in MT stabilization as a therapeutic modality in neurodegenerative disease[103]. Epothilone D (EpoD) is particularly brain-penetrant and demonstrated promise in rodent models of neurodegeneration[104,105]. Cancer and neurodegeneration are very different diseases and it seems likely that optimal therapeutic index might require different effects of drugs on the MT lattice. Given the interest in neuronal effects of taxane-site drugs, we tested if our approach could extend to a human neuron model.

The binding site for taxanes and epothilones on the interior of the MT has been well characterized at the atomic level[106,107]. Drug binding stabilizes the lattice, inhibits polymerization dynamics, and promotes ectopic MT nucleation. In dividing cells these effects cause chromosome missegregation at lower drug concentrations, and mitotic arrest at higher[60,97,108]. In non-dividing cells, they perturb organelle positioning, nuclear transport and stress signaling[109–112]. How these diverse cellular effects trigger tumor regression is controversial, with some authors favoring anti-mitotic mechanisms[113] and others interphase cell killing[112]. No prior studies systematically measured multiple phenotypic effects in parallel as a function of drug concentration or quantified the degree of site occupancy required to cause each effect.

Medicinal chemistry of taxanes and epothilones has mostly been guided by IC_{50} metrics for cell proliferation and not by biochemical K_ds or efficacy parameters[114,115]. Another important metric has been sensitivity to drug efflux pumps[116]. The most reliable biochemical K_d values come from the work of Andreu, Diaz and colleagues who measured displacement of a fluorescent taxane analog from cross-linked MTs using fluorescence polarization[117,118]. These data quantified binding separately from effects on MT stability, and the resulting data was used to profile biochemical efficacy across panels of taxanes and epothilones[119,120]. This work significantly advanced taxane-site pharmacology but was difficult to relate to biological effects in living cells. Here, we report a live-cell ligand displacement assay using the docetaxel derivative SiR-tubulin, a low-affinity, fluorogenic taxane-site ligand[121]. Using this assay, we measured, for

the first time, the degree of site occupancy required for perturbation of MT dynamics, chromosome missegregation and mitotic arrest for representative taxane-site drugs. Our work agrees with a classic measurement of saturable binding of ^{3}H-Ptx in living cells, though that study used only one drug and did not measure biological effect[122]. Furthermore, our fluorescence methodology is better suited to modern drug discovery pipelines since it does not require radioactivity.

2.4 Results

2.4.1 SirTub can be displaced by competing drugs in live cells

We pre-incubated RPE1 cells (Fig. 2.1A) and differentiated ReNcell VM human neurons (Fig. 2.1B) with 100 nM SirTub, then added 100 nM EpoB and performed live fluorescence imaging. In both cells lines, specific signal decayed completely within 10 minutes of adding competitor, indicating rapid and complete ligand displacement; Fig. 2.1C quantifies this observation for RPE1s. To minimize possible complications from drug efflux pumps, all experiments were performed in the presence of 10 μM verapamil, an efflux pump inhibitor[123]. Analysis of select data points without verapamil revealed lower SirTub signal, but competition results were not changed (data not shown).

Binding constants are usually measured after equilibrium has been achieved for both probe and test ligands. To determine equilibration time, we measured the kinetics of SirTub uptake and binding in RPE1 (Fig. 2.1D) and HT1080 cells (Supplementary Fig. 2.1). Automated thresholding and analysis allowed for ease of quantification (Supplementary Fig. 2.2). Signal from non-specifically bound probe was significant (~40% at our standard probe concentration). In Fig. 2.1D and all subsequent experiments 10 or more wells on each plate were reserved to measure non-specific probe binding. Average fluorescence signal in the presence of equimolar EpoB competitor (whose affinity is ~1,000-fold greater than that of probe) was subtracted from all values on the plate. Cellular uptake of SirTub was slow, and we were unable to saturate specific sites within 16 hours over the dosage range tested, which was capped at 1 μM to avoid DMSO artifacts. Unlabeled drugs reached equilibrium binding much faster at all concentrations (Supplementary Fig. 2.3A, B). We chose a SirTub concentration (800 nM) and pre-incubation time (10-11 hours) for all subsequent experiments where the signal was strong and changed negligibly during measurement. Lack

of true equilibrium in probe binding, and resulting uncertainty in true probe K_d, was not a problem. The much weaker affinity of the probe than test drugs meant that incomplete saturation with probe, or errors in probe K_d, had little effect on estimated test drug K_d. We verified this computationally by substituting a range of probe K_d values that were consistent with our data into the calculation of test drug K_d values, and found little effect, provided the K_d value was much lower for the test drug than the probe.

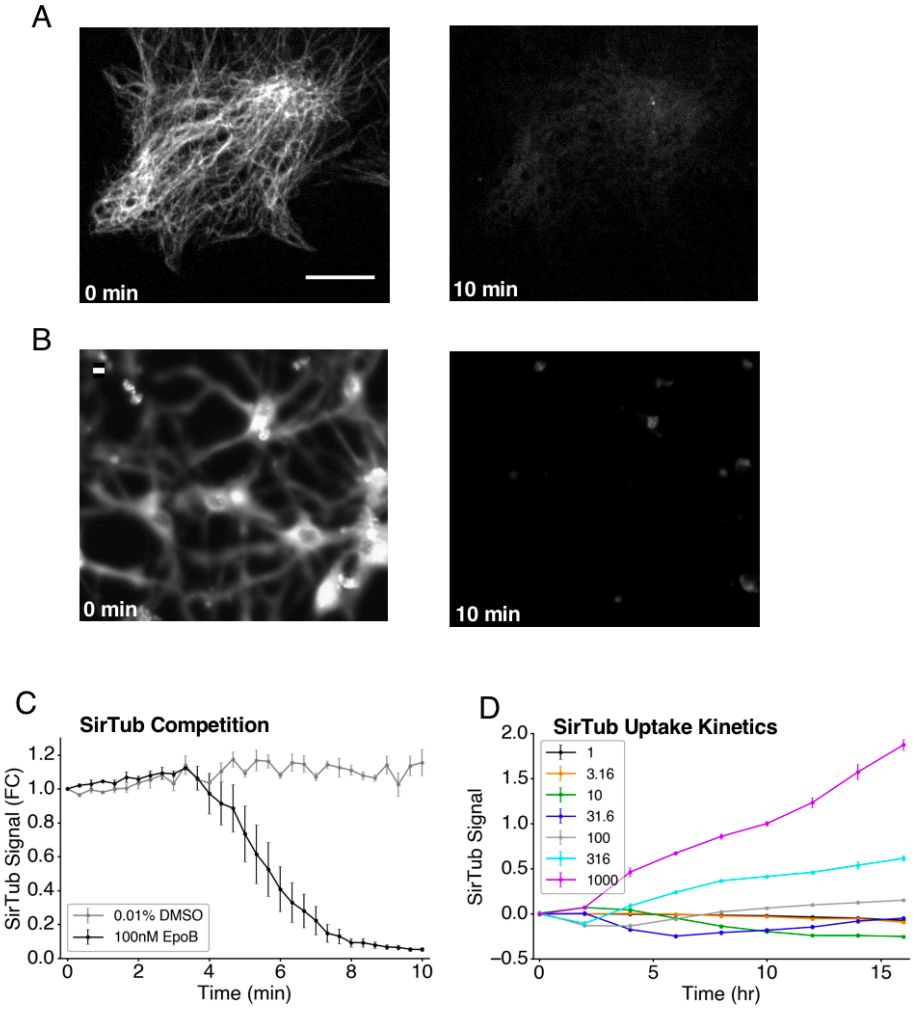

Figure 2.1. *SirTub can be displaced in live cells. (A) Representative images of RPE1 cells stained with SirTub, before and after treatment with a competing drug (EpoB). Cells were incubated with 100 nM SirTub for 2.5 hours, after which equimolar EpoB was added. Scale bar = 10 µm. (B) Representative images of ReN cells stained with SirTub, before and after treatment with EpoB. Cells were incubated with 100 nM SirTub for 10 hours, after which equimolar EpoB was added. Scale bar = 10 µm. (C) Quantification of SirTub displacement in A. SirTub signal was normalized by total cell area at every time point. FC = fold-change. (D) Time-course and titration of SirTub staining in RPE1 cells. Legend lists nanomolar concentrations of SirTub. Intensities were normalized by cell area as in C. Each data point was averaged from at least 9 wells.*

2.4.2 SirTub enables site occupancy calibration in multiple cell types

To calculate apparent K_ds of four drugs (Fig. 2.2A) from SirTub displacement curves we first evaluated a classic Cheng-Prusoff competitive displacement model with a constant number of binding sites (Fig. 2.2B) and found less than ideal fits to the data. We traced the discrepancy to induction of MT polymerization by test drugs, which caused an increase in binding sites when the test drug was titrated. This effect is evident from the slight upwards trend before the decrease in Fig 2C. It is characteristic of microtubule stabilizing drugs and was accounted for in previous models of Ptx binding in living cells[121,122]. We therefore added a simple, empirical model of drug-induced MT polymerization similar to the previous study[121]. Our final model made use of two critical equations:

(2.1)
$$K_{d,app}^{d} = \frac{[D_{out}]}{\frac{[MT]_{tot}[P_{out}]}{[PMT]K_{d,app}^{p}} - \frac{[P_{out}]}{K_{d,app}^{p}} - 1}$$

(2.2)
$$S_d = \frac{[D_{out}]}{K_{d,app}^{d} + [D_{out}]}$$

In equations (2.1) and (2.2), S_d denotes site occupancy of competing drug, $[D_{out}]$ denotes external drug concentration, $K^d_{d,app}$ denotes apparent binding constant of competing drug, $[MT]_{tot}$ denotes total MT polymer, $[P_{out}]$ denotes external SirTub probe concentration, [PMT] denotes concentration of probe-bound MT taxane sites (measured by fluorescence), and $K^p_{d,app}$ denotes the apparent binding constant of the SirTub probe. This model provided excellent fits (e.g. R^2 above 0.99 for all drugs in RPE1) to the ligand displacement data across four drugs and two cell lines (Fig. 2.2C, D). Our binding model does not account for possible differences in the concentration of unbound drug outside and inside the cell. Therefore, all our K_d estimates are apparent K_ds, not true biochemical K_ds. We believe our values are close to the biochemical K_ds because we used a drug efflux pump inhibitor to minimize concentration differences across the plasma membrane, and our values are very similar to measured biochemical K_ds for some drugs (see below).

We used our model to regress the data (Fig. 2.2C, D) and calculate apparent binding constants for four representative taxane site ligands: EpoB, EpoD, Ixa and Ptx (Fig. 2.2E, F). Fig. 2.2G and 2.2H show

curves for inferred binding site occupancy as a function of external drug concentration in two cell lines, RPE1 (untransformed, TERT-immortalized) and HT1080 (fibrosarcoma). EpoD and Ixa had almost the same apparent K_d values between the two cell lines according to our calculations (Fig. 2.2E and 2.2F), and these values were very similar to measured biochemical K_ds for binding to glutaraldehyde cross-linked MTs in pure protein assays[120]. Although our K_d estimates for Ptx differed substantially from the value obtained in the same study, they were in excellent agreement with the K_d of Ptx in living cells (5nM) calculated from ^{3}H-Ptx binding in live MCF7 cells[122]. Given recent interest in repurposing MT drugs for neuroprotective therapy[101,124], we verified that we could obtain binding constants in differentiated ReNcell VM human neurons (Supplementary Fig. 2.4).

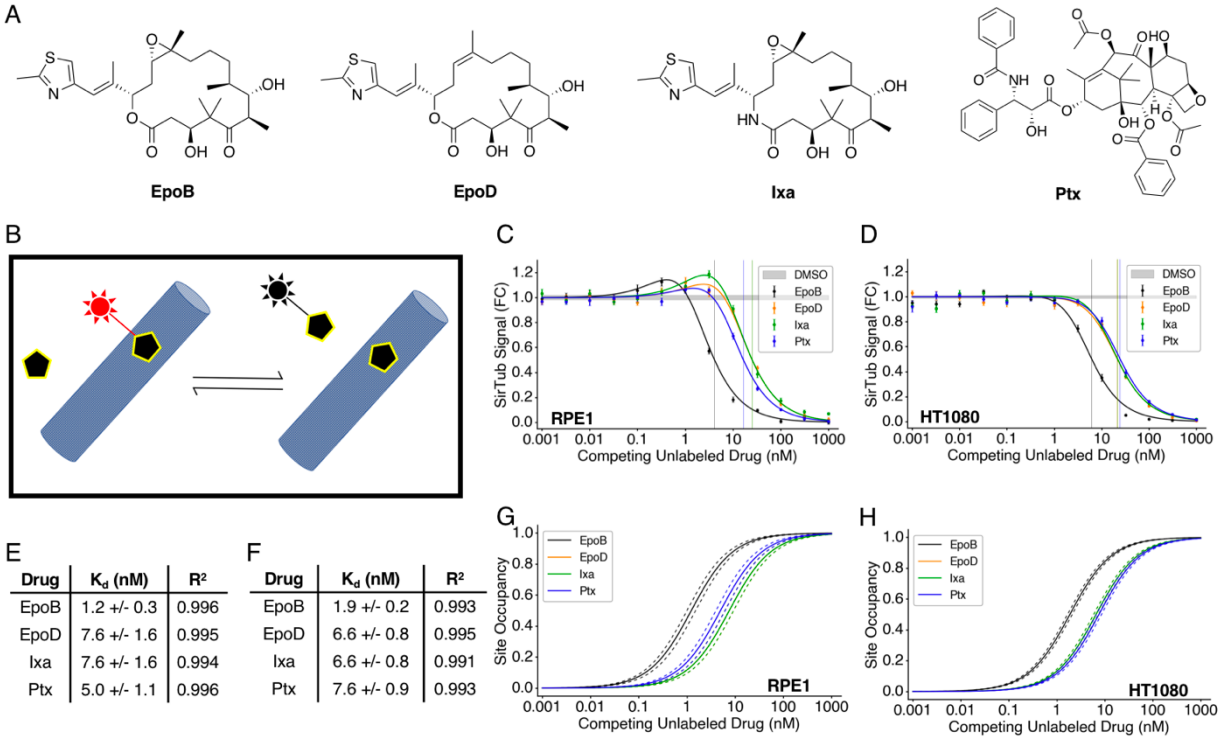

E

Drug	K_d (nM)	R^2
EpoB	1.2 +/- 0.3	0.996
EpoD	7.6 +/- 1.6	0.995
Ixa	7.6 +/- 1.6	0.994
Ptx	5.0 +/- 1.1	0.996

F

Drug	K_d (nM)	R^2
EpoB	1.9 +/- 0.2	0.993
EpoD	6.6 +/- 0.8	0.995
Ixa	6.6 +/- 0.8	0.991
Ptx	7.6 +/- 0.9	0.993

Figure 2.2. *SirTub can be used to determine binding constants of taxane-site drugs in live cells. (A) Chemical structures of EpoB, EpoD, Ixa, and Ptx. (B) Schematic of probe-displacement assay. Probe fluorescence (red) is enhanced upon target binding. (C) SirTub displacement assay in RPE1 cells. Each data point was averaged from at least 9 wells. Data was regressed using equation (2.1), which accounts for drug-induced MT polymerization. IC_{50}s are denoted by solid vertical lines. (D) SirTub displacement assay in HT1080 cells. Each data point was averaged from at least 9 wells. Data was regressed as in C. (E) $K^d_{d,app}$ values for four drugs in RPE1 cells. Values were derived from the regressions present in C. (F) $K^d_{d,app}$ values for four drugs in HT1080 cells. Values were derived from the regressions present in D. (G) Site occupancy calibration curves for RPE1 cells. The $K^d_{d,app}$ values in E were inputted into equation (2.2) to compute drug site occupancies. Dotted lines represent standard error as derived from the model fit in C. (H) Site occupancy calibration curves for HT1080 cells. As in G, site occupancy values were derived from the $K^d_{d,app}$ values in F. Note: Ixa curve is overlaid on the EpoD curve in G and H. All error bars denote standard error of the mean.*

2.4.3 Site occupancy calibration of three cellular phenotypes

We next quantified three MT- and cancer-relevant phenotypes that we could score by high-content imaging in living cells: MT polymerization dynamics, mitotic arrest and mitosis-dependent micronucleation. MT dynamics were quantified by imaging stably transfected EB3-GFP (RPE1 only), which tacks growing plus ends (Fig. 2.3A and Supplementary Fig. 2.5). This provides a sensitive and specific assay of plus end dynamics[125]. Stabilizing drugs deplete soluble tubulin, and thus block plus end growth and formation of EB3 comets. Mitotic arrest was measured by rounded morphology of living cells using EB3-GFP signal for RPE1 (Fig. 2.3B) or by adding a cell permeant dye, SiR-eribulin (see SI Appendix), for HT1080 (Supplementary Fig. 2.6). Micronucleation, which might be particularly relevant for solid tumor responses, was measured by imaging a cell-permeant DNA dye (Fig. 2.3C and Supplementary Fig. 2.7). Nuclear morphology was complex after exit from abnormal mitosis, with many clustered micronuclei that were difficult to segment with simple thresholding methods (Fig 3C inset). Watershed segmentation significantly improved the segmentation of micronuclei (Supplementary Fig. 2.7). It was not possible to segment every micronucleus present due to overlap in 2D images, but we segmented the majority as judged by eye. The number of segmentable DNA particles per unit area generated reliable dose-response curves. Fig. 2.3D shows phenotypes as a function of EpoD concentration, with the x-axis scaled to be linear in site occupancy, and the y-axis scaled to normalized fold-change of phenotype metrics. Fig. 2.3E shows mitosis and micronucleus phenotypes in HT1080s (here we lacked a bright EB3-GFP line). We performed quantitative phenotypic comparisons for all four drugs in both RPE1 (Supplementary Fig. 2.8) and HT1080 cells (Supplementary Fig. 2.9).

Plus-end dynamics was the most sensitive phenotype with loss of EB3 comets first detected at a site occupancy ~0.1 and a steady decrease to zero comets at site occupancy ~1.0. Micronucleation was the second-most sensitive phenotype, first increasing at a site occupancy of ~0.1-0.2 and peaking at ~0.6. Micronucleation declined at higher site occupancies, presumably because mitotic arrest slowed progression into micronucleated G1. We scored micronucleation at 22 hours for RPE1 and 24 hours for HT1080, the approximate doubling times for each line. This reduced complications from apoptosis. Cells arrested in mitosis eventually slip out of mitosis and progress to micronucleation or/and apoptosis over 2-3 days. Mitotic

arrest required higher site occupancies and was maximal above 0.8 in both cell lines. Mitotic arrest decreased at very high external drug concentrations, where site occupancy increased above 0.95, but we suspect our model, which assumes uniform affinity of binding sites, is no longer accurate in this regime. A notable feature of our data is the presence of a regime that exhibits strong perturbation of MT dynamics and micronucleation, but weak induction of mitotic arrest, at site occupancies of ~0.1-0.6 in both cell lines. This low-dose regime, where mitotic perturbation occurs without mitotic arrest, has been noted previously and may be of therapeutic importance[60,108].

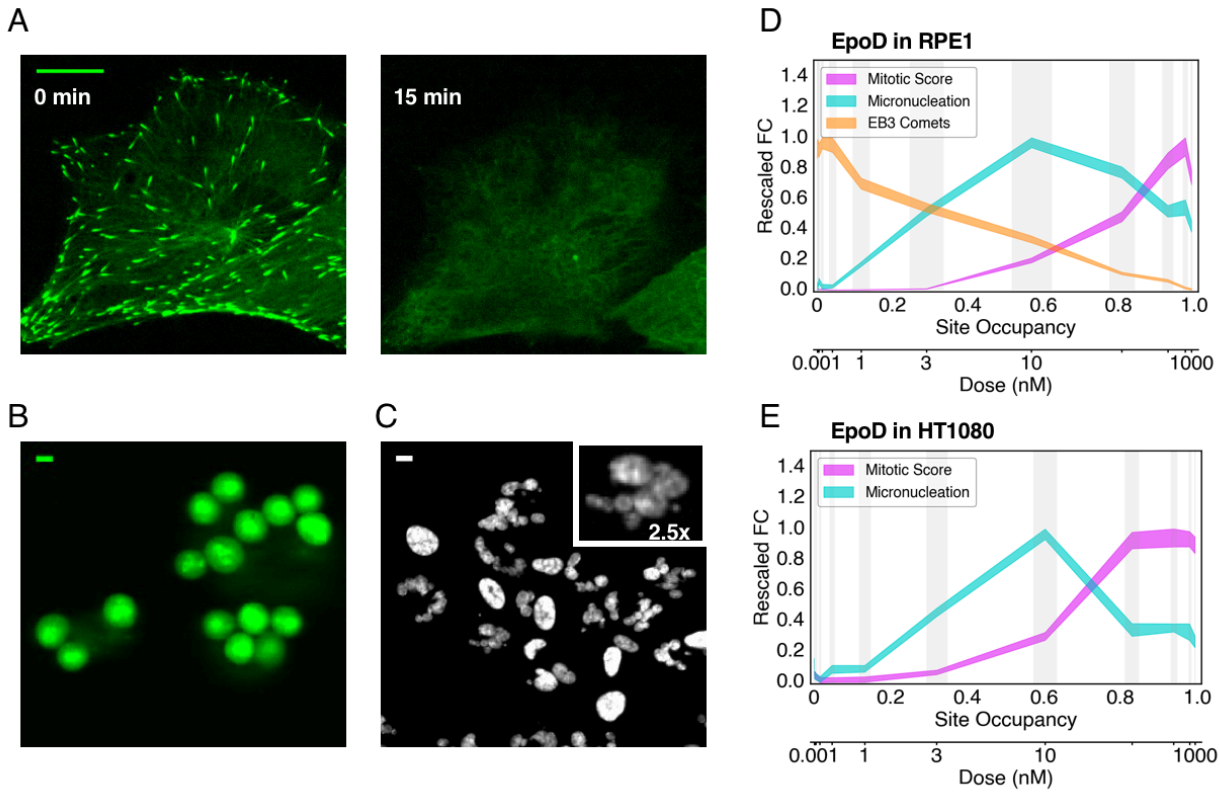

Figure 2.3. *Phenotypic comparisons on the site occupancy axis. (A) EB3 comets in RPE1 cells before and after treatment with 100 nM EpoB. Scale bar = 10 µm. (B) RPE1 cells arrested in mitosis 22 hours after treatment with 30 nM EpoB. EB3-GFP channel is shown. Scale bar = 10 µm in B and C. (C) Micronucleated RPE1 cells 22 hours after treatment with 1 nM EpoB. Image inset has been magnified 2.5x. Hoechst channel is shown. (D) Phenotypic comparison of EB3 comet loss, micronucleation, and mitotic arrest in RPE1 cells treated with EpoD. Phenotypic measurements are scaled to facilitate comparison and are shown with their corresponding standard errors (indicated by line thickness). Drug dose calibration is shown. Vertical gray bars denote standard error of site occupancy. (E) Phenotypic comparison of micronucleation and mitotic arrest in HT1080 cells treated with EpoD. Phenotypic measurements have been scaled as in D. Each value shown in D-E was averaged from 9 replicate wells.*

2.4.4 Taxane-site drugs and sensitivity differ across phenotypes and cell lines

Fig. 2.4 presents all our data for micronucleation and mitotic arrest in plots chosen to facilitate comparison between drugs (2.4A, B) or between cells (2.4C, D). In each case the phenotypic data are plotted as a function of site occupancy, so we can directly compare drugs, or cells. Broadly speaking, the four drugs were similar in their ability to promote micronucleation at lower site occupancies, and mitotic arrest at higher. That said, we also observed differences. Ptx is less efficient at promoting mitotic arrest than the epothilones in RPE1 but is one of the most efficient arresters in HT1080s at intermediate site occupancies (Fig. 2.4A, B). We did not observe any significant differences in mitotic maxima in HT1080s (Supplementary Fig. 2.10). Also, although there is no difference in micronucleation among the drugs in RPE1, these values differed significantly in HT1080, with Ixa significantly less efficient than the other drugs (Fig. 2.4A, 2.4B, S2.11).

Comparing between cell lines, and plotting the y-axis normalized to maximal fold change to facilitate comparison, we noted one major difference across all 4 drugs. HT1080s exhibited mitotic arrest at lower site occupancy than RPE1s (Fig. 2.4C). The onset of micronucleation was similar in the two cell lines but the post-peak decrease shifted to lower values in HT1080 because increased mitotic arrest, which decreased micronucleation at 24 hours, initiates at lower site occupancy (Fig. 2.4D). We especially observed this leftward shift in HT1080 with Ixa and Ptx. This result suggests that the spindle assembly checkpoint (SAC) is more sensitive to MT stabilization in HT1080s.

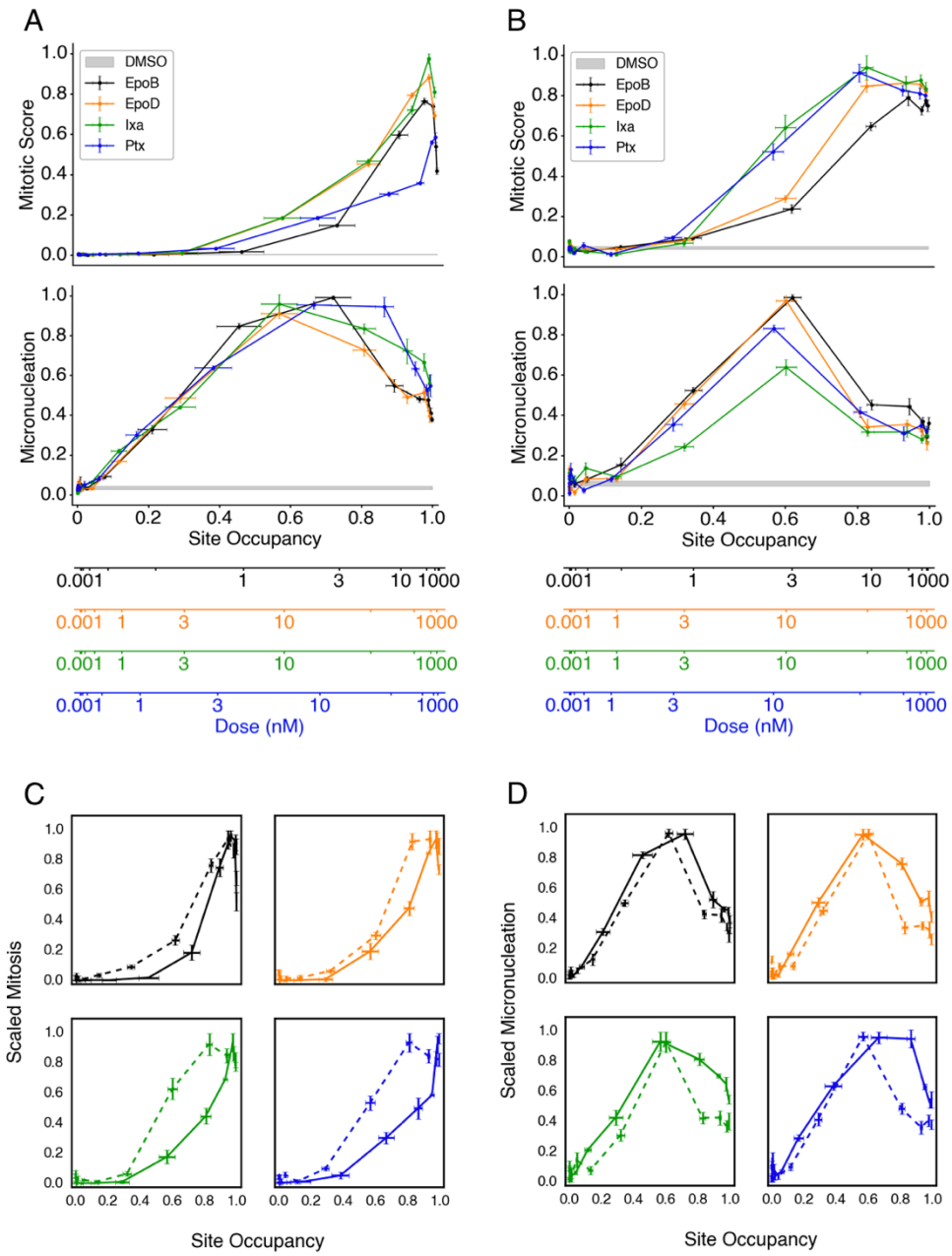

Figure 2.4. *Drug and cell-type comparisons on the site occupancy axis. (A) Drug-drug comparisons by mitotic arrest and micronucleation in RPE1 cells. All y-axis values are scaled to the maximum and minimum observed in the cell line. Dose calibration axes are included for each drug tested. (B) Drug-drug comparisons by mitotic arrest and micronucleation in HT1080 cells. All y-axis values are scaled as in A. (C) Cell-type comparison between RPE1 (solid lines) and HT1080 cells (dotted lines) by mitotic arrest. Mitotic scores have been scaled to the maximum and minimum observed for each drug. (D) Cell-type comparison between RPE1 (solid lines) and HT1080 cells (dotted lines) by micronucleation. Micronucleation values have been scaled to the maximum and minimum observed for each drug. Each value shown in A-D was averaged from 9 replicate wells. All error bars denote standard error of the mean.*

2.4.5 High initial site occupancy is needed to treat tumors

A critical question from a clinical perspective is the minimal site occupancy required *in vivo* for therapeutic efficacy. In mice, the dose of Ptx required to promote tumor regression is 10-40 mg/kg, depending on the tumor, schedule and vehicle[126–128]. We adapted our fluorescence assay to a highly responsive HT1080 xenograft tumor model that we used previously to probe cellular actions of Ptx[129,130]. Nu/nu mice with HT1080 tumors were dosed i.v. with Ptx or cremophor vehicle, followed 1 hour later by SirTub. Tumors were excised 24 hours after Ptx treatment and immediately imaged *ex vivo* by confocal microscopy. Fig. 2.5A shows SirTub images. Mitotic spindles were clearly visualized (Fig. 2.5A, inset). We were unable to resolve single MTs in interphase cells, but they exhibited specific (i.e. Ptx-competable) cytoplasmic signal that we could quantify by microscopy. Fig. 2.5B shows quantification of probe displacement in single cells from multiple fields and tumors in three mice at two doses of competing drug. Competition was dose-dependent. 30 mg/kg Ptx reduced SirTub signal by ~50% on average, with considerable heterogeneity among single cells. To confirm that our HT1080 xenografts respond in the typical range, we performed a small single-dose study, and found that 6 and 20 mg/kg Ptx i.v. reduced HT1080 tumor growth to a variable extent, and 30 mg/kg blocked growth completely (Fig. 2.5C). We applied the site occupancy calibration data that we previously obtained for HT1080s (Fig. 2.2H) to convert every SirTub measurement from Fig. 2.5B into a site occupancy estimate (Fig. 2.5D). Since we did not know the concentration of SirTub in the tumor, we considered a range for possible extracellular *in vivo* SirTub concentrations (i.e. 10 – 800 nM) and accounted for a 1-2-fold increase in MT polymer *in vivo* after addition of Ptx (Supplementary Fig. 2.12). By this analysis, we estimate the *in vivo* site occupancy for the curative 30 mg/kg dose of Ptx as being ~0.8 at 24 hours (Fig. 2.5D). We previously measured peak mitotic arrest values of ~5-10% of cells ~24 hours after a 30 mg/kg Ptx dose in HT1080 xenografts, and peak micronucleation values of ~25-30% of cells at ~72 hours[130]. We conclude that the minimal curative dose of Ptx in the HT1080 model corresponds to an initial site occupancy of ~0.8 in the tumor, which triggers mitotic arrest at peak drug concentration, followed by micronucleation as site occupancy declines through dissociation from binding sites and clearance from circulation (Fig. 2.5E).

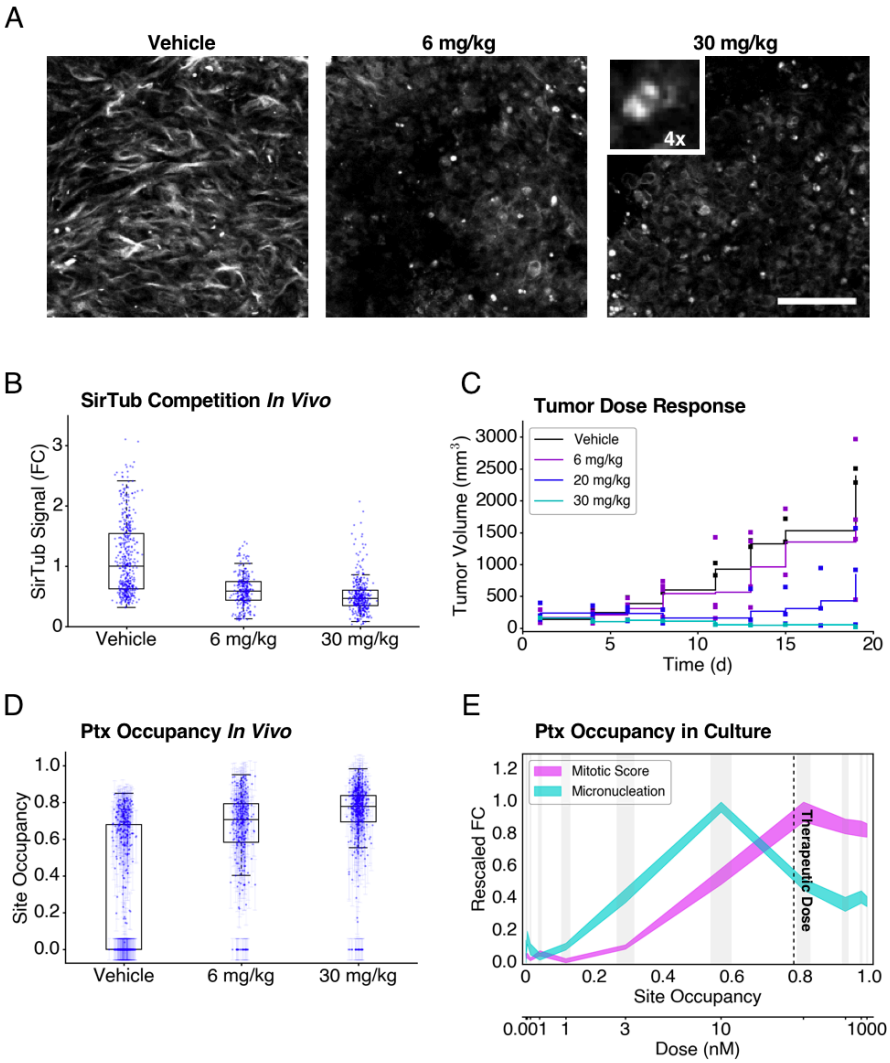

Figure 2.5. *Taxane site occupancy in vivo. (A) Ex vivo images of SirTub in HT1080 xenograft tumor 24 hours after infusion of vehicle control (left), 6 mg/kg Ptx (middle), and 30 mg/kg Ptx (right). Inset shows a mitotic cell labeled with SirTub. Scale bar = 100 µm. (B) SirTub displacement in HT1080 xenograft tumors 24 hours after Ptx treatment. Each data point denotes a single cell. FC = fold-change (i.e. all values are normalized by the average SirTub signal in the vehicle control). (C) Response of HT1080 xenograft tumors to single treatments with Ptx. Once palpable tumors were established, mice were treated on day 0 with a single i.v. dose of Ptx in cremophor EL as indicated. Each square denotes a single measurement of a mouse tumor. Solid lines track average tumor volume. (D) All data points in B have been converted to site occupancy measurements using the data in 2.2C and 2.2G. At the indicated doses, drug-induced microtubule polymerization was assumed to be 1-2-fold compared to basal. Standard error bars are shown in lighter blue at each data point. (E) Phenotypic comparison of micronucleation and mitotic arrest in HT1080 cells treated with Ptx. Dotted line represents the predicted intratumoral site occupancy. Phenotypic measurements are scaled to facilitate comparison and are shown with their corresponding standard errors (indicated by line thickness). Drug dose calibration is shown. Vertical gray bars denote standard error of site occupancy. Each value shown in E was averaged from 9 replicate wells.*

2.5 Discussion

A novel ligand displacement assay in live cells allowed us to calculate taxane site occupancy as a function of extracellular concentration for four drugs in two cell lines. Our inferred K_d values were similar to published K_ds measured using conceptually similar fluorescent ligand displacement assays on pure MTs[119] and live cell binding of ^{3}H-Ptx[122]. Previous work mostly measured phenotypic effects of taxane-site drugs as a function of external drug concentration, or specific phenotypes at saturating drug concentration[114,131]. Our work allows more precise comparisons of biological effects across external concentrations, drug analogs and cell types.

A possible point of confusion in taxane site pharmacology is the relationship between the concentration of free and total drug inside cells. Taxanes accumulate in cells and tumors, so their total concentration inside cells far exceeds the concentration in medium or plasma[122,132]. Total drug is the sum of free, specifically-bound, and non-specifically-bound drug. We could not quantify non-specific binding of non-fluorescent drugs, but we corrected all our data for non-specific binding of probe. Specifically-bound drug can be calculated from our data by multiplying our site occupancy values by binding site concentration. Tubulin constitutes ~4% of total protein in HeLa cells[133], corresponding to approximately 20 μM, and most of it polymerizes when taxanes or epothilones are added. Given the apparent K_ds of the drugs we tested, the concentration of specifically-bound, unlabeled drug is thus 3-4 orders of magnitude higher than unbound drug, consistent with previous data using ^{3}H-Ptx binding[122].

Our data revealed a clear rank order in sensitivity of phenotypic effects to site occupancy. Loss of MT dynamics was the most sensitive, with detectable perturbation starting at a site occupancy of ~0.1, followed by micronucleation starting at ~0.2 and mitotic arrest requiring 0.6-1.0. This rank order was similar for all four drugs in both cell lines. Sub-stoichiometric binding of Ptx was previously shown to inhibit polymerization dynamics[40], consistent with our findings. Previous work also showed that chromosome segregation defects and micronucleation occur at lower concentrations of Ptx than mitotic arrest[60,108]. The mechanism of micronucleation is unclear, and probably involves a combination of ectopic spindle pole formation[60] and ectopic cleavage furrow assembly[134]. Mitotic arrest decreased at the highest external drug

concentrations we tested, and the highest inferred site occupancies (>0.95). Caution is required in interpreting these high site occupancy values, since our model assumes homogeneous binding sites, and very high drug concentration might access additional, lower-affinity sites, e.g. on exposed plus ends. Decreased duration of mitotic arrest at paclitaxel concentrations above 1 mM was noted previously and attributed to stabilization of syntelic kinetochore attachments[135]. This bell-shaped dose-response is interesting but unlikely to be relevant to chemotherapy, since mitotic arrest only decreased at paclitaxel concentrations that exceed safe plasma concentrations[60,132].

We asked if taxane site drugs differ in their phenotypic actions once normalized by site occupancy, which compares efficacy independent of K_d. Comparing across drugs in RPE1 (Fig. 2.4A) and HT1080 cells (Fig. 2.4B) we noted overall similar efficacies, but some interesting differences, e.g. more efficient mitotic arrest by Ptx and Ixa in HT1080. While EpoD and Ixa had identical apparent K_d values in HT1080s, their phenotypic effects differed noticeably, suggesting different efficacies. However, these differences were not seen in RPE1 cells. Future analysis across more diverse SAR series might reveal larger efficacy differences.

A central question in taxane-site pharmacology is which phenotypic effects are responsible for tumor regression. This is a complex issue, with different authors favoring chromosome loss via aberrant mitosis[113], bystander killing[136], and direct cytotoxic actions on non-dividing cells[112]. Our work does not address this question directly, but it provides new information. In particular, we confirm that micronucleation occurs at lower concentrations than mitotic arrest for all drugs and therefore might predominate in tumors. Standard paclitaxel doses are sufficient to cause mitotic arrest in tumors 24 hours after drug infusion[137], but plasma drug concentrations decrease rapidly due to drug clearance between doses. Micronuclei trigger post-mitotic inflammatory signaling[61,138]. This may allow a subset of tumor cells that pass through mitosis in drug to cause regression of the whole tumor in sensitive patients via recruitment of cytotoxic leukocytes, and/or inflammatory damage to the neovasculature[139].

To connect our work to *in vivo* pharmacology we measured the Ptx dose required to cure a sensitive xenograft tumor model, and then estimated site occupancy in tumor cells 24 hours after this dose (Fig. 2.5). We observed a 50% decrease in SirTub signal at the curative 30 mg/kg dose. Our calculations suggest that

the *in vivo* site occupancy of SirTub was below 0.2 in the absence of drug, so in the presence of 30 mg/kg Ptx, SirTub occupancy would decrease to below 0.1, leaving up to 90% of taxane sites for Ptx to bind. This is mathematically consistent with our data and suggests that a relatively high initial Ptx site occupancy, ~0.8, was required for cure following a single dose in this model. How does this relate to human patients? A recent study assessed the intratumoral and plasma concentration of Ptx in breast cancer patients as 1.1-9 μM and 80-280 nM, respectively, 20 hours after infusion of Ptx[60]. Intratumoral concentrations measure the sum of free, specifically- and non-specifically bound drug, and their interpretation is difficult. If we assume the plasma concentration is close to the extracellular concentration, and drug efflux pumping is not a major issue, then we can estimate site occupancy using our data. 80-280 nM extracellular Ptx should generate a site occupancy greater than 0.8 (Fig. 2.2G, H). This is in the concentration regime that promotes mitotic arrest (Fig. 2.5E), consistent with elevated mitotic index at 24 hours post-Ptx in human tumors[137]. However, micronucleation will likely predominate at later time points as initially arrested cells slip into micronucleated interphase, and cells that newly enter mitosis do so at drug concentrations that are lower due to clearance. Even at 30mg/kg Ptx in HT10180 xenograft tumors, micronucleation strongly predominated over mitotic arrest at 72 hours post-drug[130].

Our work sheds new light on taxane pharmacology and demonstrates the potential of site occupancy measurements to guide future medicinal chemistry, whether for treatment of cancer or neurological diseases. It informs, but does not answer, the longstanding question of how taxanes promote regression of solid tumors. Based on the predominance of micronucleation over a broad range of site occupancies we currently favor an inflammatory micronucleation model of taxane action[139].

2.6 Methods

2.6.1 Reagents and cell lines

Epothilone B (EpoB) and ixabepilone (Ixa) were purchased from Selleckchem, Epothilone D (EpoD) was purchased from MedChemExpress, whereas paclitaxel (Ptx) and verapamil hydrochloride were purchased from Sigma Aldrich. Docetaxel, which was used in the synthesis of SiR-tubulin (SirTub), was purchased from LC Labs. Eribulin mesylate, which was used in the synthesis of SiR-eribulin (SirErib), was

obtained by lyophilization of HALAVEN® formulations (1 mg/2 mL; purchased from the MGH pharmacy). RPE1 cells expressing EB3-GFP were a generous gift from David Pellman at Harvard Medical School.

2.6.2 Cell culture

RPE1 cells expressing EB3-GFP were maintained in DMEM/F12 (Life Technologies) and supplemented with 10% FBS (GIBCO) (v/v) and 1% penicillin-streptomycin (Cellgro). HT1080 cells expressing EB3-mApple were grown in DMEM (Cellgro) supplemented with 10% FBS and 1% penicillin-streptomycin. ReNcell VM human neural progenitor cells (Millipore) were grown in ReNcell NSC maintenance medium supplemented with EGF and bFGF and differentiated into dopaminergic neurons in growth factor free medium for 14 days.

2.6.3 Live-cell microscopy

For spinning-disk SirTub imaging, RPE1 cells were imaged on 35-mm plates at 20-30% confluency. For high-content imaging, RPE1 and HT1080 cells were seeded 5000 cells per well in 20 μL serum-free media on 384-well optical bottom Cell Carrier plates (Perkin Elmer) coated with Cell-Tak (Corning). After 45 minutes, 20 μL media with 20% FBS was added to each well. After 4 hours, 40 μL of media containing 10% FBS, 20μM verapamil, and 2x SirTub (for SirTub plates only) was added to each well. Competing drugs were dispensed immediately after verapamil addition using the D300 Digital Dispenser (Hewlett-Packard). SirTub was found to be aggregate-prone which would result in inconsistent probe distribution by the D300. For this reason, SirTub was thawed, vortexed vigorously, centrifuged at 20,000 x g for 10 minutes, and carefully transferred to media, which was then manually pipetted on the imaging plates before drug treatments. Final DMSO concentrations were kept below 0.02%. Image acquisition was started immediately after drug treatments, except for the EB3 comet experiments; for these experiments, one time-point was acquired prior to drug addition.

2.6.4 Image acquisition

For the initial proof of principle SirTub competition experiment (Fig. 2.1A), we used a spinning-disk confocal microscope (Nikon) equipped with a 60x/1.42 NA Plan Apochromat objective, heated chamber, and MetaMorph acquisition software. For Fig. 2.1C, the final time-point was used to determine the non-specific signal of SiR-tubulin, after which the non-specific signal value was subtracted from all preceding time-points. For all other SirTub experiments, we imaged cells using the InCELL Analyzer 6000 high content microscope (GE Healthcare Life Sciences), equipped with 40x/0.95 NA (for EB3 comet imaging) and 20x/0.75 NA (for all other imaging) Plan Apochromat objectives, heated stage and heated lid, as well as constant CO_2 flow. For SirTub, Hoechst, and EB3 imaging, optimal focal planes were determined using the auto-offset function in the InCELL software. For imaging of mitotic cells, the auto-offset parameter was raised by 10 μm to blur out non-mitotic cells and put mitotic cells in focus. Rounded geometry was then used to segment the mitotic cells. Confocality was used for all imaging except nuclear area quantification. 2x2 binning was used for all imaging except EB3 imaging.

2.6.5 *In vivo* SirTub competition and microscopy

All animal research was performed in accordance with the guidelines from the Institutional Subcommittee on Research Animal Care. 2 million HT1080-H2B-mApple cells were implanted subcutaneously into female nu/nu mice at 4-6 weeks of age. Roughly two weeks later, the indicated dose of Ptx or vehicle was administered intravenously (i.v.) in DMAC:solutol and PBS from a DMSO stock solution; 1 hour later, 300 nmol of SirTub was administered using the same i.v. formulation. 24 hours following taxane treatment, tumors were excised and immediately imaged. Prior to harvesting, 10 kDa dextran-pacificBlue and 2 MDa FITC-dextran were co-administered i.v. to confirm vascular perfusion to the tumor as an inclusion criterion. Data for each condition was obtained from at least 250 cells across at least 3 tumors. Tumor microscopy was performed on an Olympus FV1000 confocal-multiphoton imaging system, with a XLUMPLFLN 20x water immersion objective (NA 1.0; Olympus America); 2x digital zoom; sequential scanning using 405-nm, 473-nm, 559-nm, and 635-nm diode lasers and a DM405/473/559/635-nm dichroic

beam splitter; and collection of emitted light using beam splitters (SDM473, SDM560, and/or SDM 640) and emission filters BA430-455, BA490-540, BA575-620, and BA655-755 (all Olympus America).

2.6.6 Image analysis

Images were analyzed using custom-built software in Python. Every SirTub image obtained from the InCELL was split into 16 equally sized smaller images, each of which was thresholded using a Gaussian mixture model. After thresholding, background was defined and subtracted, and total resultant signal intensity was calculated. All integrated signal intensities in a given well were summed together for each time point. The final aggregate signal intensity was then normalized by total intracellular SirTub pixel area present in the well at each time point. 800nM EpoB was used as a positive control and the final value obtained for SirTub signal intensity in this condition was defined as the signal for non-specific binding; we subtracted this value from all other drug conditions to avoid quantification artifacts due to non-specific binding.

For EB3 comet quantification, control images were thresholded manually, after which the resultant threshold was implemented across all images from a given plate. Comets were then scored using custom-built particle detection software. Comets from all quantified fields in a given well were summed together for each time point. The final number of detected comets was then normalized by the total cell area (as defined by cytosolic EB3-GFP) present in the well at each time point. Background signal was defined as the comet value obtained at 10 hours in the presence of 1μM EpoB. This value was subtracted from all other acquired values.

For mitotic scoring, control images were thresholded manually, after which the resultant threshold was implemented across all images from a given plate. For micronucleation scoring, Otsu thresholding was implemented on every image. Mitosis and micronucleation were scored using custom-built particle detection software which implemented watershed segmentation on every image. All quantified fields from a given well were summed together. The final number of detected particles was then normalized by total nuclear area (as defined by Hoechst stain) across all images for a given well.

2.6.7 Scoring of mitotic cells and micronuclei

For mitotic and micronucleation scoring in RPE1s, drug-treated cells were incubated for one doubling time (22 hours in RPE1 and 24 hours in HT1080) and then stained with 1ug/ml Hoechst for 10 minutes, after which the media was replaced. The EB3-GFP marker was imaged to define mitotic cells for later quantification, whereas Hoechst was used to define nuclear area and micronucleation. For mitotic scoring in HT1080s, cells were treated with 1 μg/ml Hoechst and 10 μM EpoB for 10 minutes to stain nuclei and fully polymerize MTs, after which this media was replaced with media containing 100 nM SirErib. After 30 minutes of staining, HT1080 cells were imaged and the SirErib channel (i.e. far red) was used to define mitotic cells for later quantification. Note that very little difference was observed when using SirErib instead of EB3-GFP to score mitotic RPE1 cells (Supplementary Fig. 2.16). Micronucleation for HT1080s was scored on separate drug-treated plates stained with 1 μg/ml Hoechst. For all imaging experiments, RPE1 and HT1080 cells were imaged in DMEM/F12 and DMEM (respectively) without phenol red (Corning), each supplemented with 10% FBS and 1% penicillin-streptomycin.

2.6.8 Determination of the minimal tumor regressing dose of paclitaxel

Mice xenografts were established with HT1080 fibrosarcoma cells. Approximately 100,000 cells were injected subcutaneously into the flank of 7 – 8-week-old female nu/nu nude mice (Crl:NU-Foxn1nu). Two tumors were established per mouse. Once palpable tumors reached approximately 1 cm in diameter, mice were administered a single i.v. dose of paclitaxel in cremophor EL, as indicated, through tail vein injections. Tumor volume was determined by external caliper measurements and carried out by independent researchers at the Dana Farber Cancer Institute Lurie Family Imaging Center. To calculate tumor volume, the greatest longitudinal diameter (length) and the greatest transverse diameter (width) were measured and volume was calculated by the modified ellipsoidal formula:

(2.3) $$TumorVolume = \frac{1}{2}\left(Length \cdot Width^2\right)$$

Mice were sacrificed if the tumor exceeded the IACUC-specified maximum.

2.6.9 Regression and confidence interval determination for binding constants

For each drug, average values from each condition were used to regress our SirTub competition data to our ligand-displacement model. The residual sum of squares (RSS) was used as an objective function to find the minimum of the corresponding log-likelihood function. To determine confidence intervals, data values from every well were used to define the log-likelihood function at this minimum (assuming Gaussian error), after which the relevant confidence intervals were extracted from the diagonal values of the corresponding hessian matrix.

2.6.10 Statistical test for drug-drug comparisons

Unpaired t-tests were used to assess the statistical significance of differences between drug-induced phenotypic maxima. For each of these comparisons, we assumed 16 degrees of freedom and used 1.746, 2.583, and 3.686 as the corresponding t-values for p-values of 0.05, 0.01, and 0.001, respectively.

2.6.11 Determination of *in vivo* site occupancy at 30 mg/kg Ptx

Since SirTub signal fold-change (i.e. $[PMT]_{FC}$) was measured in the xenograft tumors, equation (S23) was used to calculate site occupancy (S_d). The site occupancy calibrations obtained for Ptx in cultured HT1080 cells (Fig. 2.2G) were used to determine the relationship between $[PMT]_{FC}$ and $[MT]_{FC}$ (i.e. fold-change of MT polymer). With this information, it was possible to calculate S_d for any measured value of $[PMT]_{FC}$. The value of $[PMT]_{FC}$ was found to be 46% at 30 mg/kg Ptx.

2.6.12 Synthesis of SirTub and SirErib

Reactions were carried out under an atmosphere of argon in air-dried glassware with magnetic stirring. Air- and/or moisture-sensitive liquids were transferred via syringe. All reagents were obtained from commercial sources and used without further purification. Column chromatography was carried out using C18 flash cartridges (Biotage). NMR spectra were recorded on a Bruker Avance UltraShield 400 MHz spectrometer. Chemical shifts are reported in parts per million (δ) and calibrated using residual undeuterated solvent. Data is represented as follows: chemical shift, multiplicity, coupling constant (J, Hz)

and integration. LCMS and UV-spectrum analysis were performed on a Waters instrument equipped with a Waters 2424 ELS Detector, Waters 2998 UV-Vis Diode array Detector, Waters 2475 Multi-wavelength Fluorescence Detector, and a Waters 3100 Mass Detector using a Waters XTerra® C18 (5 µm) column.

SiR-C_8-CO_2H and SirTub were prepared as previously described (Supplementary Fig. 2.13) and the purity of SirTub was confirmed by LCMS and NMR (matching data previously reported)[121,140,141].

SirErib was synthesized analogous to SirTub by conjugation of SiR to eribulin using 8-aminooctanoic acid as linker (Supplementary Fig. 2.14). To a solution of eribulin mesylate (10 mM in DMSO, 300 μL, 3 μmol) was added SiR-C_8-CO_2H (60 μL of 50 mM solution in DMSO, 3 μmol), HBTU (1.14 mg, 3 μmol) and diisopropylethylamine (DIPEA, 5.2 μL, 30 μmol). The mixture was stirred at room temperature for 3 hours and then loaded directly onto a Biotage SNAP Ultra C18 column. The product was obtained after reversed phase chromatography (H_2O/MeCN gradient elution, 0.1% formic acid) as a blue solid (2.7 mg, 68%). Supplementary Fig. 2.15 shows the ^{1}H NMR, chromatogram, and UV spectra for SirErib. ^{1}H NMR (400 MHz, DMSO-d_6) δ 8.74-8.68 (m, 1H), 8.07 (d, J = 8.0 Hz, 1H), 8.02 (d, J = 8.0 Hz, 1H), 7.72-7.66 (m, 1H), 7.65 (s, 1H), 7.04-7-00 (m, 2H), 6.68-6.60 (m, 4H), 5.07-5.03 (m, 1H), 5.01-4.97 (m, 1H), 4.85-4.81 (m, 1H), 4.76-4.72 (m, 1H), 4.66-4.61 (m, 1H), 4.59-4.54 (m, 2H), 4.29-4.22 (m, 1H), 4.21-4.13 (m, 1H), 4.10 (s, 3H), 4.06-3.98 (m, 1H), 3.83-3.72 (m, 2H), 3.72-3.64 (m, 1H), 3.57-3.46 (m, 3H), 3.28-3.22 (m, 4H), 3.22-3.16 (m, 2H), 3.06-2.99 (m, 2H), 2.91 (s, 12H), 2.86-2.69 (m, 3H), 2.33-2.12 (m, 6H), 2.08-1.85 (m, 8H), 1.75-1.59 (m, 5H), 1.58-1.41 (m, 7H), 1.39-1.17 (m, 11H), 1.03 (d, J = 5.7 Hz, 3H), 0.64 (s, 3H), 0.53 (s, 3H); MS $[M+H]^+$ calculated 1325.70 for $C_{75}H_{101}N_4O_{15}Si^+$, found 1325.83.

2.7 Derivation of taxane-site occupancy model

We can state the following biochemical relationships:

(S2.1) $$D_{out} \rightleftharpoons D_{in} + MT \rightleftharpoons DMT$$

(S2.2) $$P_{out} \rightleftharpoons P_{in} + MT \rightleftharpoons PMT$$

Extracellular drug (D_{out}) defuses into the cell (D_{in}) and binds to unbound taxane sites (MT). This generates a drug-bound taxane site (DMT). This is similar in the case of the probe (P_{out} and P_{in}) which produces probe-bound taxane sites (PMT; measureable by fluorescence). We can then derive equations for binding constants for the competing drug (K^d_d) and probe (K^p_d):

$$K_d^d = \frac{[D_{in}][MT]}{[DMT]} \quad \text{(S2.3)}$$

$$K_d^p = \frac{[P_{in}][MT]}{[PMT]} \quad \text{(S2.4)}$$

$$K_{d,app}^d = \frac{[D_{out}][MT]}{[DMT]} \quad \text{(S2.5)}$$

$$K_{d,app}^p = \frac{[P_{out}][MT]}{[PMT]} \quad \text{(S2.6)}$$

Where:

$$K_{d,app}^d = \frac{K_d^d[D_{out}]}{[D_{in}]} \quad \text{(S2.8)}$$

$$K_{d,app}^p = \frac{K_d^p[P_{out}]}{[P_{in}]} \quad \text{(S2.9)}$$

Resolving equation (S2.6) and (S2.7) for [DMT] and [MT], respectively, we get:

$$[DMT] = \frac{[D_{out}][MT]}{K_{d,app}^d} \quad \text{(S2.10)}$$

$$[MT] = \frac{K_{d,app}^p[PMT]}{[P_{out}]} \quad \text{(S2.11)}$$

Furthermore, equation (S2.10) can be furthered solved as a function of [PMT]:

$$[DMT] = \frac{K_{d,app}^p[D_{out}][PMT]}{K_{d,app}^d[P_{out}]} \quad \text{(S2.12)}$$

Also, the total amount of taxane sites is equal to the amount of MT tubulin that is bound to drug, probe, or nothing. Therefore:

(S2.13) $$[MT]_{tot} = [DMT] + [PMT] + [MT]$$

Substituting equations leads to:

(S2.14) $$[MT]_{tot} = \frac{K^p_{d,app}[D_{out}][PMT]}{K^d_{d,app}[P_{out}]} + [PMT] + \frac{K^p_{d,app}[PMT]}{[P_{out}]}$$

Solving for [PMT] gives:

(S2.15) $$[PMT] = \frac{[MT]_{tot}}{\frac{K^p_{d,app}[D_{out}]}{K^d_{d,app}[P_{out}]} + \frac{K^p_{d,app}}{[P_{out}]} + 1}$$

Now solving for the apparent drug dissociation constant ($K^d_{d,app}$) gives:

(S2.16) $$K^d_{d,app} = \frac{[D_{out}]}{\frac{[MT]_{tot}[P_{out}]}{[PMT]K^p_{d,app}} - \frac{[P_{out}]}{K^p_{d,app}} - 1}$$

Ultimately, we desire drug site occupancy in the absence of probe. By definition, this is represented by:

(S2.17) $$S_d = \frac{[DMT]}{[MT]_{tot}} = \frac{\frac{[D_{out}][MT]}{K^d_{d,app}}}{\frac{[D_{out}][MT]}{K^d_{d,app}} + [MT]}$$

Which when rearranged gives:

(S2.18) $$S_d = \frac{[D_{out}]}{K^d_{d,app} + [D_{out}]}$$

Likewise, for the probe site occupancy in the absence of drug:

(S2.19)
$$S_p = \frac{[PMT]}{[MT]_{tot}} = \frac{[P_{out}]}{K^p_{d,app} + [P_{out}]}$$

Note that the basal amount of total MT polymer can be derived:

(S2.20)
$$[MT]_o = [PMT]_o \left(\frac{K^p_{d,app} + [P_{out}]}{[P_{out}]} \right) = [PMT]_o \left(\frac{K^p_{d,app}}{[P_{out}]} + 1 \right)$$

We can also determine drug site occupancy as a function of [PMT] fold-change ($[PMT]_{FC}$). This is useful for the case in which we might know $[PMT]_{FC}$ but not S_d. In order to do this, we need to derive drug concentration as a function of site occupancy:

(S2.21)
$$[D_{out}] = \frac{S_d K^d_{d,app}}{1 - S_d}$$

If we rewrite equation (S15) in terms of $[PMT]_{FC}$ (i.e. divide each side by $[PMT]_o$) and then use the relationship between site occupancy and drug concentration, we can get:

(S2.22)
$$[PMT]_{FC} = [MT]_{FC} \left(\frac{\frac{K^p_{d,app}}{[P_{out}]} + 1}{\frac{K^p_{d,app}}{[P_{out}]} \frac{S_d}{1-S_d} + \frac{K^p_{d,app}}{[P_{out}]} + 1} \right)$$

Then after substituting this expression into the equation for [PMT] and solving for drug site occupancy, we get:

(S2.23)
$$S_d = \frac{[MT]_{FC} - [PMT]_{FC}}{[MT]_{FC} - \frac{[PMT]_{FC}}{\frac{K^p_{d,app}}{[P_{out}]} + 1}}$$

For simulating the amount of total MT polymer, we have used an exponential relaxation equation:

(S2.24) $$[MT]_{tot} = [MT]_o e^{-k[D_{out}]} + [MT]_{max}(1 - e^{-k[D_{out}]})$$

Where $[MT]_{tot}$ is the amount of total MT polymer at a given drug concentration. $[MT]_o$ is the amount of total MT polymer in the absence of drug and $[MT]_{max}$ is the amount of total MT polymer when it has been maximally polymerized by drug (i.e. this is the same as the total concentration of tubulin dimer in the cell). Note that $[MT]_o$ is known, as is $[MT]_{max}$ (from known MT fold-change). The k constant is the only independent variable that must be determined. As we have it, $[MT]_{tot}$ is ultimately a function of [PMT] and $K^p_{d,app}$. If $[P_{out}]$ is not known (e.g. *in vivo*), we assume that $[P_{out}]$ is a uniformly distributed variable from 10nM to 800nM and by doing so we put generous error bounds on $[P_{out}]$. Note: an exponential relaxation equation has previously been used by Lukinavičius, G. *et al* to model MT growth[121].

2.8 Acknowledgements

This work was supported by NIH grants GM39565, K99CA207744, and U01CA206997. J.J.P. was supported by a Ruth Kirschstein fellowship (GM117882-02) from NIH-GM. We thank the Nikon Imaging Center and the Lab of Systems Pharmacology at HMS for microscopy support and the Lurie Center at the Dana Farber Cancer Institute for aiding with the *in vivo* paclitaxel dose escalation experiments. We also thank David Pellman (HMS) for gifting us with RPE1 cells expressing EB3-GFP and Allon Klein (HMS) for help with error analysis in our model.

Chapter 3

Phosphoproteomics reveals an acute signaling response to pharmacological perturbation of microtubules

Javier J. Pineda, Jui-Hsia Weng, Marian Kalocsay, Matthew Berberich,
Robert Everley, Marc Presler, Timothy J. Mitchison

3.1 Attributions

The following chapter describes a phosphoproteomics approach that I undertook to elucidate the immediate cellular signaling involved in microtubule drug perturbations. I was aided in this project by a number of exceptional scientists. First, Dr. Marc Presler taught me how to conduct enrichment of phosphopeptides using titanium dioxide microspheres. Dr. Robert Everley and Matthew Berberich helped me with later-stage mass spectrometry sample preparation and taught me how to fully process raw data produced from a mass spectrometer. Dr. Marian Kalocsay was the last mass spectrometry expert who helped me with phosphoproteomics sample preparation. We improved the phosphoenrichment protocol for my samples and are in the midst of procuring more phosphoenriched sample sets. As this data is not yet complete, it is not contained within this thesis, but it will be included in the manuscript that we will produce from this chapter. Finally, Dr. Jui-Hsia Weng conducted phospho-Western blot analyses that were critical for the claims made in this chapter. I designed and performed all of the imaging and phosphoproteomic experiments contained herein and wrote all relevant coding in Python to analyze the data.

3.2 Abstract

Microtubules are dynamic polymers with critical roles in cell division, motility, and vesicle trafficking. Many microtubule-targeting drugs exist, several of which exert antitumor effects in cancer chemotherapy, yet little is known about the biological activities of these drugs beyond perturbation of mitosis. We used phosphoproteomics to identify more than 23,000 phosphopeptides in quiescent cells, and to classify more than 2000 which change in response to microtubule perturbation. We found that chemical perturbation of microtubules stimulates extensive phospho-signaling within minutes. We classified responses as specific for stabilizing or destabilizing drugs, or common to both. Motif analysis, clustering algorithms, and bioinformatics revealed differential involvement of MAPK pathways in these responses. Using combinatorial drug treatments, we confirmed the involvement of JNK in response to microtubule stabilization. Remarkably, almost all of the 100s of phosphopeptides induced by stabilizing drugs such as epothilone-B, many of which were nuclear, were due to JNK activity. Furthermore, our data suggest that increased phosphorylation of these sites was caused by inhibition of opposing phosphatases rather than activation of

JNK itself. Our results implicate phosphatase regulation as a central response to perturbation and provide novel insights into the pharmacology of microtubule-targeting drugs used in cancer chemotherapy.

3.3 Introduction

Microtubules (MTs) and their intrinsic dynamic instability[18] are vital for many eukaryotic cell processes. Their dynamic nature is tuned by regulatory proteins, which are capable of providing increased stability or instability depending on the phase of the cell cycle or cell type[142], and prolonged chemical disruption of MT dynamics typically leads to cell death[143]. There are many classes of natural products and synthetic drugs that disrupt MTs, either by binding the polymers or by binding dimeric tubulin in the cytosol. These drugs can be summed up most simply as compounds that either stabilize or destabilize MTs. Among the most clinically relevant of these drugs are those that bind the taxane and vinca sites on ß-tubulin. Taxane-site drugs, such as paclitaxel (Ptx), and vinca-site drugs, such as eribulin (Erb), are used widely in the clinic for cancer chemotherapy. Other drugs, such as epothilone-B (EpoB), which binds the taxane site, and combretastatin-A4 (Ca4), which binds the colchicine site, have shown promise in clinical trials, but clinical use of these agents has been limited by toxicity issues. The therapeutic efficacy of MT-targeting drugs has conventionally been attributed to mitotic arrest, which is a prominent biomarker of response to these drugs in cells[59], though recent studies have suggested that interphase effects may also be therapeutically relevant[144]. The mechanisms responsible for this have not been extensively studied, although interphase death by MT perturbation is a known biological phenomenon. Vinca alkaloids, for example, have been found to induce acute apoptosis in leukemia cells before the onset of mitosis[145,146].

Post-translational modifications play a critical role in the dynamic MT life cycle, either by modifying tubulin itself[147] or by modifying MT-associated proteins (MAPs)[31,148]. In particular, phosphorylation is known to affect the MT-binding affinities of several MAPs, plus-end binding proteins (+TIPs) and catastrophe factors. MT-affinity regulating kinases (MARKs) can directly phosphorylate the MT-binding domains of classical MAPs (i.e. MAP2, MAP4, and Tau)[31], whereas protein kinase A (PKA) phosphorylates CLIP1[148] – in either case, the phosphorylation destabilizes MTs. Disruption of MTs can also induce phospho-signaling, in turn. Previous work confirmed that prolonged treatment with MT-targeting drugs stimulates mitogen-

activated protein kinase (MAPK) signaling in cycling and non-cycling cells[62,63]. The c-Jun N-terminal kinase (JNK), p38, and extracellular-signal-regulated kinase (ERK) pathways have all been implicated in the response to these drugs, though there has been little consensus on the extent and nature of the signaling, which appears to be cell-type dependent, dose-responsive, and can differ between MT-stabilizing and destabilizing drugs[62,64–66]. Other than MT-mediated MAPK regulation, little work has been done to elucidate other phospho-signaling induced by these drugs.

A mass spectrometry (MS)-based approach would offer a highly quantitative and more global assessment of MT-proximal protein phosphorylation. Recent advances in MS phosphoproteomics have made it possible to quantify the phosphorylation states of thousands of phosphorylation sites in a single experiment[87,149]. Multiplexing can be accomplished through the use of isobaric affinity tags, such as tandem mass tags (TMTs)[85], which enable simultaneous measurement of a given peptide across 11 sample conditions in a single MS2 scan. Previous work used phosphoproteomics to compare nocodazole-induced phosphorylation across a panel of cancer cell lines[93]. This work, however, focused on long incubation times and mainly commented on mitosis-related phosphorylation, which is currently well studied.

We present the first global comparison of phospho-signaling induced by MT-stabilizing and destabilizing drugs in interphase retinal pigmented epithelial (RPE)-1 cells. For this, we employed TMT-based phosphoproteomics and quantified over 20,000 phosphopeptides. Our analysis reveals common and unique signaling to both classes of drug, sheds light on MAPK activity, and uncovers the prominence of phosphatase action in response to MT destabilization. Furthermore, we demonstrate a rapid increase in JNK activity without additional JNK activation in the case of MT stabilization in RPE1 cells, which we hypothesize is due to drug-induced inhibition of the opposing phosphatase(s).

3.4 Results

3.4.1 MT drug action can be kinetically aligned using EB3 comet analysis

To determine ideal drug concentrations to test for phosphoproteomic analysis, we decided to measure the response of MT dynamics to a panel of stabilizing and destabilizing drugs. Since MT stabilizing and destabilizing drugs have opposite effects on MT polymer in cells, we sought to determine

concentrations that would achieve similar rates of EB3 comet loss in live cells. We tested a small, but diverse, panel of drugs including paclitaxel (Ptx), epothilone-B (EpoB), combretastatin-A4 (Ca4), and eribulin (Erb). We show the binding modes of these drugs in an overlay of four published crystal and cryo-EM structures[47,51,150,151] (Fig. 3.1A). Since we could not find published structures for EpoB in complex with tubulin, we used a structure of epothilone-A instead, which differs by one methyl group. We conducted time-lapse imaging of EB3 comets in RPE1 cells expressing an EB3-GFP reporter (Fig. 3.1B, Supplementary Fig. 3.1). We tested a four-fold dilution series of these drugs and after quantifying the images, we concluded that the highest concentrations tested should be used for phosphoproteomic analysis. Note that for the stabilizing drugs, the data suggest that MTs are fully polymerized within 3-5 minutes (Fig. 3.1B), since the number of EB3 comets directly correlates with the number of growing MTs[152]. The kinetics of MT depolymerization after treatment with Erb or Ca4 is less obvious from the data, but we observed cell rounding for even the lowest doses tested (i.e. 50 and 25 nM, respectively) within 15 minutes (Supplementary Fig. 3.1), suggesting that at least some proportion of MTs had depolymerized within that time. MT depolymerization has previously been found to induce GEF-H1-mediated actin stress fiber formation and cell contractility[153,154].

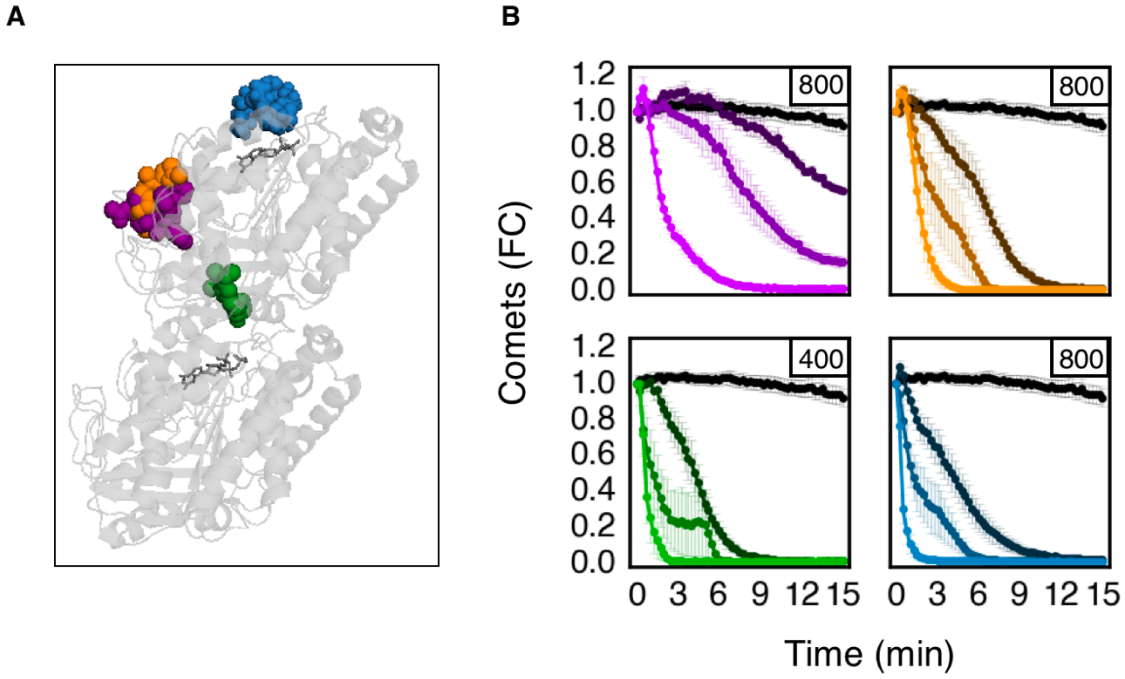

Figure 3.1. *Comparison of MT drug kinetics via EB3 comet imaging. (A) Overlay of published crystal and cryo-EM structures of Ptx (blue), Ca4 (green), Erb (purple), and epothilone-A (orange) in complex with dimeric tubulin (gray). PDBs: 1JFF, 1TVK, 5JH7, 5LYJ. (B) EB3 comet scoring for Ptx, CA4, Erb, and EpoB (same colors as in A). A four-fold dilution series is depicted for each drug. Darker hues denote lower doses (black for 0.1% DMSO control) whereas brighter hues denote higher doses. The boxed number in each plot denotes the highest dose tested (nM). Error bars denote standard error of the mean (N > 100 cells).*

3.4.2 Erb and EpoB stimulate time-dependent high-fold changes in the phosphoproteome

We proceeded by treating serum-deprived, contact-inhibited RPE1 cells with 800 nM Erb, 800 nM EpoB, or DMSO control over a 2-fold time series (Fig. 3.2A). We treated cells for as long as 2 hours and as short as 4 minutes in order to observe slower and quicker signaling that is stimulated by the drugs. Importantly, we normalized the serum-deprivation time for all conditions. After drug treatment, we aspirated the media and lysed quickly with a guanidine thiocyanate (GuSCN) buffer. In this way, protein was immediately denatured, making the use of phosphatase and protease inhibitors unnecessary. We proceeded with a typical protein-MS sample work-up utilizing isobaric TMTs to multiplex 10 conditions in a single MS run[85,155] (Fig. 3.2A, middle column). We then used MS/MS/MS to quantify the TMT reporter ions.

After searching the data to map the phosphopeptides on the proteome, we performed principal component analysis (PCA) for the Erb and EpoB datasets to reduce dimensionality and determine the principal cause of variance in the data. Looking at the first principal component (PC1), it was apparent that time accounted for the maximum variance observed for both Erb- and EpoB-induced phosphopeptides (Fig. 3.2B). We then assessed the magnitude of fold-changes observed in the data and determined that 8 and 6 percent of phosphopeptides changed more than 2-fold within 2 hours for Erb and EpoB, respectively. We also conducted null hypothesis testing to compute confidence scores with respect to duplicate reliability. For subsequent analysis, we used phosphopeptide measurements that were assigned confidence scores above 90 percent (Supplementary Fig. 3.2).

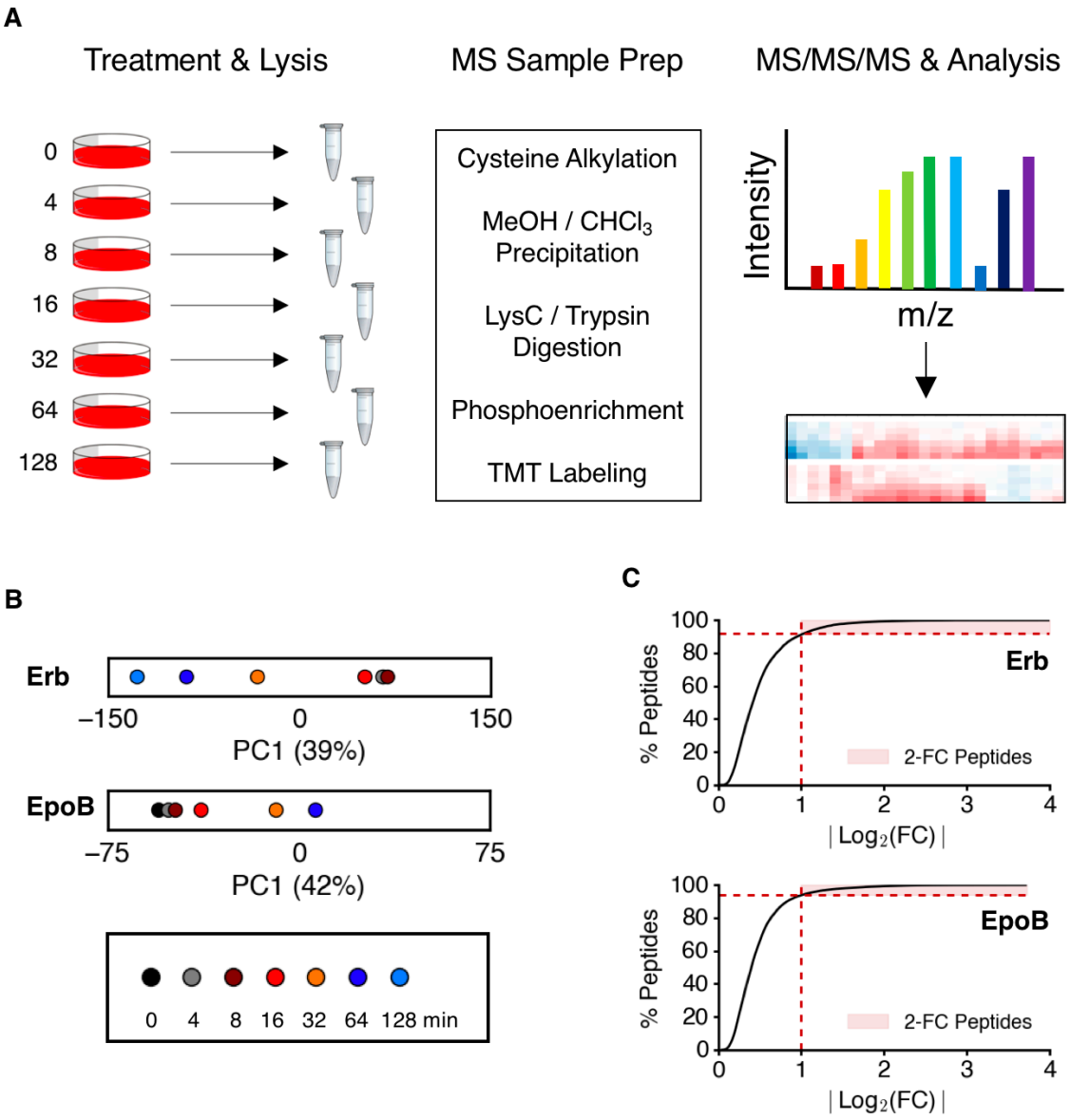

Figure 3.2. *Phosphoproteomics sample preparation and dimensionality reduction. (A) Workflow for treatment, lysis, and sample preparation to obtain TMT-labeled phosphopeptides and subsequent data analysis. (B) Principal component analysis (PCA) of phosphopeptide data obtained for Erb and EpoB. The variance accounted by the first principal component (PC1) is indicated in parentheses. (C) Cumulative distributions of log_2(FC) data for Erb and EpoB. Shaded region denotes phosphopeptides with greater than 2-fold change.*

3.4.3 Several pathways are stimulated by Erb and EpoB

To broadly assess which signaling pathways are stimulated by Erb or EpoB treatment, we used KEGG (Kyoto Encyclopedia of Genes and Genomes) pathway analysis. In Fig. 3.3A, we annotate a subset of pathways enriched for both Erb and EpoB ($p < 0.05$). This analysis revealed that several pathways, such as MAPK signaling and focal adhesion functionality, were over-represented by Erb phosphopeptides but under-represented by EpoB phosphopeptides. Exceptions to this observation included protein processing in the endoplasmic reticulum (ER) and phagosome regulation, which were over-represented for EpoB phosphopeptides. It was also obvious from this analysis that Erb stimulated many more pathways than EpoB, including regulation of the actin cytoskeleton, calcium signaling, and apoptosis (Supplementary Fig. 3.3). Intriguingly, Erb phosphopeptides also seemed to be enriched for immune-related signaling. On this note, previous work has suggested that GEF-H1 released from depolymerized MTs controls sensing of nucleic acids for antiviral host defenses[156].

To identify groups of correlated phosphopeptides, we utilized a custom-built factor analysis algorithm (Fig. 3.3B, Supplementary Fig. 3.4). Intriguingly, the top factor loadings for Erb were enriched for +TIPs and MAPs (e.g. CLIP1, MAP4) and proteins associated with the actin cytoskeleton (e.g. FMN2, ANLN, DBNL). The top factor loadings for EpoB were also enriched for +TIPs and MAPs, though these proteins (and phosphopeptides) were different than those enriched for Erb (Fig. 3.3B). In Fig. 3.3C, we show the representative phosphopeptides for MAP4 and CLIP1 identified by factor analysis for Erb. All of these peptides are being dephosphorylated and reside in vital regions of these proteins. The phosphosites for MAP4 occur in the MT-binding region of the protein. Dephosphorylation of these sites increases MAP4 affinity for MTs and may act to counter to drug response. The phosphosites for CLIP1 occur in a serine-rich region between the two CAP-Gly domains of the protein. Although the exact functionality of each of these CLIP1 sites is unknown, studies have shown that, similar to MAP4, dephosphorylation in this region can increase CLIP1 affinity for MTs[157]. Many other phosphopeptides were detected that hint at regulation of MTs and actin in response to Erb (Supplementary Fig. 3.5).

We then performed motif analysis using Motif-x[158,159] to determine enriched motifs among high-fold changing phosphopeptides. This approach only returned proline-directed motifs (i.e. S*P and T*P) for Erb

and EpoB phosphosites. These motifs, however, were present in a higher proportion of phosphopeptides for EpoB as compared to Erb (Fig. 3.3D), indicating that EpoB-stimulated signaling relies much more on proline-directed kinase activity.

Proline-directed phosphosites implicate a small panel of possible upstream kinases. Potential candidates include MAPKs (e.g. JNK, p38, ERK), CDKs, and GSK3ß. We therefore looked in our data for phosphosites that would further implicate any of these kinases. The c-Jun transcription factor was found to be phosphorylated at Ser63 after treatment with Erb (Fig. 3.3E; this peptide was not detected for EpoB), which primarily implicates JNK, though ERK1/2 can also phosphorylate this site under certain circumstances[160]. The activation sites for ERK1 and ERK2, as well as p38, were also present in the data, but these sites were only phosphorylated in the case of Erb. We also discovered phosphorylation of LMNA at either Thr19 or Ser22 (Supplementary Fig. 3.6), both of which would normally implicate CDK1[161]. Note that since we allowed our cells to contact inhibit each other, the mitotic index was very low prior to drug treatments (below 1%) which makes CDK1 activity very unlikely.

To visualize the global kinetics and directionality of all changing phosphopeptides, we clustered the data using a Pearson-based hierarchical clustering algorithm (Fig. 3.3F). This visualization of the data made it clear that a large wave of phosphorylation is induced by both drugs as fast as 4 minutes after drug treatment. This wave of phosphorylation accounted for the large majority of all changing phosphopeptides and suggests that the two drugs induce similar kinase activity to phosphorylate these sites. There were also noticeable differences between the drugs, however. For example, it was clear that there is a slower wave of phosphorylation that is induced by Erb but not EpoB (Fig. 3.3F, top left black box). There was also a kinetically similar wave of dephosphorylation specific to Erb (Fig. 3.3F, lower left black box). Fewer phosphopeptides were unique to EpoB, but we did observe a small cluster of phosphorylated sites that tracked differently for Erb (Fig. 3.3F, thin black box). We also annotated phosphoproteins with Uniprot identifiers for protein family assignment and likely cellular localization. Using “nucleus”, “nucleus speckle,” and “nucleus matrix” as Uniprot identifiers for cellular localization, we annotated phosphoproteins that were localized in the nucleus (Fig. 3.3F, barcode on right of heatmap). Surprisingly, nuclear sites were very enriched among all changing phosphopeptides.

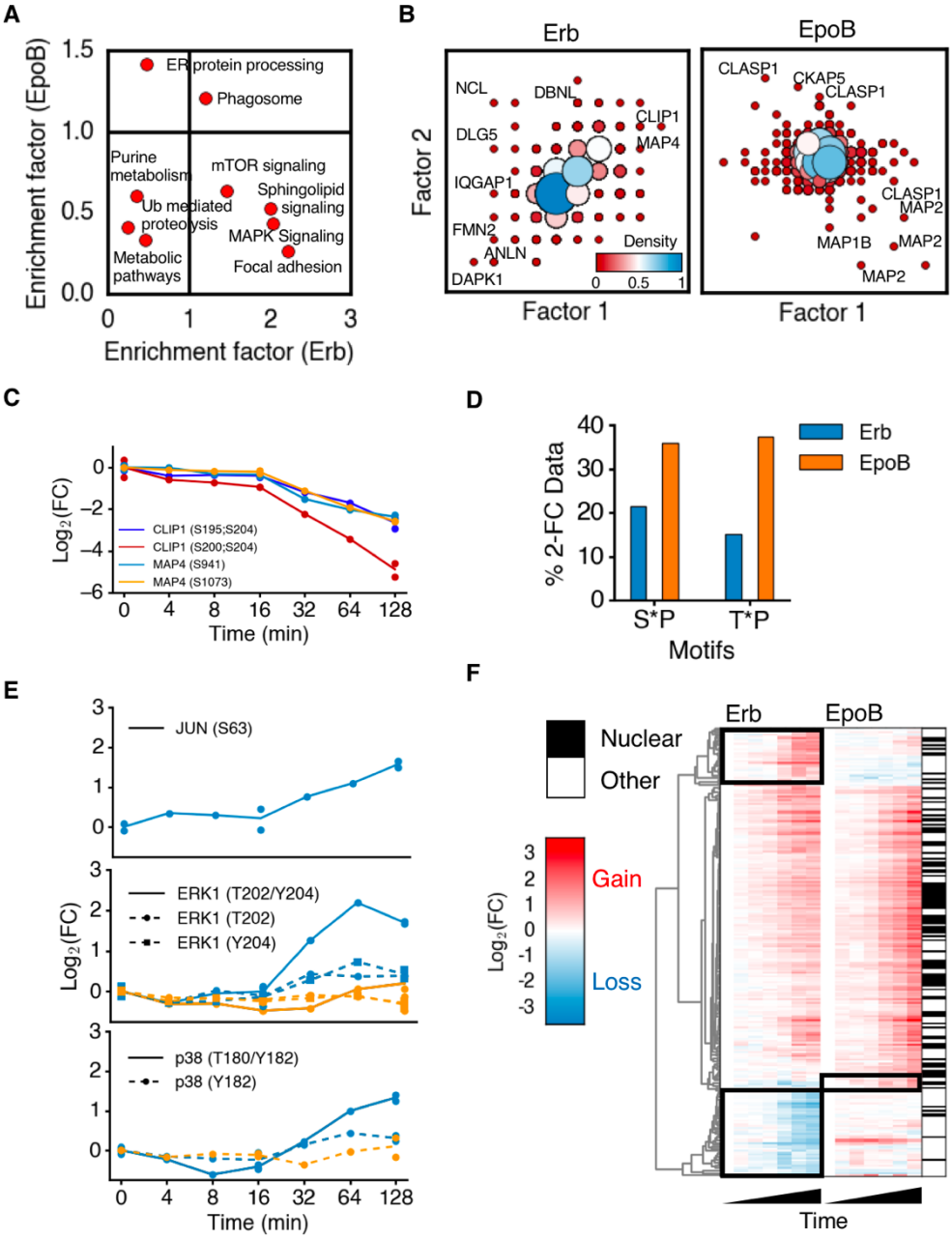

Figure 3.3. *Pathway analysis of phosphopeptide changes induced by Erb and EpoB. (A) Scatterplot shows statistically enriched KEGG pathways in the phosphoproteome induced by Erb and EpoB ($p < 0.05$, Fisher's exact test). Pathways that are over-represented have enrichment factors greater than 1, whereas under-represented pathways have enrichment factors less than 1. (B) Factor analysis of Erb and EpoB phosphopeptide data. Proteins among the top factor loadings are annotated. Protein density is denoted by both color and size. (C) Phosphopeptide profiles for MAP4 and CLIP1 phosphosites stimulated by Erb. (D) Percentages of high fold-change peptides that are proline-directed. (E) Phosphopeptide profiles for MAPK relevant phosphosites detected for Erb (blue) or EpoB (orange). (F) Hierarchical clustering of the phosphopeptides induced by Erb and EpoB. Nuclear phosphopeptides are denoted by black lines. Top left box encloses phosphorylation specific to Erb. Lower left box encloses dephosphorylation specific to Erb. Right box encloses phosphorylation specific to EpoB.*

3.4.4 JNK activity (not activation) is induced by EpoB

Thus far, the data implicated potential action of JNK, p38, ERK, and possibly CDKs for Erb, and just JNK or CDKs for EpoB. Since proline-directed directed phosphorylation constituted a larger proportion of EpoB phosphosites, we performed an additional phosphoproteomics experiment in RPE1 cells, this time with combinatorial drug treatments of EpoB and inhibitors for the 4 kinase families mentioned above (Fig. 3.4A). Cells were again grown to contact inhibition and serum-deprived prior to the 2-hour drug treatments. Importantly, we also tested the effects of the kinase inhibitors alone on cells. We clustered the data using the Fuzzy c-means algorithm which revealed that only JNK was responsible for the phosphorylation present in this new dataset (Fig. 3.4B, Supplementary Fig. 3.7). When visualizing these clusters in heatmap format, this result became even more obvious (Fig. 3.4C). Additionally, we found that JNK was responsible for the CDK1-annotated sites in LMNA (Supplementary Fig. 3.8). We mapped this smaller dataset of JNK-dependent phosphosites onto the previous Erb/EpoB time-course data and found that most all of these sites occurred in the cluster of sites that are highly correlated between the two drugs, with the exception of a few sites that occurred in phosphopeptides changing only for EpoB (Supplementary Fig. 3.10).

Since we did not detect phosphorylation of the JNK activation sites previously, we performed phospho-Western blot analysis of these sites. For this, we used Ca4 instead of Erb – we used MS to verify similar phosphorylation dephosphorylation induced by these two drugs (Supplementary Fig. 3.9A, B). Western blot analysis made it clear that treatment with an MT destabilizing drug induces activation of JNK (Fig. 3.4D). Strikingly, JNK was not activated after treatment with EpoB. Although this may be counterintuitive at first, this result indicates that net JNK activity has increased in the case of EpoB treatment without additional activation. We interpret the data as hinting at competition between JNK and an opposing phosphatase(s) and present a potential model for this in Fig. 3.5. In any case, the data point toward two different JNK pathways that are induced by MT-stabilizing vs. MT-destabilizing drugs.

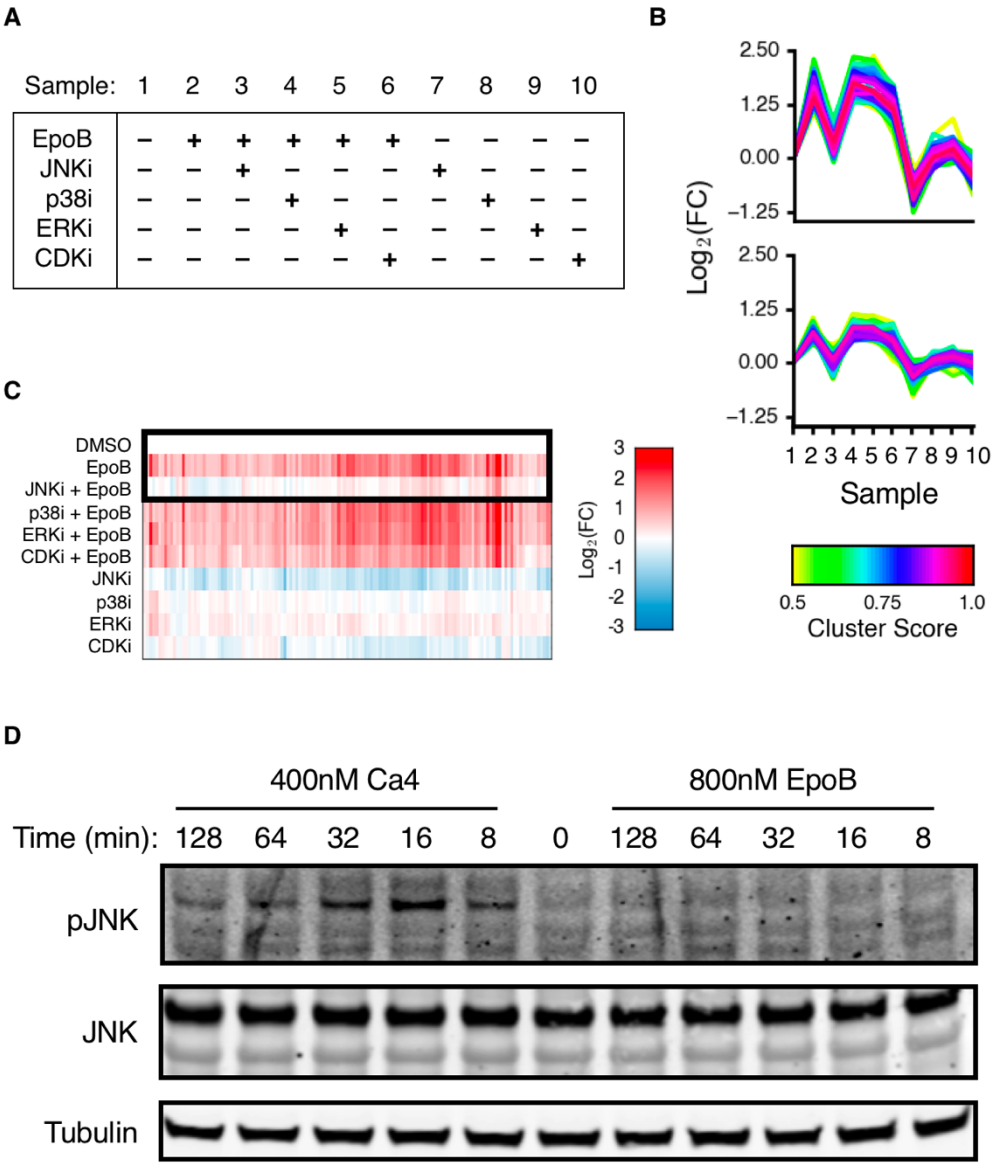

Figure 3.4. *JNK activity, but not activation, is responsible for EpoB-induced phosphorylation. (A) Experimental design to probe proline-directed kinases (JNK, p38, ERK, CDKs). (B) Fuzzy c-means clusters demonstrating JNK-dependent signaling stimulated by EpoB. Sample numbers are the same as in A. (C) Heatmap representation of the phosphopeptide profiles plotted in B. (D) Phospho-Western blot of JNK activation sites upon treatment with Ca4 or EpoB.*

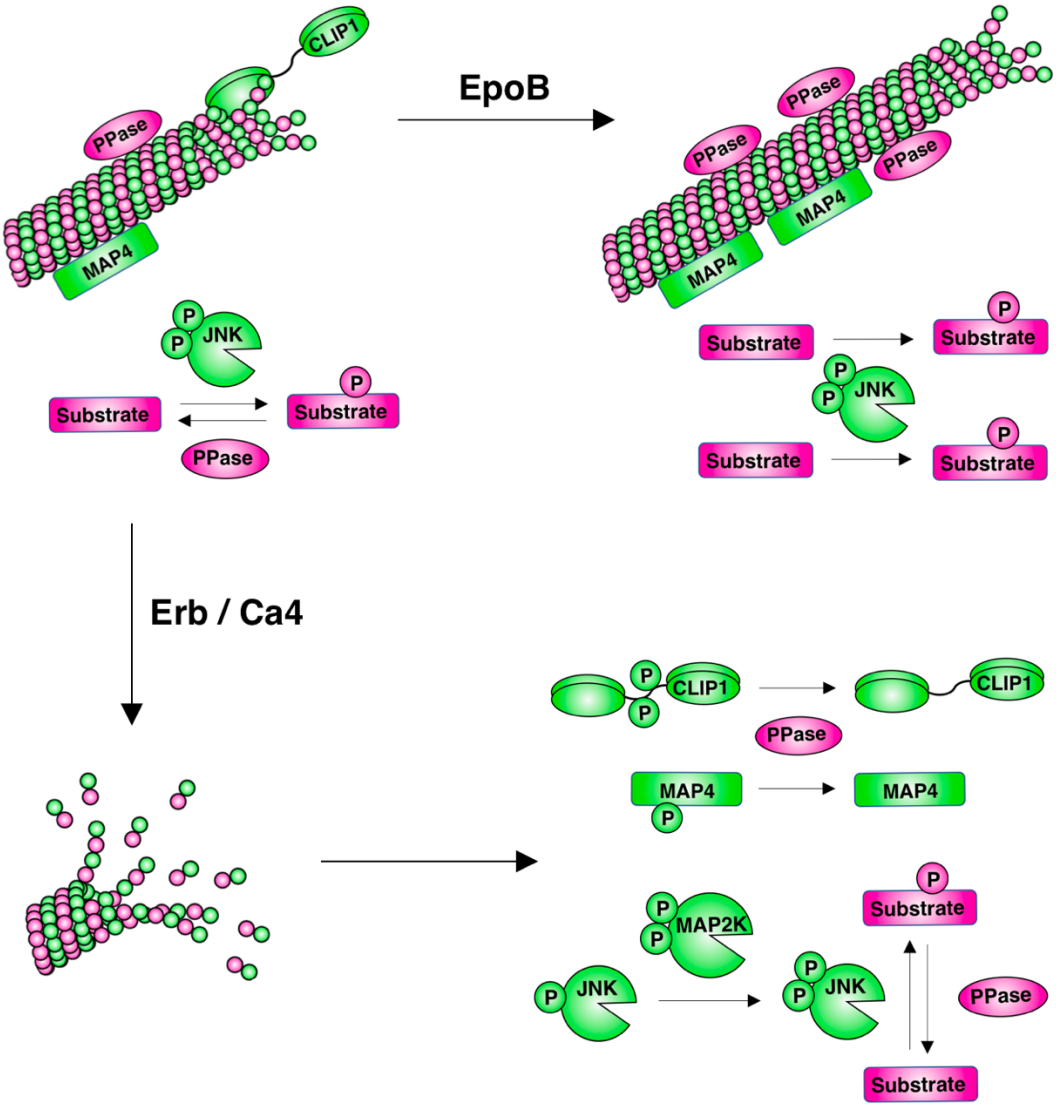

Figure 3.5. *Model of two MT-mediated pathways for stimulating JNK activity. EpoB stimulates MT polymerization and effectively inhibits the phosphatase whereas Erb, or Ca4, induces MT depolymerization into tubulin dimers, leading to JNK activation and phosphatase release from MTs.*

3.5 Discussion

We have conducted a global comparison of the interphase phosphorylation induced by an MT-stabilizing drug, EpoB, and an MT-destabilizing drug, Erb. We implemented the use of MS-based phosphoproteomics, which enabled us to multiplex two different time-courses and capture phospho-changes occurring as quickly as 4 minutes in serum-deprive cells. Importantly, we found that serum-deprivation had little effect on drug-induced changes other than partially accentuating most all of the phospho-changes observed (Supplementary Fig. 3.11). That being said, a small cluster of phosphopeptides was affected, but half of this cluster consisted of peptides from one large protein. The other affected peptides hinted at a difference in cell cycle regulation, suggesting that these divergent signals may be due to a small percentage of cells that were not fully contact-inhibited (Supplementary Fig. 3.11).

Simple dose-response experiments of EB3-GFP comet kinetics allowed us to align Erb and EpoB with respect to time-dependent loss of MT dynamics (Fig. 3.1B), which facilitated comparison for our phosphoproteomic analysis. Although less than 10 percent of phosphorylation changed after drug treatment, it was obvious that several signaling pathways, in addition to MAPK signaling, were induced by MT stabilization or destabilization (Fig. 3.3A). We observed that significantly more signaling pathways were induced by the destabilizing drugs (Supplementary Fig. 3.3 shows a subset of these). Intuitively, this may make sense considering that many signaling proteins bind to MTs *in vivo* and some are known to have functions that are inhibited by MT binding[153].

We were initially surprised by the enrichment of cytoskeleton-related proteins among our high-fold changing phosphopeptides. Factor analysis revealed that both MAPs and actin-binding proteins are phospho-regulated in response to MT destabilization, whereas primarily MAPs are affected by MT stabilization. The enrichment of actin-binding phosphoproteins is consistent with the idea that MT depolymerization mediates crosstalk with the actin cytoskeleton via release of the GEF-H1, which is required for Rho kinase activation and subsequent actin contractility[162]. Indeed, we observed contractile cell morphology induced by MT depolymerization for both Erb and Ca4 (Supplementary Fig. 3.1). Among the many MAP phosphosites that changed in our datasets, we noticed that several phosphosites occurred in regions that alter affinity for MTs. This was especially the case for MT destabilizing drugs. CLIP1 and

MAP4 were dephosphorylated in response to Erb (Fig. 3.3C), which would naturally increase their affinity for MTs. This may hint at a phospho-regulated compensatory response to MT destabilization: as MTs are depolymerized, a phosphatase dephosphorylates cytosolic MAPs to re-stabilize MTs. This idea may be further supported by the phosphorylation of stathmin at S25 in response to Erb (Supplementary Fig. 3.5), which inhibits stathmin-mediated sequestration of tubulin dimer and effectively stabilizes MTs[163].

Like others, we observed induction of the JNK, p38, and ERK signaling pathways in response to MT destabilization, as evidenced by phosphorylation of S63 of c-Jun, T202/Y204 of ERK1, and T180/Y183 of p38, respectively (Fig. 3.3E). ERK and p38 were not significantly activated in the case of EpoB treatment, though this may be due to the short duration of our treatment. We became particularly interested in the large cluster of phosphopeptides that were correlated between the two drugs. We performed combinatorial drug treatments to identify the kinase most responsible for this cluster. Phosphoproteomic analysis pointed exclusively at JNK as the kinase responsible (Fig. 3.4B, C). Although we did not perform combinatorial drug treatments for Erb, we believe that JNK is still largely responsible for the Erb side of this phosphopeptide cluster. This hypothesis is supported by the high correlation between the drugs in this cluster, the rapid nature of the phosphorylation, and the slower activation of ERK and p38 in response to Erb treatment. We also verified the quicker induction of JNK activation when using the same time-points and the same effective dose of Ca4 (Fig. 3.4D), which further supports this hypothesis. Nevertheless, it is possible that ERK and p38 might also phosphorylate these sites at later time-points. Strikingly, JNK was not activated in the case of EpoB treatment, although our phosphoproteomics data demonstrated an obvious increase in JNK-dependent phosphorylation. Realizing that phosphatase activity was induced by the depolymerization of MTs (Fig. 3.3F, lower left black box), and that some proline-directed sites were phosphorylated for EpoB but dephosphorylated for Erb (Fig. 3.3F, middle black box), we reasoned that a phosphatase (or multiple phosphatases) may be competing for these MAPK substrates.

We present a simple literature-supported model in Fig. 3.5. In our model, a pool of phosphatase is sequestered by MT affinity. Upon chemical-induced MT polymerization, the phosphatase becomes further sequestered and, thereby, inhibited. This allows for basally activated JNK to phosphorylate without competition from the opposing phosphatase. Upon treatment with a MT-destabilizing drug, however, the

phosphatase is released, allowing for the dephosphorylation of MAPs (and potential re-stabilization of MTs). Although more phosphatase is present to compete with JNK, an upstream MAPK is also activated by the MT disruption (or is basally active), allowing for quick JNK activation. The PP2A phosphatase has previously been found to associate with MTs[164] and bind to MAPs[165]. We conclude with this model of two different MT-mediated JNK pathways. Future work may elucidate the extent to which the EpoB-stimulated JNK pathway occurs in other cell types, especially those previously reported to have slow or little activation of JNK in response to MT stabilization.

3.6 Methods

3.6.1 Reagents and cell lines

EpoB and Ptx were purchased from MedChemExpress whereas Ca4 was purchased from Sigma-Aldrich. Erb was a generous gift from Ralph Weissleder at Mass General Hospital who purchased it from a clinic at MGH. In addition, JNK-IN-8, SCH772984, and dinaciclib were purchased from MedChemExpress, whereas VX-745 was obtained from Sigma-Aldrich. RPE1 cells expressing EB3-GFP were a generous gift from David Pellman at Harvard Medical School.

3.6.2 Cell culture

RPE1 cells expressing EB3-GFP were maintained in DMEM/F12 (Life Technologies) and supplemented with 10% FBS (GIBCO) (v/v) and 1% penicillin-streptomycin (Cellgro).

3.6.3 Live-cell microscopy and image acquisition

Each day prior to imaging, RPE1 cells were passaged to 25% confluency on 35-mm MatTek plates with glass coverslip bottoms. Media was replenished 3-4 hours before imaging. We imaged EB3 comets using a spinning-disk confocal microscope (Nikon) equipped with a 60x/1.42 NA Plan Apochromat objective, heated chamber, and MetaMorph acquisition software. 30 percent laser power was used with 500 millisecond exposure. Four fields were imaged per plate. Images were acquired every 15 seconds.

3.6.4 Image analysis

Images were analyzed using custom-built software in Python. Comet thresholding was performed separately for each imaging session (i.e. image fields that were obtained within the same imaging session were thresholded similarly). To do this, a Gaussian blur with 5-pixel radius was applied on a given field. This blurred image was then subtracted from the original image. The result of this subtraction was then used to threshold with respect to the first time-point, after which this threshold was applied onto all subsequent time-points for the same cell. The threshold was computed so to maximize the negative control-to-positive control comet ratio; later time-points of the DMSO control and highest drug dose were used for this. In order to count apparent image puncta as comets, we set a 3-20 pixel size filter. The median number of comets from all quantified fields for a given plate was computed at each time-point. The resultant array of comet medians was then normalized by the median cell area (as defined by cytosolic EB3-GFP) at each time point.

3.6.5 Mass spectrometry-based phosphoproteomics

For the Erb and EpoB time-course experiments, cells were grown to confluency on 15-cm plates until the visible mitotic index was below 1%. Cells were washed twice with PBS and then serum-deprived for 2.5 hours prior to drug treatments. The cells were then treated with either 800nM Erb, 800nM EpoB, or 0.01% DMSO control. Cell lysates were obtained at 4 minutes, 8 minutes, 16 minutes, 32 minutes, 64 minutes, or 128 minutes after drug treatment. DMSO control lysates were procured after treating for 64 or 128 minutes. Biological duplicates were obtained for the DMSO control as well as for the 16-min and 128-min time-points. Note: all cells were serum-deprived for 4.5 hours including treatment time. Cells were lysed by aspirating the serum-deprived media and immediately pipetting 2 mL of 5 M GuSCN buffered with 100 mM HEPES, pH 7.2. For each lysate, 4mg of protein was utilized to carry forward with phosphoproteomics sample preparation. Cysteines were alkylated using N-ethylmaleimide (NEM). To do this, samples were heated to 60°C for 20 minutes in the presence of 5 mM DTT, then cooled to room temperature (RT), after which 15 mM NEM was added for 20 minutes. The alkylation reaction was then quenched with 5 mM DTT. Proteins were then purified by methanol/chloroform precipitation in 50-mL Falcon tubes[166]. Protein pellets

were resuspended (~5 mg/mL) in freshly prepared 8 M urea buffered with 10 mM 3-[4-(2-hydroxyethyl)-1-piperazinyl]propanesulfonic acid (EPPS), pH 8.5; dissolution was aided by gentle flicking, pipetting, and heating at 37ºC for 15 minutes. The samples were then diluted to 4 M urea with 10 mM EPPS, pH 8.5, and digested with LysC (Wako Chemicals) at 10 ng/μL at RT for 14 hours. Then samples were diluted to 1.6 M urea with 10 mM EPPS, pH 8.5, and further digested with 10 ng/μL LysC and 5 ng/μL trypsin (Promega) at 37ºC for 8 hours in an incubator. The samples were then acidified with phosphoric acid (final concentration: 5%), desalted using C18 Sep-Pak cartridges (Waters), and dried down. Phosphopeptides were enriched using titanium dioxide microspheres as previously described[89]. After phosphoenrichment, samples were once again acidified and desalted as described above. The dried samples were then resuspended to 1 mg/ml with 200 mM EPPS, pH 8.0. For TMT labeling, 15 μL of TMT stock solution (0.8 mg in 40 μL acetonitrile) was added per 100 μg of peptide. After 2 hours of incubation at RT, the TMT reaction was quenched with 10 mM hydroxylamine for 15 minutes. All samples for a given 10-plex sample set were then combined, acidified by addition of phosphoric acid to 5%, clarified via centrifugation at 20,000 RCF for 30 minutes, and desalted as described above. To reduce sample complexity, peptides were fractionated into a 96-well plate by reverse-phase HLPC using an acetonitrile gradient. The resultant 96 fractions were pooled into 24 fractions by combining alternating wells from each column (i.e. one column produced 2 fractions). Each fraction was dried down, resuspended in 1% formic acid and 0.1% trifluoroacetic acid, and desalted using the C18 StageTip procedure[167]. The fractionated samples were processed using an Orbitrap Fusion Lumos mass spectrometer (Thermo Fisher Scientific) using a multi-notch MS3 method[22,23]. The raw data were converted to mzXML and searched using Sequest[79] against a concatenated Uniprot database. To distinguish forward and reverse hits, linear discriminate analysis was used, with reverse hits filtered to an FDR of 1% at the protein level. The A-score method was used to assess confidence in phosphosite localization[149]. Reporter ion intensities were quantified and normalized as previously described[168].

For the combinatorial drug treatment experiment, cells were grown to confluency until the visible mitotic index was below 1%. Cells were washed twice with PBS and then serum-deprived for 1.5 hours prior to any drug treatments. The cells were then treated with 200 nM JNK-IN-8, 200 nM VX-745, 80 nM SCH772984, 80 nM dinaciclib, or 0.002% DMSO for 1 hour. Cells were then co-treated with 800 nM EPO,

or 0.008% DMSO, and the corresponding kinase inhibitor (same concentrations as above). After 128 minutes of co-treatment, cells were lysed using 5 M GuSCN buffered with 100 mM HEPES, pH 7.2. Samples were prepared for MS phosphoproteomics as above.

For the serum-deprived Ca4 time-course, cells were grown to confluency until the visible mitotic index was below 1%. Cells were washed twice with PBS and then serum-deprived for 2.5 hours prior to drug treatments. The cells were then treated with either 400 nM Ca4 or 0.01% DMSO control. Cell lysates were obtained at 4 minutes, 8 minutes, 16 minutes, or 32 minutes after drug treatment. Cells were lysed as described above for the other time-courses. Samples were also prepared for MS phosphoproteomics as above.

For the serum-containing Ca4 time-course, cells were grown to confluency until the visible mitotic index was below 1%. Serum-containing media was replenished 2.5 hours prior to drug treatments. The cells were then treated with either 400 nM Ca4 or 0.01% DMSO control. Cell lysates were obtained at 4 minutes, 8 minutes, 16 minutes, or 32 minutes after drug treatment. For lysis, cells were first washed twice with ice-cold PBS on a bed of wet ice and lysed with 5 M GuSCN buffered with 100 mM HEPES, pH 7.2, as above. Samples were prepared for MS phosphoproteomics as above.

3.6.6 Principal component analysis

PCA was performed using custom-written code in Python. The full phosphoproteomic datasets were used for the computation, with Log_2(FC)-transformed values. Only the first principal component (PC1) was retained in order to determine the source of maximum variance.

3.6.7 Confidence score generation from internal duplicates

For every 10-plex peptide profile, we tested the null hypothesis that the duplicates match by chance. To do this, we computed the Euclidean distance between the two vector duplicates according to equation (3.1) below:

(3.1) $$D = \sqrt{(x_1 - y_1)^2 + (x_2 - y_2)^2 + (x_3 - y_3)^2}$$

For the Erb and EpoB time-courses, the DMSO control, 16-min, and 128-min time-points were defined by x_1, x_2, and x_3, respectively, or by y_1, y_2, and y_3, respectively. Then the time-points labels were randomized, and the Euclidean distance of the randomized values was computed. This randomized Euclidean distance calculation was performed 1,000 times to obtain confidence values with precision up to the second decimal place.

3.6.8 KEGG pathway analysis

For pathway analysis, phosphopeptides with 90% duplicate confidence and greater than 2-fold change were used. Pathways were searched separately for Erb and EpoB phosphopeptides using the Kyoto Encyclopedia of Genes and Genomes. Statistically significant pathways (determined by Fisher's exact test) were annotated as being enriched for Erb, EpoB, or both.

3.6.9 Factor analysis

Factor analysis was performed using custom-written code in Python. The algorithm used first employs standard PCA analysis, after which it performs a mathematical rotation on the PCA loadings to satisfy the varimax criterion[169] (i.e. the algorithm would maximize peptide profile variance while minimizing principal component/factor variance). Phosphopeptides with 90% duplicate confidence and greater than 2-fold change were used for the analysis, which was performed separately for Erb and EpoB.

3.6.10 Motif Analysis

Phosphosite motif analysis was performed using Motif-x[158,159]. The significance cutoff was set to 10^{-6}, peptide width was set to 13 amino acids, and the minimum number of occurrences to call a motif was set to 20. Motifs obtained in this manner were subsequently reassigned to the corresponding phosphopeptides. Only phosphopeptides with 90% duplicate confidence and greater than 2-fold change were used for the analysis, which was performed separately for Erb and EpoB.

3.6.11 Fuzzy c-means clustering

FCM clustering was performed using custom-written code in Python. The regularization parameter was set to 2.0 to deter unique peptides from driving cluster construction. The algorithm was employed on the Log_2(FC)-transformed data obtained for the combinatorial drug treatment experiment. Phosphopeptide data with greater than 1.5-fold change were used for the analysis.

3.6.12 Western blots

For Western blot analysis, cell lysates were prepared in buffer containing 100 mM Tris-HCl (pH 6.8), 20% glycerol, 4% SDS, 0.2% bromophenol blue, 200 mM DTT, and 2% ß-mercaptoethanol. 20 μg of cell lysate was added per gel lane. Primary rabbit antibodies for JNK and phospho-JNK (pT183/pY185) were purchased from Santa Cruz Biotechnology and Cell Signaling, respectively, and used at 1:1000 dilutions. Primary mouse antibody for α-tubulin was purchased from Sigma-Aldrich and used at a 1:10,000 dilution. Primary staining was performed overnight at 4ºC. Secondary anti-rabbit IgG (800CW) and anti-mouse IgG (680RD) antibodies were purchased from LI-COR and were used at 1:15,000 dilutions.

3.7 Acknowledgements

This work was supported by NIH grant GM39565. J.J.P. was supported by a Ruth Kirschstein fellowship (GM117882-02) from NIH-GM. We thank the Nikon Imaging Center at HMS for microscopy support and the Lab of Systems Pharmacology for mass spectrometry support. We also thank David Pellman (HMS) for gifting us with RPE1 cells expressing EB3-GFP.

Chapter 4

Multiplexed EB3 comet counting provides a quantitative biomarker for anti-tubulin drugs and reveals drug-induced single-cell heterogeneity

Javier J. Pineda, Sergine Brutus, Timothy J. Mitchison

4.1 Attributions

The following chapter describes an approach that I developed with help from Sergine Brutus to image, detect, and quantify EB3 comet counts in a multiplexed format (i.e. using 384-well plates). We used this framework to score EB3 comets for a diverse panel of anti-tubulin drugs and also used single-cell segmentation to assess the heterogeneity of cellular response to these drugs.

I designed the experimental set-up (with Sergine) as well as the entire single-cell EB3 image analysis pipeline, including all relevant coding in Python and ImageJ. Dr. Timothy Mitchison suggested that I construct models to fit to the acquired data. In response, I derived and implemented the models described below, which allowed us to further analyze and comment on these data. Finally, I developed the method described below for back-calculating background to obtain true comet signal in single cells.

4.2 Abstract

The dynamic instability of microtubules is a critical phenomenon that regulates several biological processes in cells. Quantification of microtubule dynamics has been made possible in recent years but has been limited in imaging throughput and single-cell analysis. Here we describe a new experimental and computational approach to quantify microtubule dynamics. We conduct highly multiplexed quantification of EB3 comet counts in live cells and use custom-built algorithms to segment single cells, thereby affording large-scale single-cell analysis. Using a dry objective lens and an automated image analysis pipeline, we were able to obtain acceptable signal-to-noise ratios, reliably quantify comets, and subtract false positives. Finally, we used our method to validate EB3 comet counts as a biomarker for anti-tubulin drug action and to assess the heterogeneity of single cells in response to microtubule poisons. We conclude that these mechanistically diverse drugs stimulate an increase in single-cell heterogeneity that is independent of drug efflux pump action.

4.3 Introduction

Microtubules (MTs) are dynamic polymers that stochastically grow and shrink on the order of seconds to minutes[18]. The extent of their dynamicity can be quantified by tracking fluorescently labeled

MTs or by tracking their growing plus-ends, for example, via fluorescently labeled plus-end tracking proteins (+TIPs), such as EB1 or EB3[75,170–172]. The resultant images contain comet-like puncta that represent the growing ends of MTs. Using available software such as plusTipTracker[171]. users can obtain growth rates of MTs via EB comet trajectories under different conditions, for example, treatment of cells with MT poisons.

While comet tracking software has afforded quantitative insights into MT dynamics, the conventional microscope set-up and analysis pipeline for obtaining this quantitative information has notable disadvantages. In order to obtain exceptional signal-to-noise for comet tracking, users tend toward oil-immersion objectives which makes it impractical to scale-up this technology. Work has been published that highlights automated screening of biological conditions using comet tracking, but the main automation used was for image analysis and the size of the screens were too small to be useful for more demanding biological or pharmacological questions[173,174]. In addition, tracking EB comet velocities requires frequent image acquisitions to reliably track comets over subsequent frames, a requirement that can incur significant photobleaching and potential phototoxicity, especially when using a confocal set-up. Photobleaching can be mostly avoided by using the state-of-the-art lattice light sheet microscope[74], but this limits the user to imaging one condition at a time, again severely limiting the throughput of image acquisition. This limit in image acquisition throughput has made a range of questions regarding MTs unfeasible to answer, such as the response of MT dynamics to many different cellular stresses, or the degree of heterogeneity in MT dynamics with respect to single cells – basally or in response to MT poisons. Some have tried to conduct single-cell analysis of EB comet tracking but have obtained data for far too few cells to offer any well-supported new biological insights[175]. The impracticality, as mentioned above, lies in the conventional use of oil-immersion objectives, which limits throughput of image acquisition, and also in manual segmentation of single cells, which limits throughput of image analysis.

Here we describe a new experimental and computational strategy that substantially improves the throughput of both EB comet image acquisition and single-cell image analysis. Our method relies on the use of EB3 comet *counting*, which allows for more infrequent image acquisitions. We have conducted kinetic experiments on 384-well plates and have used a DNA dye, SiR-DNA[176], to conduct single-cell segmentation and quantify comet counts over time for single cells. We used our method to validate EB3

comet counting as a universal biomarker of anti-tubulin drugs and we imaged and quantified single-cell MT dynamics for several thousand cells in less than 24 hours. In this manner, we have discovered, for the first time, that MT poisons stimulate an increase in cellular heterogeneity that is independent of drug efflux pump action.

4.4 Results

4.4.1 EB3 comet counting can be used to score MT dynamics

To score MT dynamics, we imaged an EB3-GFP reporter in RPE1 cells before treatment with anti-tubulin drugs in the presence of 10 μM verapamil, a pan-inhibitor of efflux drug pumps[123]. We then drugged the cells and immediately resumed image acquisition every 60 (for higher drug doses) or 90 seconds (for lower drug doses). Depending on the drug dose used (e.g. 10nM combretastin-A4, or Ca4), we could observe complete loss of comets with 20 minutes (Fig. 4.1A). In order to scale the amount of data acquired with this method, we decided to carry all subsequent experiments in 384-well imaging plates and stain cells with SiR-DNA (SirD), a nuclear dye for live cells[176]. This dye, which has advantageous fluorogenic properties for nuclear segmentation, has previously been found to affect cell cycle progression in RPE1 cells at concentrations at or above 250nM[177]. For this reason, we maintained SirD at 100nM in our experiments. This SirD concentration still allowed us to utilize watershed and voronoi algorithms to segment single cells (Fig. 4.1B). For segmenting EB3 comets, we realized that it was simple to manually choose a threshold so to avoid background pixels to be falsely counted as comets. We also realized, however, that in the case of many cells, it was difficult – if not impossible – to not pick up background as comets (i.e. false positives) at the later time-points of our drug-treated time-courses (Fig. 4.1C, solid green line). The increase in background intensities toward the end of these time-courses is due to increased EB3-GFP in the cytosol and is to be expected. Although true comet loss was obvious at high doses of anti-tubulin drugs, we were less confident in quantifying EB3 comets at intermediate doses without knowing the amount of cytosolic background for each cell. We realized, however, that we could add saturating drug (i.e. 4 μM Ca4) to force eliminate all comets at the end of any given time-course, which allowed us to determine the background cytosolic EB3 intensity for each single cell. We used this to write a background correction algorithm that

could back-calculate true signal at each point in the time-course (Fig. 4.1C, dotted green line). In some cases, cells did not have noticeable background, so our background correction algorithm did not really alter these trends (Fig. 4.1C, solid and dotted black lines). The use of our background correction algorithm also allowed us to automate thresholding for every single cell on our 384-well plates (Supplementary Fig. 4.1). Importantly, our DMSO control wells showed little to no photo-bleaching during our time-courses.

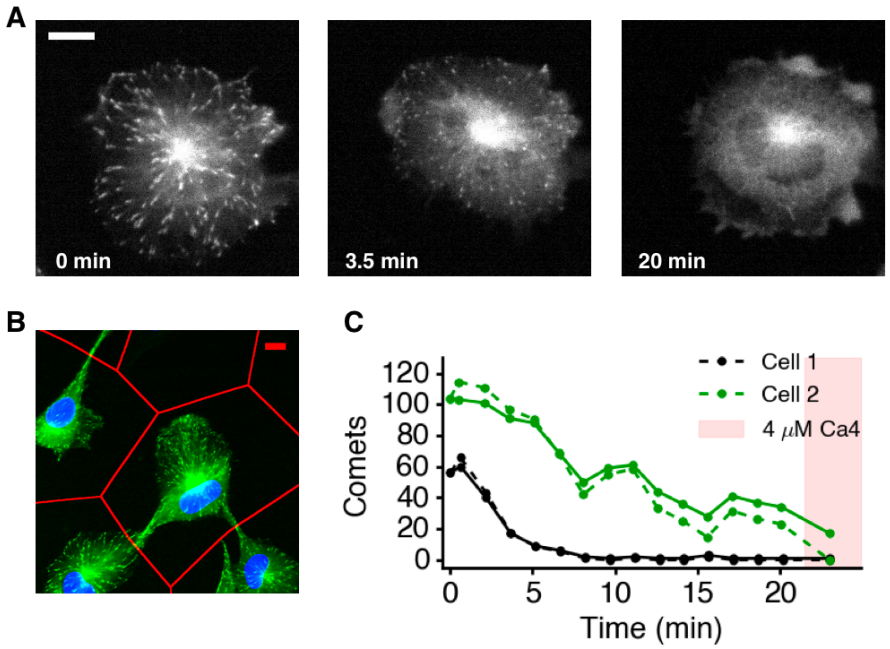

Figure 4.1. *Single cells can be segmented and scored for EB3 comets. (A) Representative single-cell time-lapse. The cell was imaged once, then treated with 10nM Ca4, then imaged over the course of 20 minutes. Scale bar: 10μm. (B) Example of single-cell segmentation using watershed and voronoi algorithms. Nuclei were stained with 100nM SiR-DNA (blue). The nuclear stain was used to define voronoi regions (red) and segment single cells (green). Scale bar: 10μm. (C) Raw and corrected comet count profiles are plotted for two individual cells. The solid curves denote the raw profiles for each cell. 4μM Ca4 was used to induce complete comet loss and define cytosolic background after each time-course (shaded pink region). The cytosolic background was then used to correct the cell comet profiles (dotted curves).*

4.4.2 EB3 comet counts measure endogenous single-cell heterogeneity

After we determined how to reliably quantify EB3 comets, we proceeded to characterize drug responses at the single-cell level. We used four drugs: epothilone-B (EpoB) and paclitaxel (Ptx) to represent the taxane site[97,178], Ca4 to represent the colchicine site[43], and vinblastine (Vnb) to represent the vinca

site[50]. Fig. 4.2 shows data for each of the drugs at 3 different doses. We observed noticeable single-cell heterogeneity in the presence of DMSO and lower doses of drugs whereas this heterogeneity appeared to reduce at high doses of drug. We also were able to capture a transient increase in EB3 comets induced by the stabilizing drugs EpoB and Ptx (Fig. 4.2B, magnified peaks, top right). These peaks are likely due to ectopic nucleation of MTs being stimulated immediately after drug uptake.

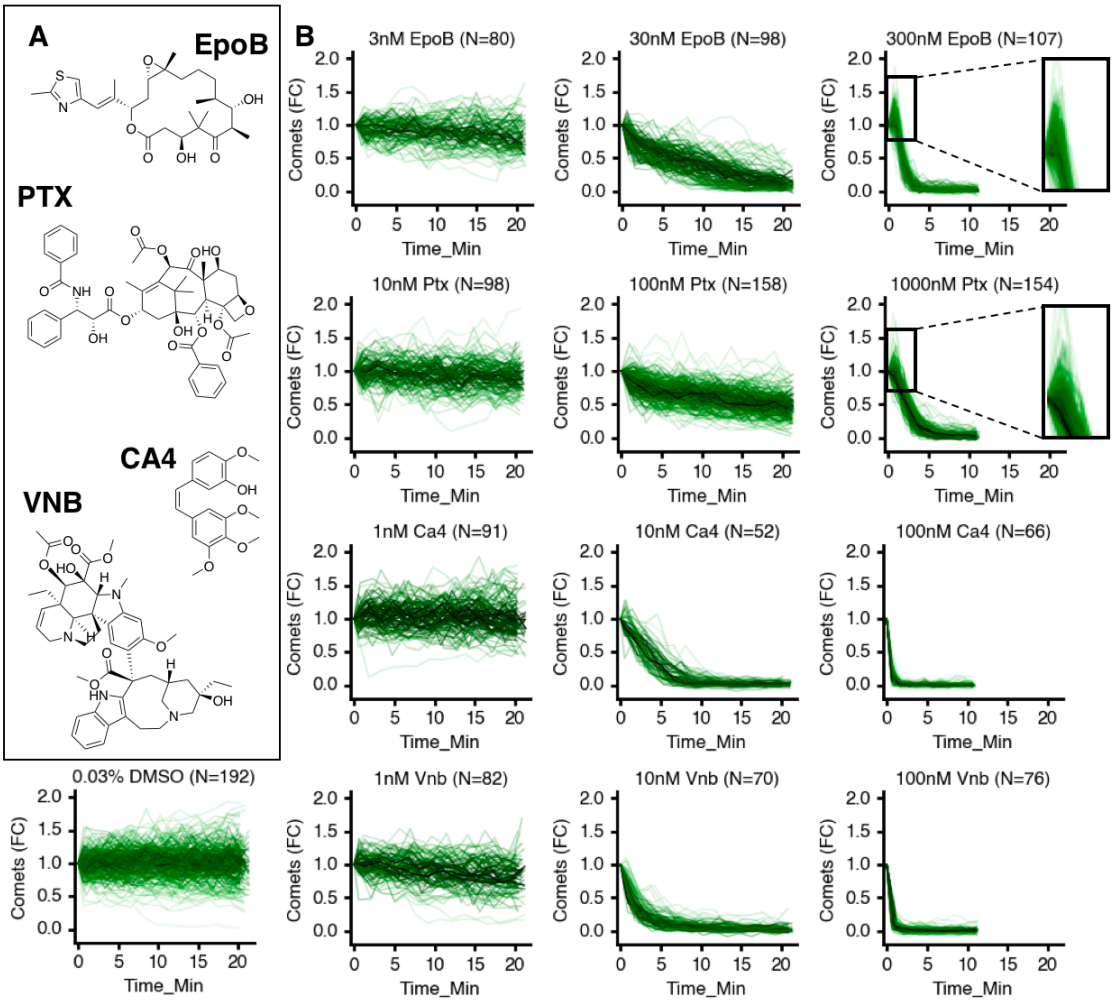

Figure 4.2. *Single-cell EB3 data for four microtubule drugs. (A) Chemical structures are shown for EpoB, Ptx, Ca4, and Vnb. (B) Single-cell EB3 comet counts are shown for three doses of each drug in A. Cells with at least 50 comets before drug treatment and less than 10 percent background were included in the analysis. The number of cell profiles in each plot is denoted in parentheses. The black boxes magnify the transient comet increases observed for EpoB and Ptx.*

4.4.3 EB3 comet counts can be modeled with simple biochemical models

To model the single-cell data, we derived simple biochemical equations with respect to the taxane site, colchicine site, and vinca site, i.e. equations (4.1-4.3). For convenience, we assumed passive diffusion in equation (4.4) for each of the drugs:

(4.1) $$N_{FC}^{comets} = e^{-kt}\left(\frac{[D]_{in}}{K_d^D[MT]_{FC,\,max}} + 1\right)$$

(4.2) $$N_{FC}^{comets} = e^{-k[D]_{in}}\left(\frac{[D]_{in}}{K_d^D} - \frac{[D]_{in}}{K_d^D[MT]_{FC,\,max}} + 1\right)$$

(4.3) $$N_{FC}^{comets} = e^{-k[D]_{in}}\left(\frac{[D]_{in}}{K_d^D[MT]_{FC,\,max}} + 1\right)$$

(4.4) $$[D]_{in} = [D]_{out}\left(1 - e^{-k_{diff}\,t}\right)$$

In our model, there are four necessary parameters, namely the binding constant of the drug (or K_d), the drug diffusion constant (or k_{diff}), the dose-dependent polymerization/depolymerization constant (or k_{pol}), and the ratio of total tubulin divided by initial polymerized tubulin (or $[MT]_{FC,\,max}$). We validated out model on the averaged single-cell data using drug binding constants from the literature[43,50,122,179] (Fig. 4.3A-D). We determined that $[MT]_{FC,\,max}$ was approximately 2.0, which is consistent with previous modeling we have conducted for MTs in RPE1 cells, whereas diffusion constants and polymerization constants were drug dependent. Our model provided exceptional fits for Ca4 and Vnb (Fig. 4.3C, D), and also for EpoB and Ptx at higher drug doses (Fig. 4.3A, B). Our model did not fit as well at lower doses of stabilizers, but we suspect that model fitting would be improved with a greater number of cells.

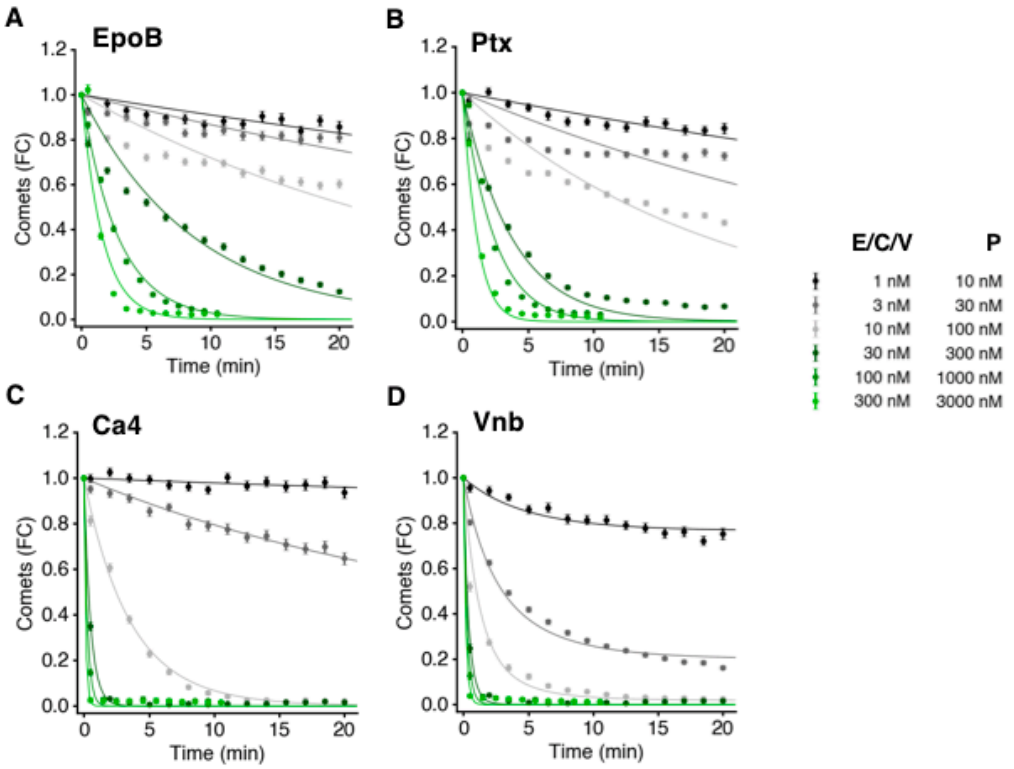

Figure 4.3. *Modeling of averaged comet data. (A) Single-cell comet profiles were averaged for 6 doses of EpoB. Equation (4.1) and (4.4) was used to obtain best-fit lines for these data. (B) Single-cell comet profiles were averaged for 6 doses of Ptx. Equation (4.1) and (4.4) was used to obtain best-fit lines for these data. (C) Single-cell comet profiles were averaged for 6 doses of Ca4. Equations (4.2) and (4.4) were used to obtain best-fit lines for these data. (D) Single-cell comet profiles were averaged for 6 doses of Vnb. Equations (4.3) and (4.4) were used to obtain best-fit lines for these data. Single-cell comet profiles containing at least 35 comets before drug treatment and less than 20 percent cytosolic background were used to obtain the averaged values in A-D. Error bars denote standard error. N = 95 cells for 30 nM Ca4. N > 100 cells for all other data points.*

After validating our models on our averaged data, we then sought to model our single-cell data. In Fig. 4.4A, we have replotted the corrected data for cell 2 from Fig. 4.1C. We also show the modeled curve for this data. Hereafter, we assess model fit by using a negative $\log_{10}$-transformation of residual mean-squared-error (NLM). In the case of Fig. 4.4A, goodness of fit was acceptable with an NLM of 2. We proceeded to model the data from all of the 4700 imaged cells and kept all modeled data that had an NLM

of at least 1.3. More than 97 percent of our single-cell data passed this cut-off (Fig. 4.4B). Fig. 4.4C shows modeled data for three doses of EpoB and Vnb. DMSO control indicated basal heterogeneity, though it should be noted that many more cells were imaged for this condition. We found that 75 percent of DMSO cells resided between 0.5 – 1.25 comet fold-change (Supplementary Fig. 4.2; Fig. 4.4C, red box).

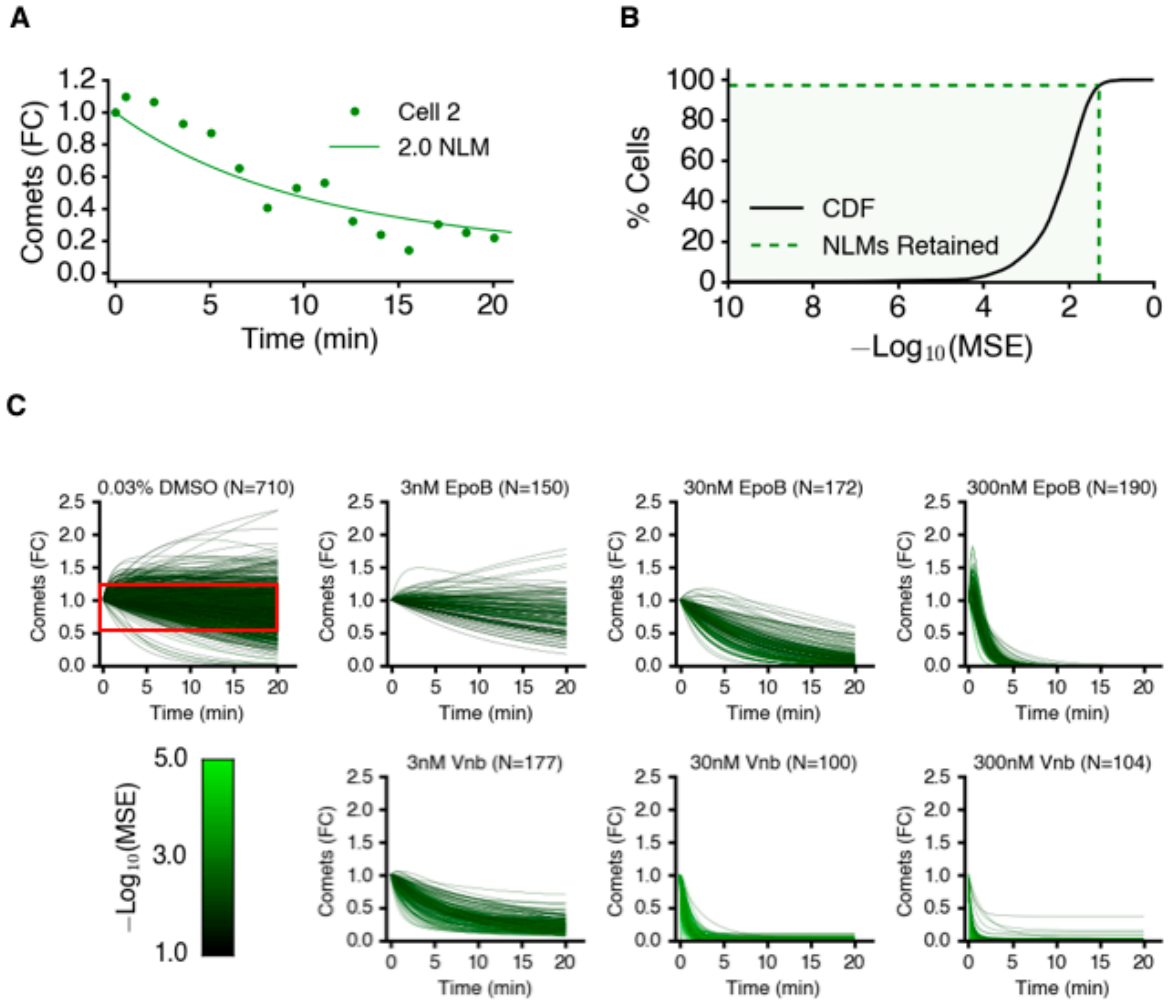

Figure 4.4. *Modeling of single-cell comet data. (A) The comet profile for cell 2 from Fig. 4.1C has been replotted. The solid line represents the best fit curve using equations (2) and (4). NLM denotes the negative log10 transformation of the curves mean-squared-error. (B) The cumulative distribution function shows the distribution of NLMs across all of the modelled single-cell comet data. The green dotted lines denote the NLM cut-off for well-modeled data and the proportion of modeled data that was retained after imposing this cut-off. (C) Modeled single-cell curves are shown for one dose of each drug tested. The number of modeled single-cell profiles depicted on each plot is indicated in parentheses. Curves have been color-coded with respect to the negative log_{10} transformation of respective mean-squared-error. Red box in DMSO plot encloses 75 percent of DMSO single cells with respect to the final time-point.*

4.4.4 EB3 comet counts reveal single-cell heterogeneity in response to MT drugs

After validating that our models faithfully recapitulated our single-cell data, we sought to quantitatively assess whether heterogeneity was exhibited by these curves, and whether MT poisons stimulated any additional heterogeneity in cells compared to DMSO alone. To do this, we computed the area-under-the-curve (AUC) for all of the modeled single-cell curves (Fig. 4.5A-D). To facilitate comparison between drug conditions, we normalized the interquartile ranges (IQRs) of the AUCs by their respective medians. We then renormalized these values with respect to DMSO control to obtain fold-change. When plotting all of the normalized IQRs with respect to drug concentration, it became obvious that some of the drugs have a higher-dose regime where additional single-cell heterogeneity is stimulated (Fig. 4.5E-H). This regime was noticeably broader for the MT destabilizing drugs Ca4 and Vnb. We also noticed a statistically significant degree of heterogeneity measured for Ptx at 300 nM. A similar peak was observed for EpoB at 30 nM, but this peak was not scored as being statistically significant, perhaps due to a need for a greater number of cells.

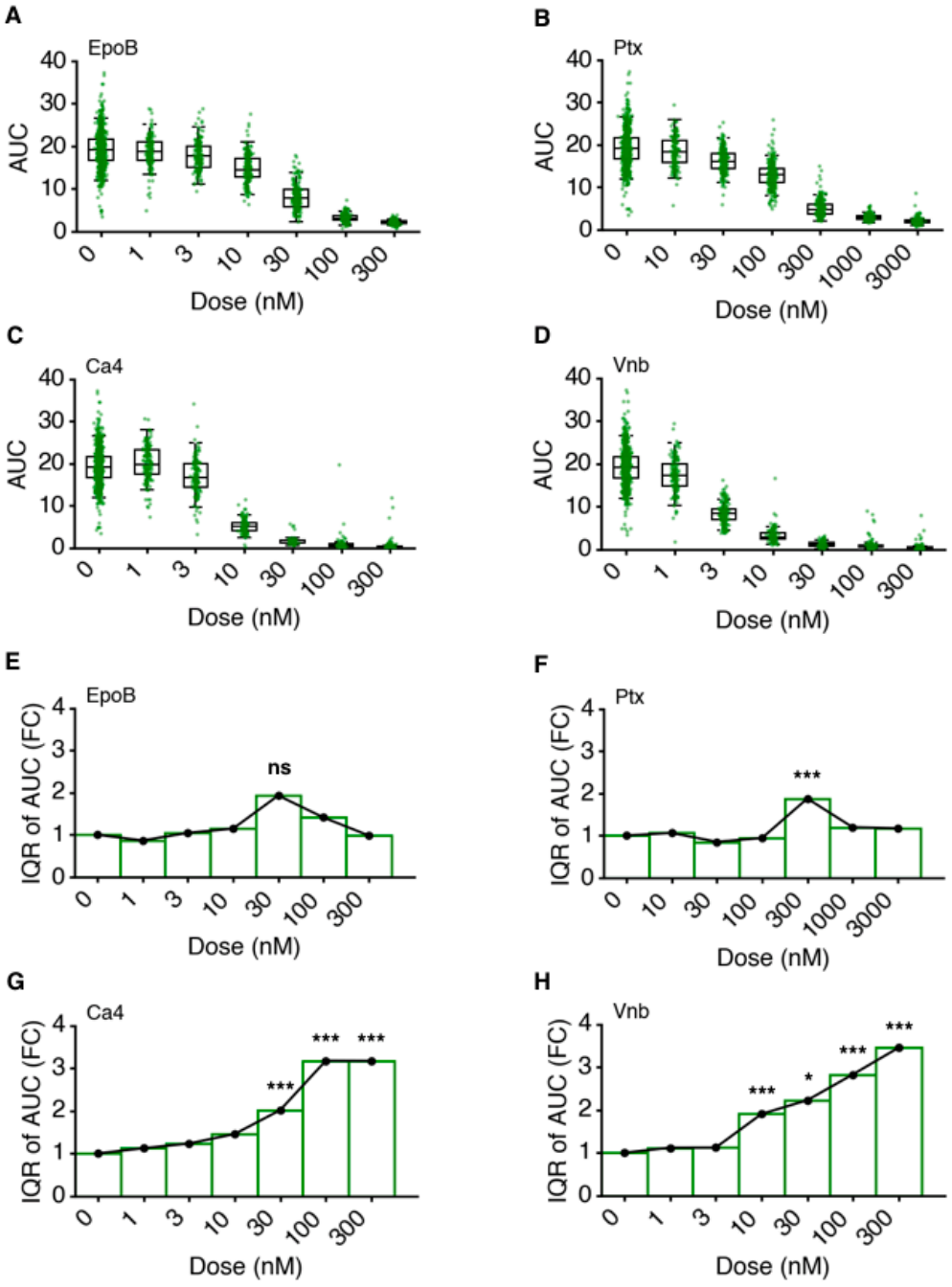

Figure 4.5. *Microtubule poisons stimulate cellular heterogeneity. (A-D) AUCs have been computed for every single-cell curve for EpoB, Ptx, Ca4, and Vnb, respectively. N = 95 cells for 30 nM Ca4. N > 100 cells for all other conditions shown. (E-H) The normalized interquartile ranges of the AUCs in A-D are shown. The IQR of each dose in A-D was normalized by the respective median and subsequently normalized by DMSO control to obtain fold-change. Statistical significance was determined by computing Brown-Forsythe Tests on the sample distributions in A-D. Asterisks denote *p < 0.05 or ***p < 0.001.*

4.5 Discussion

We have demonstrated a novel method for imaging and quantifying EB3 comets in live cells. We implemented the use of EB3 comet counting, which is a simplified, and arguably more interpretable, version of EB3 comet tracking as it directly reports on the number of growing microtubules as opposed to a distribution of comet velocities, which may be less necessary for pharmacological questions. Importantly, the simplicity of our method not only offers a computational advantage to conventional comet tracking, but it also offers a new experimental set-up that is much more amenable to answer questions that demand large-scale experiments. Our experimental method makes use of lower magnification air objective lens, which is compatible with highly multiplexed experiments on 384-well plates. Although this method obtains slightly lower signal-to-noise compared to conventional set-ups on state-of-the-art spinning disk confocal or lattice light sheet microscopes, we were able to develop a background correction algorithm that compensates for the loss in signal-to-noise (Fig. 4.1C).

Our analysis of EB3 comets in response to multiple anti-tubulin drug classes validates EB3 comet counting as a biomarker of microtubule poisons. It also reveals additional insights into dynamic instability. For example, the data shown here suggest that the number of comets over time has basal fluctuations in single cells. Therefore, aside from variability in comet velocities, which is to be expected in any cell type, the number of growing microtubules over time is not necessarily constant in a single cell (Fig. 4.2B, bottom left). It is important to note that our method uses the fold-change of EB3 comet count with respect to a pre-treatment time-point. The advantage of this implementation is that it is less sensitive toward false negatives. Whether 50 comets or 100 comets are counted, at the end of a drugged time-course, the fold-change will be similar. Since all dynamic MTs are affected by anti-tubulin drugs, both quicker-moving and slower-moving comets will be affected. In this way, comet counts give a robust readout of cellular sensitivities with respect to the MT cytoskeleton.

We were able to model both the averaged and single-cell EB3 count data with simple biochemical models. Note that more sophisticated models of dynamic instability have factored in several parameters for single MTs, such as catastrophes, rescues, shrinkage, as well as growth[180], whereas our models only take into account overall MT polymer growth. Nevertheless, our simplified model fits the data well, presumably

because our counting metric measures the average MT response within a single cell which makes it less necessary to know the specific kinetic parameters for each single MT. Although our multiplexed imaging approach limited the temporal resolution of image acquisition, which would normally make it difficult to compare single cells across different wells, our modeling compensated for this by allowing us to compute and compare the cellular trends in comet count fold-change. We then used a classic pharmacology parameter to assess single-cell heterogeneity, i.e. area-under-the-curve. This approach, combined with the ample amount of cellular data collected after drug treatment in the presence of verapamil, allowed us to conclude that anti-tubulin drugs, and MT-destabilizing drugs in particular, stimulate an increase in cellular heterogeneity with respect to MT dynamics, and this drug-induced heterogeneity is independent of efflux drug pump action. Future work may use our framework to probe at MT-proximal biology in a high-throughput format, for example, to assess the response of the MT cytoskeleton to many different cellular stresses, perhaps at the single-cell level. For the first time, these kinds of biological questions can now be tackled with the development of our highly multiplexed set-up and single-cell analysis pipeline.

4.6 Methods

4.6.1 Reagents and cell lines

EpoB, Ptx, and Vnb were purchased from MedChemExpress, whereas Ca4 and verapamil hydrochloride was purchased from Sigma Aldrich. RPE1 cells expressing EB3-GFP were a generous gift from David Pellman at Harvard Medical School.

4.6.2 Cell culture

RPE1 cells expressing EB3-GFP were maintained in DMEM/F12 (Life Technologies) and supplemented with 10% FBS (GIBCO) (v/v) and 1% penicillin-streptomycin (Cellgro).

4.6.3 Image acquisition

We imaged cells using the InCELL Analyzer 6000 high content microscope (GE Healthcare Life Sciences), equipped with 40x/0.95 NA Plan Apochromat objective, heated stage and heated lid, as well as

constant CO_2 flow. For EB3-GFP imaging, the confocality setting was used and the optimal focal plane was determined using the auto-offset function in the InCELL software. For imaging nuclei in the SiR-DNA far red channel, the wide-field setting was used and the focal plane was set to be the same as the EB3-GFP channel. 100 percent laser power was used for both channels, but 200 millisecond and 60 millisecond exposure was used for the EB3-GFP and SiR-DNA channel, respectively. Two fields were imaged per well. To maintain consistency and preserve all image information, binning was not used.

4.6.4 Live-cell microscopy

Each day prior to imaging, RPE1 cells were passaged to 25 percent confluency to discourage contact-dependent inhibition of the cell cycle. The following day, the cells (now at 50 percent confluency) were trypsinized and seeded at 4000 cells per well in 20 μL serum-free media on a 384-well optical bottom Cell Carrier plates (Perkin Elmer) coated with Cell-Tak (Corning). After 30 minutes, 20 μL media with 20% FBS and containing 200nM SiR-DNA (and 20μM verapamil for select plates) was added to each well. Cells were then allowed to incubate for 4-5 hours before imaging.

A separate 96-well plate was filled 150μL per well with media containing 10% FBS (and 10μM verapamil for select plates). Drugs were dispensed onto this 96-well plate using the D300 Digital Dispenser (Hewlett-Packard). Rows B and C were used to dispense the two highest doses of each drug or DMSO control whereas rows D-G were used to dispense the lower doses of each drug or DMSO control. All inner wells were used to dispense drugs at 2x concentration. All border wells were used to dispense saturating Ca4 at 5x concentration (i.e. 20μM to be later diluted to 4μM for the positive control time-point of each time-course). DMSO was kept at 0.03% for all wells.

For high-dose wells on the 384-well plate (i.e. rows B-D or E-G), 15 wells were imaged simultaneously during each time-course. To achieve this, 3 adjacent rows were used whereas 5 non-adjacent columns were used (i.e. every other column). This set up not only allowed us to use an electronic multichannel pipette for drug dispensing, but it also substantially reduced the amount of time between drug addition and the first image acquisition (i.e. ~24-26 seconds) and allowed for a 60-second time interval between each time-point. One image was acquired for every field prior to adding drug. After this pre-

treatment image acquisition, the 384-well imaging plate was ejected from the microscope. The lid heater was moved aside and 40μL of 2x drug was quickly transferred (i.e. using the multistep dispense function on the multichannel pipette) from the 96-well plate to the corresponding wells in the 384-well plate, after which the lid heater was returned, and the plate was immediately reloaded into the microscope to avoid temperature fluctuations. The time-course was then restarted immediately. After completion of the time-course, 20μL of saturating Ca4 was transferred from the 96-well plate onto the same wells of the 384-well plate. After 2 minutes, these wells were re-imaged once more to obtain the cytosolic EB3-GFP background signal for each cell. Low-dose wells on the 384-well plate (i.e. rows H-J or K-M) were imaged and treated similarly, but 27 wells were imaged simultaneously (i.e. 3 adjacent rows and 9 non-adjacent columns) and a 90-second time interval was used.

4.6.5 Single cell segmentation

Images were first aligned using custom-build code in Python. This was necessary because starting and stopping the InCELL Analyzer 6000 for image acquisitions induces slight but noticeable camera shifts in the acquired fields that could complicate single cell tracking over the time-courses. To perform the alignment, we applied a Gaussian blur with 10-pixel radius on all nuclear images, binarized these images all with the same visually-determined threshold, and then determined the optimal row and column shift to align each consecutive time-point for a given field. These optimal row and column shifts were also applied on all channel images for the given field and time-point. At this time, images were also binned 4x4 – surprisingly, we found this had a positive impact on signal-to-noise later in the automated image analysis pipeline.

After image alignment we applied watershed and voronoi algorithms on the nuclear channel to delineate cells. To do this, we first applied a Gaussian blur with 10-pixel radius on all nuclear images and binarized these images all with the same visually-determined threshold. We then took the intersection of every two, consecutive time-point images in order to incur more consistent watershed segmentation across the time-course for a given field.

We imported the aforementioned intersected nuclear images into ImageJ, performed watershed segmentation and used this segmentation to delineate voronoi boundaries as a proxy for cell boundaries; voronoi delineation was an especially convenient algorithm to use for RPE1 cells as these cells tend to cluster together, which complicates the possibility of true delineation of cell boundaries. Considering the possibility of faulty watershed segmentation of some nuclei, we set a minimum and maximum size threshold for counting nuclei. In the case of faulty segmentations as defined by our size thresholds, we preserved the delineated voronoi boundaries but removed the nuclei so that our later algorithms would know to ignore these faulty regions. To be thorough, we also imported the raw EB3-GFP channel images into ImageJ and thresholded these images such that most all of the cellular interiors were accounted for. We then binarized these images and applied the voronoi algorithm on them to further delineate boundaries between cells. We took the resultant cellular voronoi region images and merged them with the corresponding nuclear voronoi region images.

After completing the watershed and voronoi segmentation, we imported the segmented and raw images into Python to count comets, and measure cell areas and nuclear intensities for each time-point.

4.6.6 Single cell tracking

After segmenting single cells, we sought to track each given cell through the various frames of the time-course. To match a given cell between two time-points, we used Euclidean distances between time-adjacent nuclear centroid coordinates, time-adjacent voronoi centroid coordinates, time-adjacent nuclear major axis lengths, and time-adjacent nuclear minor axis lengths.

To be thorough, however, we also set a hard criterion to define a cell match: two cells in time-adjacent images that were matched as identical by the above criteria also needed to have spatial overlap between their nuclei. To implement this criterion, we used the pixel area of each nucleus and, assuming a near-circular geometry, we computed the nuclear radii of these time-adjacent cells and checked whether the distance between the two nuclei was shorter than the sum of the nuclear radii. If this was the case, the two time-adjacent cells were considered to be the same cell. If, however, a cell never achieved a match with any other cells in adjacent time-points, this cell was discarded from all subsequent analysis.

4.6.7 Cell thresholding

In order to reliably count most all cellular EB3-GFP pixels (i.e. in order to obtain cell area measurements), we implemented a Gaussian filter with 2.5-pixel radius each voronoi region containing a single cell. We then implemented a 2-component Gaussian mixture model in order to model both background and cell pixel intensities. The relative minimum between the two Gaussians was set to be the intensity threshold.

4.6.8 EB3 comet thresholding, segmentation, and counting

Comet thresholding was performed separately for every single cell that was faithfully segmented and tracked over time. To do this, a Gaussian blur with 1.25-pixel radius was applied on a given cell voronoi region. This blurred cell region was then subtracted from the original image. The result of this subtraction was then used to threshold with respect to the first time-point, after which this threshold was applied onto all subsequent time-points for the same cell. The threshold was computed in the following way using the first (i.e. untreated negative control) and last (i.e. 4 μM Ca4-treated positive control) time-point: the threshold was chosen that minimized background in the last time-point but also maximized signal in the first time-point. In order to count apparent image puncta as comets, we set a 1-10 pixel size filter.

4.6.9 Modeling averaged single cell data

Equations (4.1), (4.2), and (4.3) were used to model the averaged data acquired for EpoB and Ptx, Ca4, and Vnb, respectively. To do this, the K_d of each drug was set to its literature value (i.e. 1.2, 5, 140, and 2000 nM, respectively). However, the drug diffusion constant, polymerization constant, and maximal possible fold-change increase in MTs were considered unknown and so were subjected to modeling.

4.7 Derivation of EB3 comet models

4.7.1 Modeling variables

N^{comets}: number of EB3 comets (i.e. synonymous with number of growing microtubules). N_{FC}^{comets}: fold-change of comet count. $[D]_{in}$: unbound, intracellular drug concentration. [Tb]: unbound, tubulin concentration. [MT]: unbound, microtubule-incorporated tubulin concentration. [D-Tb]: drug-bound, tubulin concentration. [D-MT]: drug-bound, microtubule-incorporated tubulin concentration. k^{Tb}_{on}: on-rate with respect to tubulin incorporation. k^{Tb}_{off}: off-rate with respect to tubulin incorporation. k^{D}_{on}: drug on-rate. k^{D}_{off}: drug off-rate. k_{diff}: drug diffusion constant. k_{pol}: drug-induced microtubule (de)polymerization constant.

4.7.2 Modeling EB3 comet counts with respect to the colchicine site

We can state the following biochemical relationships:

(S4.1)
$$D_{out} \rightleftharpoons D_{in} + Tb \rightleftharpoons D{-}Tb$$

(S4.2)
$$Tb \rightleftharpoons MT$$

Extracellular drug (D_{out}) defuses into the cell (D_{in}) and binds to unbound colchicine sites on tubulin (Tb). This generates a drug-bound colchicine site (D-Tb). Here, we will assume that in a given cell, "bulk" tubulin and microtubules are at equilibrium inside the cell; we still assert that dynamic instability is present at the single microtubule level. From this assumption, it follows that overall production (or growth rate) of bulk microtubule is constant. In other words:

(S4.3)
$$\frac{d[MT]}{dt} = 0 \Rightarrow \frac{k_{on}^{Tb}}{k_{off}^{Tb}} = \frac{[MT]}{[Tb]} = \frac{[MT]_o}{[Tb]_o}$$

For drug-binding, however, we will assume non-equilibrium. Therefore:

(S4.4)
$$\frac{d[D{-}Tb]}{dt} = k_{on}^{D}[D]_{in}[Tb] - k_{off}^{D}[D{-}Tb]$$

Note that colchicine-site binding drugs bind to soluble tubulin. Also, for the sake of convenience and consistency, we will default to write all equations in terms of total microtubule polymer amount, instead of tubulin. We know that the total amount of soluble tubulin is equal to drug-bound and unbound tubulin. We also know that the total amount of tubulin in the cytoplasm (i.e. the maximum amount of microtubule polymer possible) is equal to the total soluble tubulin plus total polymerized tubulin. Note: here total polymerized tubulin is represented by [MT] or $[MT]_{tot}$, since the only species of microtubule-incorporated tubulin is that which is not bound to a drug. We can therefore define these relationships as follows:

(S4.5) $$[Tb]_{tot} = [Tb] + [D{-}Tb]$$

(S4.6) $$[MT]_{max} = [MT]_{tot} + [Tb]_{tot}$$

Since we are assuming bulk microtubule production is at equilibrium, we can rewrite [Tb} in terms of [MT].

(S4.7) $$[Tb]_{tot} = \frac{k_{off}^{Tb}}{k_{on}^{Tb}}[MT] + [D{-}Tb]$$

We can further write [D-Tb] in terms of $[MT]_{max}$ and $[MT]_{tot}$:

(S4.8) $$[D{-}Tb] = [MT]_{max} - [MT]_{tot} - \frac{k_{off}^{Tb}}{k_{on}^{Tb}}[MT]_{tot}$$

We now refer to [MT] as $[MT]_{tot}$. We will now re-write the rate equation for d[D-Tb]/dt in terms of $[MT]_{tot}$ and $[MT]_{max}$:

(S4.9) $$\frac{d[D{-}Tb]}{dt} = [MT]_{tot}\left(\frac{k_{on}^{D}k_{off}^{Tb}}{k_{on}^{Tb}}[D]_{in} + \frac{k_{on}^{D}k_{off}^{Tb}}{k_{on}^{Tb}} + k_{off}^{D}\right) - k_{off}^{D}[MT]_{max}$$

For modeling the number of EB3 comets per cell, we will make a few assumptions. First, as stated above, the number of comets is synonymous with the number of growing microtubules. On a related note, if the addition of a drug stimulates an increase in the overall microtubule growth rate, the number of comets will increase. Conversely, if the addition of a drug stimulates a decrease in the overall microtubule growth rate, the number of comets will decrease. Additionally, if the amount of drug-tubulin binding becomes constant (i.e. d[D-Tb]/dt = 0), the number of comets will be constant. Similarly, if there is no drug present, the number of comets should be roughly constant. We will also start with the assumption that the number of comets is linearly proportional to the overall growth rate of microtubules, and also linearly proportional to the overall production drug-bound tubulin. From these assumptions, we derive the following equation with respect to the colchicine site:

(S4.10) $$N^{comets} = k_1 \frac{d[D{-}Tb]}{dt} + k_2$$

Where k_1 and k_2 are constants. To determine these constants, we set the known bounds of the system. First, at saturating drug, we know that there will be no EB3 comets and no microtubule polymer present (i.e. $N^{comets} = 0$ and $[MT]_{tot} = 0$). Applying this bound to the N^{comets} equation above and substituting the above representation for d[D-Tb]/dt, we determine that:

(S4.11) $$k_2 = k_1 k_{off}^{D} [MT]_{max}$$

Additionally, when there is no drug present in the cell (i.e. $[D]_{in} = 0$), $N^{comets} = N_o^{comets}$ and $[MT]_{tot} = [MT]_o$. Applying this bound, we find that:

(S4.12) $$N_o^{comets} = k_1 [MT]_o \left(\frac{k_{off}^{D} k_{off}^{Tb}}{k_{on}^{Tb}} + k_{off}^{D} \right)$$

Here we want to point out that fold-change of EB3 comet count is a more reliable metric, considering the fact that in a given field of view, different cells may appear to have different number of comets. If all cells behave the same with respect to a given drug, however, their fold- change in EB3 comet count should be the same at any given time. Taking this into account, we can get the following expression:

(S4.13)
$$\frac{N^{comets}}{N_o^{comets}} = N_{FC}^{comets} = \frac{[MT]_{tot}\left(\frac{k_{on}^{D}k_{off}^{Tb}}{k_{on}^{Tb}}[D]_{in} + \frac{k_{off}^{D}k_{off}^{Tb}}{k_{on}^{Tb}} + k_{off}^{D}\right)}{[MT]_o\left(\frac{k_{off}^{D}k_{off}^{Tb}}{k_{on}^{Tb}} + k_{off}^{D}\right)}$$

After dividing both numerator and denominator by k^D_{off} and recognizing that $[MT]_{tot}/[MT]_o = [MT]_{FC}$, we can rewrite the above expression as:

(S4.14)
$$N_{FC}^{comets} = \frac{[MT]_{FC}\left(\frac{k_{off}^{Tb}[D]_{in}}{k_{on}^{Tb}K_d^D} + \frac{k_{off}^{Tb}}{k_{on}^{Tb}} + 1\right)}{\left(\frac{k_{off}^{Tb}}{k_{on}^{Tb}} + 1\right)}$$

Note that the drug dissociation constant, $K^D_d = k^D_{off}/k^D_{on}$. As mentioned above, because we are assuming bulk microtubule production is at equilibrium,

(S4.15)
$$\frac{k_{off}^{Tb}}{k_{on}^{Tb}} = \frac{[Tb]_o}{[MT]_o} = \frac{[MT]_{max} - [MT]_o}{[MT]_o} = [MT]_{FC,\,max} - 1$$

Where $[MT]_{FC,\,max}$ is the maximal possible fold-change increase in microtubule polymer. For example, if there are equal amounts of soluble and polymerized tubulin, $[MT]_{FC,\,max}$ would equal 2. We have decided to model microtubule depolymerization with a decaying exponential relaxation. We achieve this with the following expression:

(S4.16)
$$[MT]_{tot} = [MT]_o e^{-k_{pol}[D]_{in}} \Rightarrow [MT]_{FC} = e^{-k_{pol}[D]_{in}}$$

Assuming passive drug diffusion, we can model drug diffusion across the plasma membrane as:

(S4.17)
$$\frac{d[D]_{in}}{dt} = k_{in}^{D}[D]_{out} - k_{out}^{D}[D]_{in}$$

Or,

(S4.18) $$[D]_{in} = [D]_{out}\left(1 - e^{-k_{diff}\,t}\right)$$

Where $[D]_{out}$ is assumed to be constant. Taking all of these relationships into account, we can arrive at our final equation for EB3 comet fold-change with respect to the colchicine site:

(S4.19) $$N_{FC}^{comets} = e^{-k_{pol}[D]_{in}}\left(\frac{[D]_{in}}{K_d^D} - \frac{[D]_{in}}{K_d^D[MT]_{FC,\,max}} + 1\right)$$

Note that K^D_d can be obtained from the literature for a given drug. However, the diffusion constant, k_{diff}, the (de)polymerization constant, k_{pol}, and the maximal possible microtubule fold-change increase, $[MT]_{FC,\,max}$, are unknowns that need to be determined by modeling.

4.7.3 Modeling EB3 comet counts with respect to the vinca site

Similarly, as with the colchicine site (though different since vinca-site binding drugs tend to bind to the plus ends of microtubules), we can state the following biochemical relationships:

(S4.20) $$D_{out} \rightleftharpoons D_{in} + MT \rightleftharpoons D\text{–}MT$$

(S4.21) $$Tb \rightleftharpoons MT$$

Just as before, we will assume that "bulk" tubulin and microtubules are at equilibrium inside the cell, so:

(S4.22) $$\frac{d[MT]}{dt} = 0 \Rightarrow \frac{k_{on}^{Tb}}{k_{off}^{Tb}} = \frac{[MT]}{[Tb]} = \frac{[MT]_o}{[Tb]_o}$$

For drug-binding, we will once again assume non-equilibrium. Therefore:

(S4.23) $$\frac{d[D\text{–}MT]}{dt} = k_{on}^{D}[D]_{in}[MT] - k_{off}^{D}[D\text{–}MT]$$

Similarly, as with the colchicine site, we will default to write all equations in terms of total microtubule polymer amount, instead of tubulin. We know that the total amount of polymerized tubulin is equal to drug-bound and unbound microtubule-incorporated tubulin. We also know that the total amount of tubulin in the cytoplasm (i.e. the maximum amount of microtubule polymer possible) is equal to the total soluble tubulin plus total polymerized tubulin. We can therefore define these relationships as follows:

(S4.24) $$[MT]_{tot} = [MT] + [D{-}MT]$$

(S4.25) $$[MT]_{max} = [MT]_{tot} + [Tb] = [MT] + [D{-}MT] + [Tb]$$

Recalling the equilibrium relationship between [MT] and [Tb] and that [Tb] = $[MT]_{max} - [MT]_{tot}$, we can write:

(S4.26) $$[MT] = \frac{k_{on}^{Tb}}{k_{off}^{Tb}}[MT]_{max} - \frac{k_{on}^{Tb}}{k_{off}^{Tb}}[MT]_{tot}$$

Additionally, [D-MT] = $[MT]_{tot} - [MT]$ or:

(S4.27) $$[D{-}MT] = [MT]_{tot} - \frac{k_{on}^{Tb}}{k_{off}^{Tb}}[MT]_{max} + \frac{k_{on}^{Tb}}{k_{off}^{Tb}}[MT]_{tot}$$

We will now rewrite the rate equation for d[D-MT]/dt in terms of $[MT]_{tot}$ and $[MT]_{max}$:

(S4.28) $$\frac{d[D{-}MT]}{dt} = k_{on}^{D}[D]_{in}\frac{k_{on}^{Tb}}{k_{off}^{Tb}}[MT]_{max} - k_{on}^{D}[D]_{in}\frac{k_{on}^{Tb}}{k_{off}^{Tb}}[MT]_{tot} - k_{off}^{D}[MT]_{tot} + k_{off}^{D}\frac{k_{on}^{Tb}}{k_{off}^{Tb}}[MT]_{max} - k_{off}^{D}\frac{k_{on}^{Tb}}{k_{off}^{Tb}}[MT]_{tot}$$

As with the colchicine site, we will make a few additional assumptions for modeling the number of EB3 comets per cell. First, as stated above, the number of comets is synonymous with the number of growing microtubules. On a related note, if the addition of a drug stimulates an increase in the overall microtubule growth rate, the number of comets will increase. Conversely, if the addition of a drug stimulates a decrease

in the overall microtubule growth rate, the number of comets will decrease. Additionally, if the amount of drug- microtubule binding becomes constant (i.e. d[D-MT]/dt = 0), the number of comets will be constant. Similarly, if there is no drug present, the number of comets should be roughly constant. We will also start with the assumption that the number of comets is linearly proportional to the overall growth rate of microtubules. From these assumptions, we derive the following equation with respect to the vinca site:

(S4.29) $$N^{comets} = k_1 \frac{d[D{-}MT]}{dt} + k_2$$

We pause here to note that the entire vinca site model derivation up to this point can also be used to model the taxane site. It changes, however, when we apply bounds to the system to determine k_1 and k_2. First, at saturating drug, we know that there will be no EB3 comets and no microtubule polymer present (i.e. $N^{comets} = 0$ and $[MT]_{tot} = 0$). Applying this bound to the N^{comets} equation above and substituting the above representation for d[D-MT]/dt, we determine that:

(S4.30) $$k_2 = -k_1 k_{on}^{D} [D]_{in} \frac{k_{on}^{Tb}}{k_{off}^{Tb}} [MT]_{max} - k_1 k_{off}^{D} \frac{k_{on}^{Tb}}{k_{off}^{Tb}} [MT]_{max}$$

Therefore, we can rewrite N^{comets} as:

(S4.31) $$N^{comets} = -k_1 [MT]_{tot} \left(\frac{k_{on}^{D} k_{on}^{Tb}}{k_{off}^{Tb}} [D]_{in} + \frac{k_{off}^{D} k_{on}^{Tb}}{k_{off}^{Tb}} + k_{off}^{D} \right)$$

Additionally, when there is no drug present in the cell (i.e. $[D]_{in} = 0$), $N^{comets} = N_o^{comets}$ and $[MT]_{tot} = [MT]_o$. Applying this bound, we find that:

(S4.32) $$N_o^{comets} = -k_1 [MT]_o \left(\frac{k_{off}^{D} k_{on}^{Tb}}{k_{off}^{Tb}} + k_{off}^{D} \right)$$

We can now write things in terms of fold-change, and divide both N^{comets} and N_o^{comets} by $-k_1 k^D_{off}$:

(S4.33)
$$\frac{N^{comets}}{N_o^{comets}} = N_{FC}^{comets} = \left(\frac{1}{\frac{k_{on}^{Tb}}{k_{off}^{Tb}} + 1} \right) \frac{[MT]_{tot}}{[MT]_o} \left(\frac{k_{on}^{Tb}[D]_{in}}{k_{off}^{Tb} K_d^D} + \frac{k_{on}^{Tb}}{k_{off}^{Tb}} + 1 \right)$$

Recall that $k^{Tb}_{off}/k^{Tb}_{on} = [MT]_{FC,\,max} - 1$, where $[MT]_{FC,\,max}$ is the maximal possible fold-change increase in microtubule polymer. Also, as with the colchicine site, we model microtubule depolymerization here with a decaying exponential relaxation, i.e. $[MT]_{FC} = \exp(k_{pol}\,[D]_{in})$. Putting all of this together, we can arrive at our final equation for EB3 comet fold-change with respect to the vinca site:

(S4.34)
$$N_{FC}^{comets} = e^{-k_{pol}[D]_{in}} \left(\frac{[D]_{in}}{K_d^D [MT]_{FC,\,max}} + 1 \right)$$

4.7.4 Modeling EB3 comet counts with respect to the taxane site

For the taxane site, we use the derivations for the vinca site up to before the application of the system bounds. At saturating drug, we know that there will be no EB3 comets and all tubulin will be incorporated into microtubules (i.e. $N^{comets} = 0$ and $[MT]_{tot} = [MT]_{max}$). Applying this bound to the unbound vinca site N^{comets} equation above and substituting the unbound representation for d[D-MT]/dt in the vinca site derivation, we determine that:

(S4.35)
$$k_2 = k_1 k_{off}^D [MT]_{max}$$

Therefore, we can rewrite N^{comets} as:

(S4.36)
$$N^{comets} = k_1 \left(\frac{k_{on}^D k_{on}^{Tb}}{k_{off}^{Tb}} [D]_{in}[MT]_{max} - \frac{k_{on}^D k_{on}^{Tb}}{k_{off}^{Tb}} [D]_{in}[MT]_{tot} + \frac{k_{off}^D k_{on}^{Tb}}{k_{off}^{Tb}} [MT]_{max} - \frac{k_{off}^D k_{on}^{Tb}}{k_{off}^{Tb}} [MT]_{tot} + k_{off}^D [MT]_{max} - k_{off}^D [MT]_{tot} \right)$$

Additionally, when there is no drug present in the cell (i.e. $[D]_{in} = 0$), $N^{comets} = N_o^{comets}$ and $[MT]_{tot} = [MT]_o$. Applying this bound, we find that:

(S4.37) $$N_o^{comets} = k_1 \left(k_{off}^D [MT]_{max} - k_{off}^D [MT]_o + \frac{k_{off}^D k_{on}^{Tb}}{k_{off}^{Tb}} [MT]_{max} - \frac{k_{off}^D k_{on}^{Tb}}{k_{off}^{Tb}} [MT]_o \right)$$

By factoring the N^{comets} and N_o^{comets} equations, and dividing both by $k_1 k^D_{off}$, we can arrive at the following expression:

(S4.38) $$\frac{N^{comets}}{N_o^{comets}} = N_{FC}^{comets} = \frac{([MT]_{max} - [MT]_{tot}) \left(\frac{k_{on}^{Tb}[D]_{in}}{k_{off}^{Tb} K_d^D} + \frac{k_{on}^{Tb}}{k_{off}^{Tb}} + 1 \right)}{([MT]_{max} - [MT]_o) \left(\frac{k_{on}^{Tb}}{k_{off}^{Tb}} + 1 \right)}$$

Recall that $k^{Tb}_{off}/k^{Tb}_{on} = [MT]_{FC,\,max} - 1$, where $[MT]_{FC,\,max}$ is the maximal possible fold-change increase in microtubule polymer. Also, we will model microtubule polymerization here with an exponential relaxation with respect to time:

(S4.39) $$[MT]_{tot} = ([MT]_o - [MT]_{max})\, e^{-k_{pol} t} + [MT]_{max} \Rightarrow [MT]_{FC} = \left(1 - [MT]_{FC,\,max}\right) e^{-k_{pol} t} + [MT]_{FC,\,max}$$

Putting all of this together, we can arrive at our final equation for EB3 comet fold-change with respect to the taxane site:

(S4.40) $$N_{FC}^{comets} = e^{-k_{pol} t} \left(\frac{[D]_{in}}{K_d^D [MT]_{FC,\,max}} + 1 \right)$$

4.8 Derivation of algorithm for EB3 comet background subtraction

To image fluorescent EB3 comets in cells, we use a 40x/0.95 NA air objective lens on an automated high-content microscope (InCELL Analyzer 6000 from GE Healthcare). Traditionally, EB3 comets are imaged using oil-immersion lens at higher magnification (e.g. 60x) to afford greater separation between comet signal and background. In the case of EB3 comets, background is mainly fluorescent cytosolic EB3 marker. This kind of set-up, however, makes higher throughput imaging impractical.

In the case of both oil immersion objective lenses and air lenses, we assume that before any treatment of drug, signal-to-noise is high enough such that we can avoid picking up background in untreated cells. After adding a microtubule drug, comets then come off of microtubules and go into the cytosol, thereby increasing the overall intensity of background (i.e. the background distribution shifts to the right while the comet signal distribution shifts to the left and diminishes in magnitude). In the case of an air lens, however, background and true signal start to overlap after drug treatment (e.g. saturating drug treatment) which makes it difficult to avoid counting background as true signal. For example, when treating cells with saturating microtubule drug, although all comets are quickly eliminated in this case, due to the use of an air lens, cytosolic EB3 will be counted as "comets" and thus the value for comets will be erroneously quantified as being non-zero. If we, however, know the relationship between the comet distribution shift and the background distribution shift, we would be able to back calculate the background and then subtract it out.

After adding a microtubule drug EB3 comets start disappearing over time, and the cytosolic EB3 (i.e background) increases at the same time. Both the raw quantified comet signal and cytosolic background have an exponential relationship with respect to time. We wish to point out the obvious here: every time we lose an EB3 protein from microtubule plus-ends, we gain another EB3 protein in the cytosol. In other words, the loss of comets is linearly proportional to the concentration of EB3 in the cytosol, as is the background. If we can determine where the background and raw signal intersect on the $[EB3]_{cytosol}$ axis, we will be able to back-calculate the amount of EB3 background at any given raw quantified comet value, y_o^{raw}.

Let us suppose that we pick a threshold that allows us to avoid background before drug treatment (i.e. $y_o^{bkg} = 0$, where *y* represents measured signal), but after we have eliminated all EB3 comets, our final

– and maximum – background becomes y_f^{bkg}. Note that since we have eliminated all comets, the raw comet signal will be equal to the final background by definition, i.e. $y_f^{raw} = y_f^{bkg}$.

Let us then define a decreasing linear raw signal curve as $y^{raw} = -ax + y_o^{raw}$ and also define an increasing linear background curve as $y^{bkg} = bx$, where *x* represents additional cytosolic EB3 and $-a$ and *b* are the respective slopes of the two curves. If we solve each equation for *x* and set them equal to each other, we obtain the following relationships:

(S4.41) $$\frac{y^{bkg}}{b} = \frac{y_o^{raw} - y^{raw}}{a} \quad \Rightarrow \quad y^{bkg} = \frac{b}{a}(y_o^{raw} - y^{raw})$$

We can obtain true comet signal by subtracting the corresponding cytosolic background from the raw comet signal. In other words:

(S4.42) $$y^{true} = y^{raw} - y^{bkg} \quad \Rightarrow \quad y^{true} = y^{raw} - \frac{b}{a}(y_o^{raw} - y^{raw})$$

Also, at the intersection of the curves:

(S4.43) $$\frac{y_f^{bkg}}{b} = \frac{y_o^{raw} - y_f^{raw}}{a} \quad \Rightarrow \quad y_f^{bkg} = \frac{b}{a}\left(y_o^{raw} - y_f^{raw}\right)$$

But since $y_f^{bkg} = y_f^{raw}$:

(S4.44) $$y_f^{bkg} = \frac{b}{a}\left(y_o^{raw} - y_f^{bkg}\right) \quad \Rightarrow \quad \frac{b}{a} = \frac{y_f^{bkg}}{y_o^{raw} - y_f^{bkg}}$$

Now that we have a relationship for the ratio of the slopes, we can complete the expression for true comet signal y^{true}:

(S4.45) $$y^{true} = y^{raw} + (y^{raw} - y_o^{raw})\left(\frac{y_f^{bkg}}{y_o^{raw} - y_f^{bkg}}\right)$$

The only unknown term that must be determined at this point is the final (i.e. maximum possible) background signal at the given intensity threshold. In order to obtain this value for each single cell, we have decided to add saturating destabilizing drug (i.e. 4μM combretastatin-A4) after all of our time-courses to induce complete comet loss and maximal background. Then we take that value and correct the comet time-course by subtracting the respective background from each raw EB3 comet value. The amount of background subtracted is naturally the least at the beginning of the time-course and greater at the end of the time-course.

4.9 Acknowledgements

This work was supported by NIH grant GM39565. J.J.P. was supported by a Ruth Kirschstein fellowship (GM117882-02) from NIH-GM. We thank the Nikon Imaging Center and the Lab of Systems Pharmacology at HMS for microscopy support. We also thank David Pellman (HMS) for gifting us with RPE1 cells expressing EB3-GFP.

Chapter 5

Discussion

5.1 Main findings and advancements

Every class of MT-targeting drugs inhibits the dynamic instability of MTs. This basic similarity among these compounds, in addition to the observation that these drugs all induce mitotic arrest, has heavily influenced the study of these drugs in the context of mitosis, during which MTs are most dynamic and therefore most sensitive to chemical perturbation. The work contained in this thesis does not disprove the importance of mitosis for the pharmacology of these drugs, but it does present findings that argue for the importance of further study into their interphase effects.

We performed high-content imaging in RPE1 and HT1080 cells and compared the degree of taxane-site occupancy required for MT dynamics loss, mitotic arrest, or induction of post-mitotic micronucleation. We found that MT dynamics was the most sensitive phenotype, which became perturbed at very low site occupancies. We also determined that post-mitotic micronucleation occurred over a broad range of taxane-site occupancies for all drugs and cell lines tested and we confirmed that this phenotype could occur independent of mitotic arrest at lower concentrations of drug. Our work in cells and in an HT1080 xenograft model supports – but does not prove – the idea that chromosome missegregation and subsequent G1 arrest in a micronucleated state is the most important cellular action of taxanes in cancer chemotherapy.

After observing biological effects many hours after drug treatment in the second chapter of this thesis, we decided to focus on rapid biology induced by these drugs in the third chapter. For this, we utilized MS-based phosphoproteomics and quantified relative phosphopeptide changes over several time-points and multiple drugs. Our analysis revealed the phosphorylation of hundreds of downstream substrates in response to MT stabilization and MT destabilization. For the first time, we were able to make a global comparison between these two main classes of drug: MT stabilizers versus MT destabilizers. Our work confirmed the activation of MAPK pathways in response to MT destabilization but more importantly revealed the induction of phosphatase activity. Our work in this chapter also suggested a striking reality about JNK regulation – that induction of JNK activity in interphase can occur without additional JNK activation – thereby confirming the importance of further study into the interphase effects of anti-tubulin drugs.

Upon discovering the large amount of phospho-signaling that these drugs induce in cells at such quick time-scales, we decided to look into possible heterogeneity among single cells in their response to a panel of MT-targeting drugs. To do this, we developed a novel high-content approach for quantifying MT dynamics in single cells, namely EB3 comet counting. Using this method, we discovered that, over the quick time-course tested, most drugs in our panel induced a substantial degree of heterogeneity with respect to interphase MT dynamics. Furthermore, we observed this result in the presence of a pan-efflux drug pump inhibitor, which suggests that the heterogeneity may originate from something other than efflux pump action.

These results present previously unknown biology concerning these drugs in interphase and highlight the importance of further study.

5.2 Comparing phenotypes, drug efficacy and cellular sensitivity on the site occupancy axis

We used a previously published fluorogenic compound to develop a high-throughput ligand displacement assay[121]. This assay allowed us to compute taxane-site occupancy as a function of drug concentration in live cells, after which we were able to make quantitative comparisons between three phenotypes, four drugs, and two cell lines. This work primarily addressed the question of how much MT disruption is necessary to elicit cellular phenotypes for the taxane drug class, but it simultaneously raised new questions.

Regarding our initial site occupancy measurements (Fig. 2.2C-H), it is interesting to note the surprising agreement between our apparent binding constants and those present in the literature. The high degree of agreement, which affirms the reliability of our method, was unexpected given that we made binding measurements in live cells with respect to extracellular drug concentration. In contrast, previous measurements produced bona fide binding constants *in vitro* using purified and cross-linked MTs[118]. One would imagine that the presence of MAPs in the live-cell case would affect drug binding affinity, but our results suggest that this is not the case. Instead, MAPs do not seem to have a large effect on the binding affinity of taxane-site drugs, which we hypothesize may be due to the presence of the taxane-site on the inner lumen of MTs, which might experience far less steric disruption by MAPs. It would be interesting to

conduct live-cell binding constant measurements for the peloruside site, which resides on the outside of the MT lattice and may directly interact with MAPs.

We used our site occupancy measurements to compare differential drug efficacy with respect to mitotic arrest and micronucleation (Fig. 2.4A-B). In the case of mitotic arrest, it is surprising that paclitaxel is inefficient compared to the epothilone drugs in RPE1 cells and yet be one of the most efficient in HT1080 cells, while the converse is true for epothilone-D. We had already found it interesting that the different taxane-site drugs we tested differed in efficiency with respect to mitotic arrest on the site occupancy axis. This would argue for important differences in drug-induced MT conformations. Given that these drugs are known to bind along the MT lattice, MT conformational changes are likely dependent on site occupancy. The fact that the same drug can possess different relative efficiencies with regard to mitotic arrest in two different cell lines argues for something more than just conformational changes in MTs. One possible explanation is differential MAP composition between the two cell lines. This could either involve a different set of MAPs present between the two cell lines, different proportions of the same MAPs, a different amount of post-translationally modified MAPs, or all of the above. To test these possibilities, one would need to perform a co-sedimentation experiment with respect to MTs and then compare the relative amounts of all binding proteins in the two cell lines, perhaps via MS-based proteomics. The challenge here is that, in order to compare amounts of one protein to another in the same cell line, it is necessary to measure the original cellular protein concentrations, which can be done by summing up the ion current in the MS1 spectrum for all peptides of a given protein and normalizing this sum by the theoretical number of peptides produced by proteolysis[181]. In addition, a phosphoenrichment step would need to be performed of both the MT-enriched pellet as well as the supernatant, especially considering that phosphorylation can affect the binding of MAPs. Given the different efficacies of these drugs in cells, it would be very informative to repeat these assays in a whole panel of cancer- and non-cancer cell lines. Such an analysis would likely reveal that different MT drugs can be more efficacious depending on the cancer.

In terms of the most important cellular action of taxane-site drugs in cancer, our work hints toward chromosome missegregation and subsequent micronucleated G1 arrest. Although Fig. 2.5E may initially appear to argue against this hypothesis, we remind the reader that we used a single-dose regime for our

in vivo experiments. This is analogous to the two-week high dose regimen given to cancer patients who suffer from solid tumors. Considering the pharmacokinetic properties of paclitaxel in the human body, we know that at least half of the drug clears out of the body within 3 days[182], after which it will continue to clear out due to clearance. As clearance occurs over the span of the two-week regimen, the intratumoral concentration of paclitaxel will drop and fall into the broad micronucleation regime depicted in Fig. 2.5E. In support of this argument, one group compared the results of breast cancer patients who were given a high-dose biweekly regimen with those of patients who were given a low-dose weekly regimen, and found that the low-dose regimen was equally effective and less toxic[183].

Other than the biological insights provided by our site occupancy-guided analysis, we highlight the fact that all of the cell culture assays were performed in a high-throughput (i.e. 384-well plate) format and can be easily scaled to evaluate other taxane-site drugs or adapted for use in other cell lines.

5.3 Novel phospho-signaling induced by MT-targeting drugs

Using MS-based phosphoproteomics, we conducted the first global comparison of phospho-regulation induced by MT-stabilizing and destabilizing drugs. This assay reproduced phosphorylation events that had been seen previously (e.g. activation sites of MAPKs) and also revealed an acute response to MT disruption as measured by more than one thousand phosphorylation changes.

Comparing phosphorylation events observed between eribulin and epothilone-B, we were surprised by the enrichment of MAPs among high-fold-changing phosphopeptides (Fig. 3.3B). In the case of eribulin, most of these MAPs were found to be dephosphorylated (e.g. Fig. 3.3C). Given that MAP phosphorylation is known to reduce affinity for MTs and that sites were dephosphorylated in the MT-binding regions of critical MAPs (e.g. S941 and S1073 on MAP4), this finding hints at a compensatory response induced by MT destabilization. In other words, depolymerization of MTs may likely release a sensor protein (e.g. a phosphatase) which induces dephosphorylation of several MAPs in an attempt to re-stabilize MTs. Further study is necessary to address this hypothesis. Future experiments may involve kinetic drug titration experiments that observe drug-induced phospho-changes and correlate these to MT polymer loss and MT dynamics loss. In addition, this hypothesis can be further tested with knockdowns of phosphatase subunits,

perhaps with special focus on those that associate with MTs, and subsequent retesting of drug-induced phospho-regulation in the presence of these knockdowns.

The most prominent cluster in our phosphoproteomics data clearly demonstrated parallel effects of the two drugs on phosphorylation. It is not trivial that a high-dose of two mechanistically different MT-targeting drugs can produce a such large amount of common signaling (Fig. 3.3F, middle cluster), especially considering that one drug will fully polymerize MTs while the other eventually depolymerizes MTs at the dose tested (i.e. 800 nM). Results from our experiment combining epothilone-B and kinase inhibitors strongly suggested that JNK was most responsible for this common signaling (Fig. 3.4A-C), especially considering the rapid onset of this common signaling and that ERK and p38 were activated at later time-points (Fig. 3.3E). Collectively, our results hint at unresolved pathways of stimulating JNK activity that differ between MT-stabilizing and destabilizing drugs. A small cluster of (likely) JNK-dependent phosphopeptides were phosphorylated in the case of epothilone-B but were found to either be dephosphorylated or remain relatively unchanged in the case of eribulin. This may suggest competition between JNK and the phosphatase implicated above. Inhibition of a phosphatase could explain the net increase of JNK activity. We present a potential model of this in Fig. 3.5, but we disclaim that there may be other potential models of phosphatase or JNK regulation that explain the data.

Although we highlight the prevalence of proline-directed phosphorylation in the case of the two drugs tested, we want to highlight the fact that not all changing phosphopeptides contained proline-directed motifs (Fig. 3.3D). These motifs were only found in ~40 percent of the changing phosphosites for epothilone-B. This suggests that other kinases are recruited in the JNK-dependent signaling stimulated by MT stabilization. These candidate kinases could be identified by conducting more combinatorial drug treatments with additional kinase inhibitors, similar to the one presented in Fig. 3.4. This would involve more phosphoproteomic experiments, but the workload could potentially be lessened if performed in combination with bioinformatic inference into likely kinase-substrate relationships.

We made an additional side observation regarding these data. We detected phosphorylation of several sites that were annotated as CDK1 sites in the literature and as being important for mitosis. This was unexpected given that we grew our RPE1 cells past confluency to induce contact inhibition and

quiescence. For example, eribulin and epothilone-B both induced phosphorylation of lamin-A (LMNA) at either threonine T19 or serine S22 (Supplementary Fig. 3.6), both of which are CDK1 sites. Phosphorylation of serine S22 is known to be necessary for disassembly of the nuclear lamin prior to mitosis[184]. Our combinatorial drug experiment demonstrated, however, that phosphorylation of these sites and others was JNK-dependent and not CDK-dependent (Supplementary Fig. 3.8).

These data raise the question of how global phospho-signaling may differ between cell types. It may be possible, for example, that different cell types induce similar phospho-regulation in response to these drugs, but the degree of phosphorylation may differ. Considering the possible compensatory response in the context of MT destabilization, less phosphatase activity in a given cell type could cause greater sensitivity to MT-destabilizing drugs.

5.4 Drug-induced heterogeneity in MT dynamics

After having conducted analysis of phospho-signaling in an averaged population of cells, we desired to test effects of MT-targeting drugs on MT dynamics in single cells. An important side note here is how such a question has been previously infeasible to answer. Most work probing into MT dynamics have used conventional comet tracking, which involves imaging fluorescently-labeled +TIPs. These analyses have largely been performed to obtain information regarding comet trajectories and velocities and have reported MT growth rates instead of directly commenting on the number of growing MTs[75,171]. Although this approach procures highly quantitative data, it also inhibits imaging throughput and is unpractical for answering complex biological questions like the nature of heterogeneity in single cell MT dynamics.

We developed the first practical approach for imaging MT dynamics via comet counting, a simplified version of comet tracking that allows for more infrequent image acquisitions and thereby enables scale-up onto 384-well plates. We show-case the ability of this method to bridge the fields of high-throughput/high-content screening and MT biology by conducting relatively short time-courses in chapter 4. It is important to note, however, that our pipeline can also be conducted on longer time-scales with less frequent image acquisition which would allow for even more experimental scale-up and user convenience. With this being said, it should be noted that questions involving single-cell analysis set a lower limit on the frequency of

image acquisition; this is because it is hard to confidently identify the same cell between two snapshots if too much time has passed.

To probe into single-cell heterogeneity in response to MT-targeting drugs, we began by acquiring single-cell data for an ample number of cells (greater than 100-200 on average) for each drug condition tested. The data we obtained indicated that a significant degree of single-cell heterogeneity can be measured without addition of drug (Fig. 4.2, DMSO). This was observable even with stringent comet and background cutoffs, suggesting that the extent of MT dynamicity truly differs from cell to cell. Given our limited frequency of image acquisition, however, we sought to model each single-cell EB3 profile in order to facilitate comparison between conditions (Fig. 4.3-4.4). This allowed us to use a classic pharmacology metric, area-under-the-curve, to assess the heterogeneity of drug response. Using this approach, we discovered an increase in single-cell heterogeneity with respect to MT dynamics stimulated by higher doses of drug, especially in the case of MT destabilizers (Fig. 5E-H). One possible explanation for this heterogeneity is that MTs are differentially regulated by these cells in response to drug treatment. This differential regulation could occur at the level of PTMs, for example phosphorylation. This is a reasonable hypothesis given the phosphoproteomics results in chapter 3. That being said, future experiments should test drug-induced single-cell heterogeneity with respect to MT dynamics in the presence of JNK inhibition given that this kinase is responsible for the phosphorylation of large number of substrates, including MAPs. Given the increase in heterogeneity that we observed in the presence of a pan-efflux pump inhibitor, it is also a question of whether removing this additional inhibitor might allow for a greater increase in heterogeneity due to the activity of drug pumps.

5.5 Conclusion

In 1967, the previously elusive subunit of the microtubule was discovered to be the “colchicine-binding protein”[4]. Over the past half-century, much has been discovered regarding the effects of anti-tubulin drugs, especially with regard to their effects on microtubule dynamics, and consequentially, their effects on mitosis and cell division. Comparably less extensive research has been conducted on interphase effects.

The data in this thesis provides novel insights into the pharmacology of these drugs. For one, it is now apparent that the relative efficacies of anti-tubulin drugs with respect to downstream phenotypes can differ significantly between cell types. Moreover, these drugs can stimulate massive phosphorylation changes on the order of minutes and depending on whether the drug stabilizes or destabilizes microtubules, a phosphatase may be inhibited or activated. Finally, this thesis demonstrates how these drugs stimulate a heterogeneous response in cells with respect to interphase microtubule dynamics.

In the translational sphere of biology, interest in learning more about anti-tubulin drugs appears to be waning, perhaps due to contentment with decades of (partial) success in the clinic, in conjunction with rising interest in immuno-oncology approaches for cancer therapy. My hope is that the work presented in this thesis 1) offers compelling evidence that there are still many unanswered questions concerning the biology of these drugs, 2) offers modern approaches to biological discovery that can be used to answer those questions, and 3) demonstrates how there is much more to be known before we actually understand how these drugs work in the clinic.

Appendix: Supplementary Figures

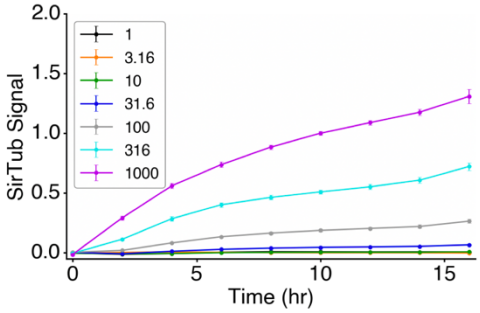

Figure S2.1. *SirTub uptake kinetics in live HT1080 cells. Time-course and titration of SirTub staining in HT1080 cells. Legend represents nanomolar concentrations of SirTub. Intensities have been normalized by cell area at every time point. Each data point has been averaged from 9 replicate wells.*

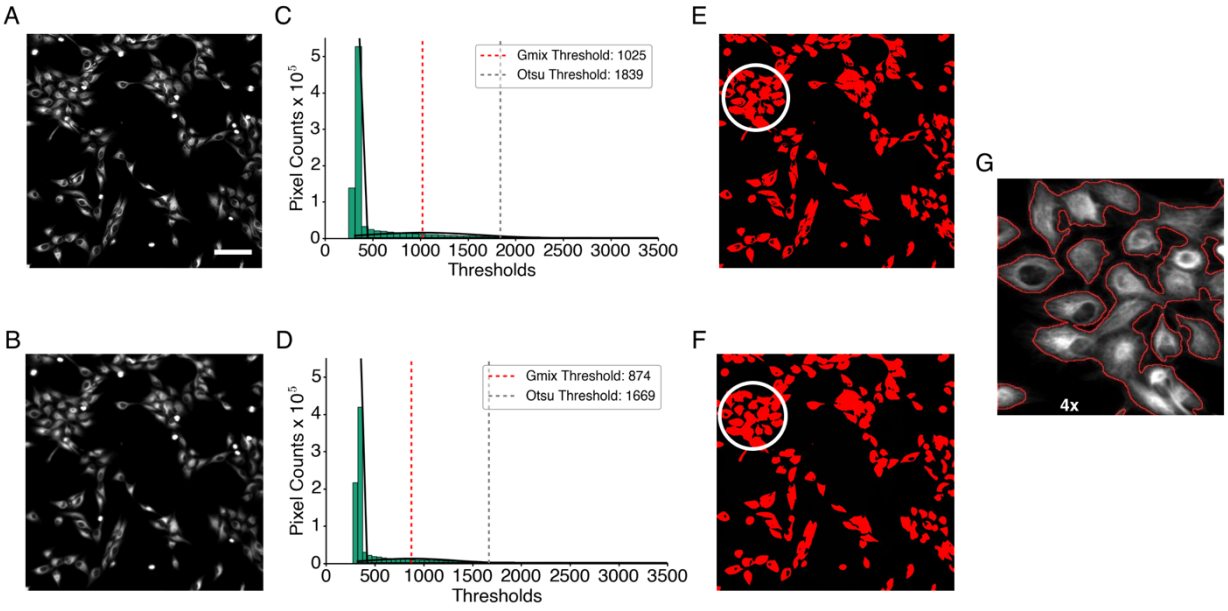

Figure S2.2. *Gaussian mixture models enable proper thresholding of intracellular SirTub. (A) Representative 20x image of RPE1 cells stained with 316nM SirTub. Scale bar = 100 µm. (B) Image in A has been subjected to a Gaussian blur with a 2.5-pixel radius. (C) Image histogram of pixel intensities (and possible thresholds) in A. Gaussian model curves are overlaid in black. Otsu threshold has been included for reference. (D) Image histogram of B. (E) Implementation of "gmix threshold" in C onto image in A. Circled region has been magnified in G. (F) Implementation of "gmix threshold" in D onto image in B. Circled region has been magnified in G. (G) Overlay of area perimeter from F onto image in A.*

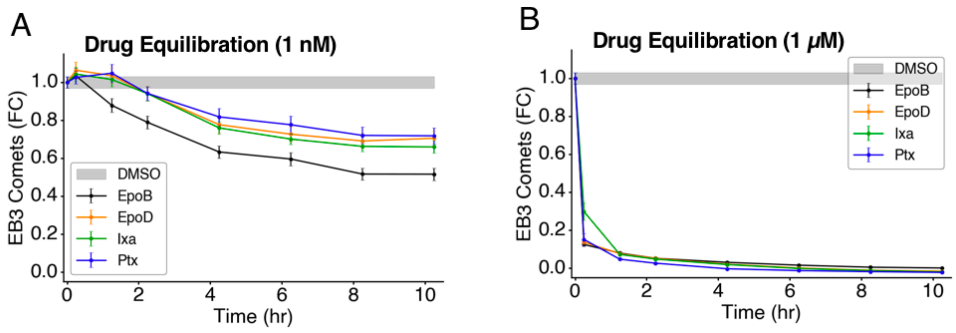

Figure S2.3. *(A) Time-course of EB3 comet loss in RPE1 cells after treatment with 1 nM of microtubule drugs. Cells were imaged before and after drug treatments. Comet values have been normalized to cell area at every time point. (B) Time-course of EB3 comet loss in RPE1 cells after treatment with 1 μM of microtubule drugs. Cells were imaged and quantified as in D. All error bars denote standard error of the mean.*

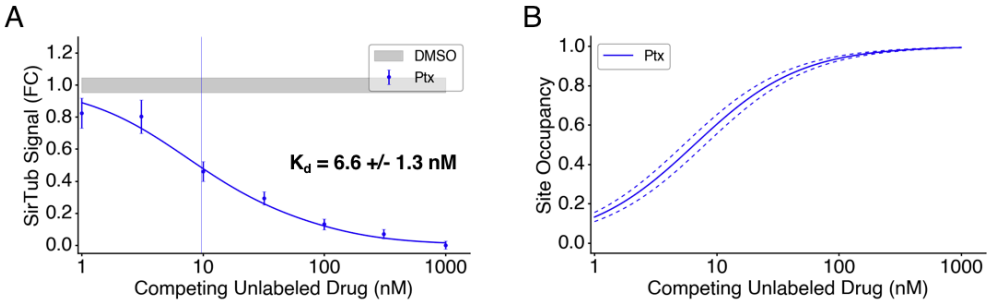

Figure S2.4. *Site Occupancy of Ptx in ReN cells. (A) SirTub displacement assay in ReN cells (in the presence of 316nM SirTub). Each data point has been averaged from at least 9 wells. Data has been regressed using equation (2.1), which accounts for drug-induced microtubule polymerization. IC_{50} is denoted by a solid vertical line. (B) Site occupancy calibration curve for ReN cells. The $K^d_{d,app}$ value in A was inputted into equation (2.2) to compute drug site occupancies corresponding to 1 nM-1 μM. Dotted lines represent standard error as derived from the model fit in A.*

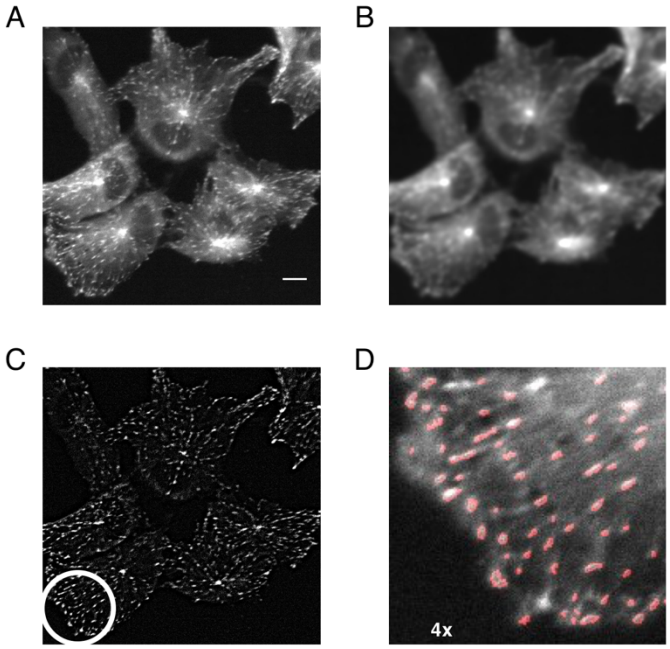

Figure S2.5. *EB3 comet segmentation. (A) Representative 40x image of EB3-GFP comets in live RPE1 cells. Scale bar = 10 µm. (B) Image in A has been subjected to a Gaussian blur with a 5-pixel radius. (C) Image in B has been subtracted from image in A. Circled region has been magnified in D. (D) Comets defined after manual thresholding are outlined in red.*

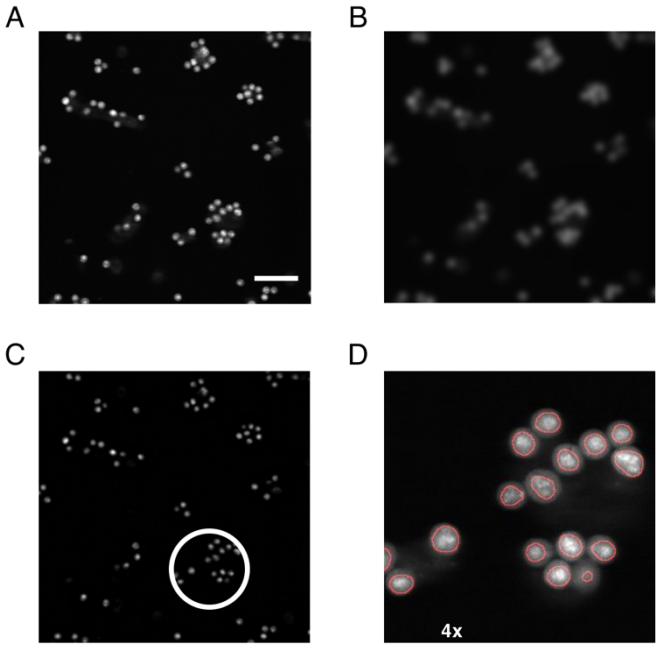

Figure S2.6. *Segmentation of mitotic cells. (A) Representative 20x image of EB3-GFP in mitotic RPE1 cells. Cells have been imaged 10 µm above normal autofocus z-position. Scale bar = 100 µm. (B) Image in A has been subjected to a Gaussian blur with 12.5-pixel radius. (C) Image in B has been subtracted from image in A and the resulting image has been subjected to a Gaussian blur with 2.5-pixel radius. Circled region has been magnified in D. (D) Manual thresholding and watershed segmentation has been implemented on the image in C. Mitotic cells defined after segmentation are outlined in red.*

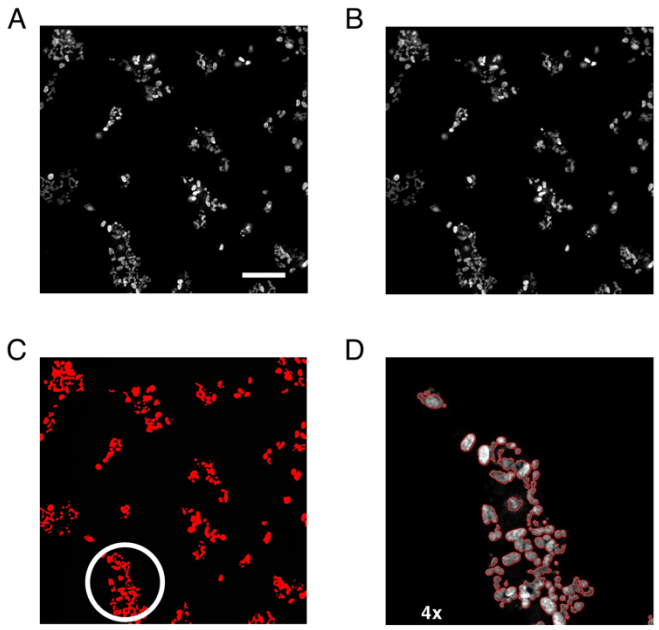

Figure S2.7. *Segmentation of micronuclei. (A) Representative 20x image of micronuclei in RPE1 cells stained with 1µg/ml Hoechst dye. Scale bar = 100 µm. (B) Image in A has been subjected to a Gaussian blur with 1-pixel radius. (C) Otsu thresholding has been implemented on image in B. Circled region is magnified in D. (D) Watershed segmentation has been implemented on the image in C. Micronuclei defined after segmentation are outlined in red.*

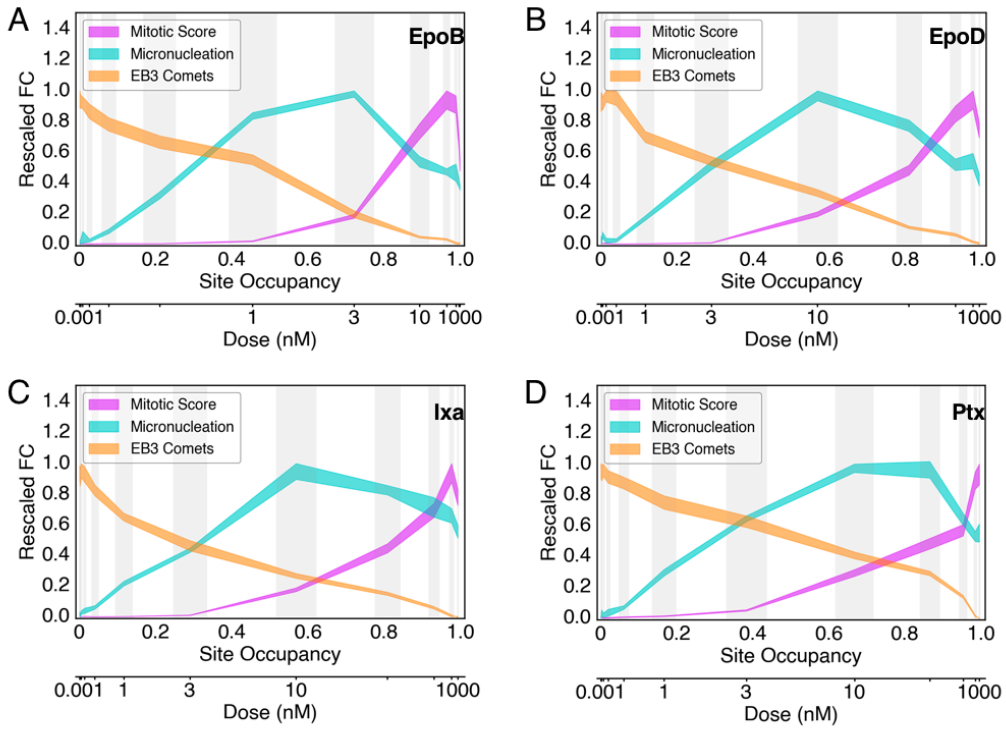

Figure S2.8. *Phenotypic comparisons on the site occupancy axis (RPE1 cells). (A) Phenotypic comparison of microtubule dynamics (represented by EB3 comet numbers), micronucleation, and mitotic arrest in RPE1 cells after 22 hours of treatment with EpoB, (B) EpoD, (C) Ixa, (D) and Ptx. Vertical gray bars denote standard error of site occupancy. Each data point shown in A-D has been averaged from 9 replicate wells, and then scaled by each respective phenotypic maximum.*

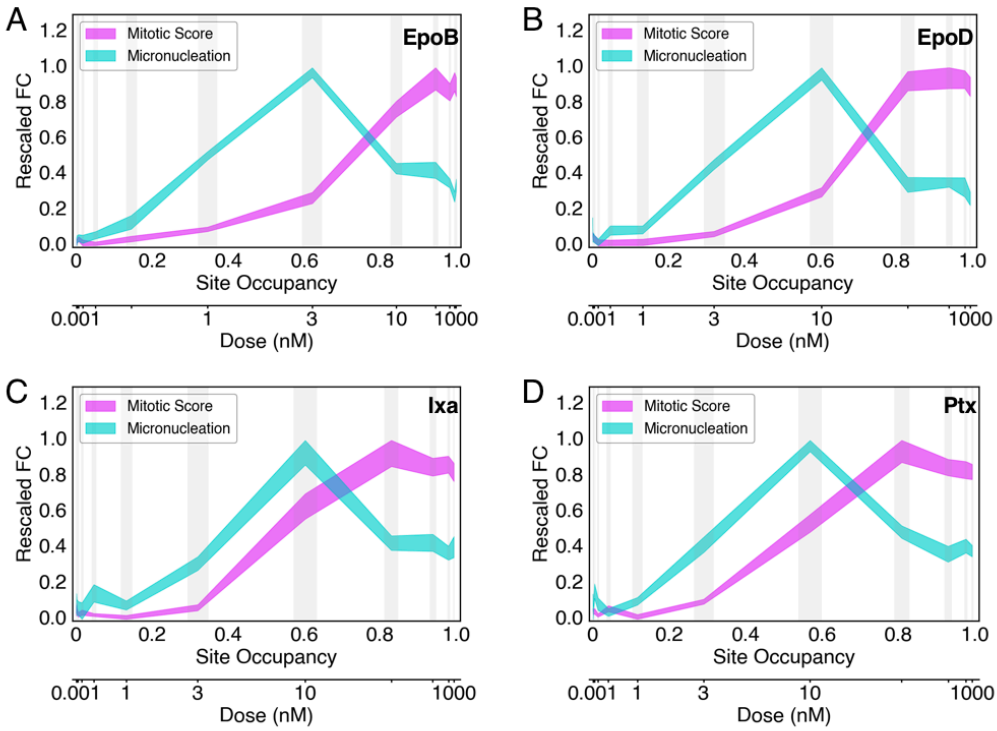

Figure S2.9. *Phenotypic comparisons on the site occupancy axis (HT1080 cells). (A) Phenotypic comparison of micronucleation and mitotic arrest in HT1080 cells after 24 hours of treatment with EpoB, (B) EpoD, (C) Ixa, (D) and Ptx. Vertical gray bars denote standard error of site occupancy. Each data point shown in A-D has been averaged from 9 replicate wells, and then scaled by each respective phenotypic maximum.*

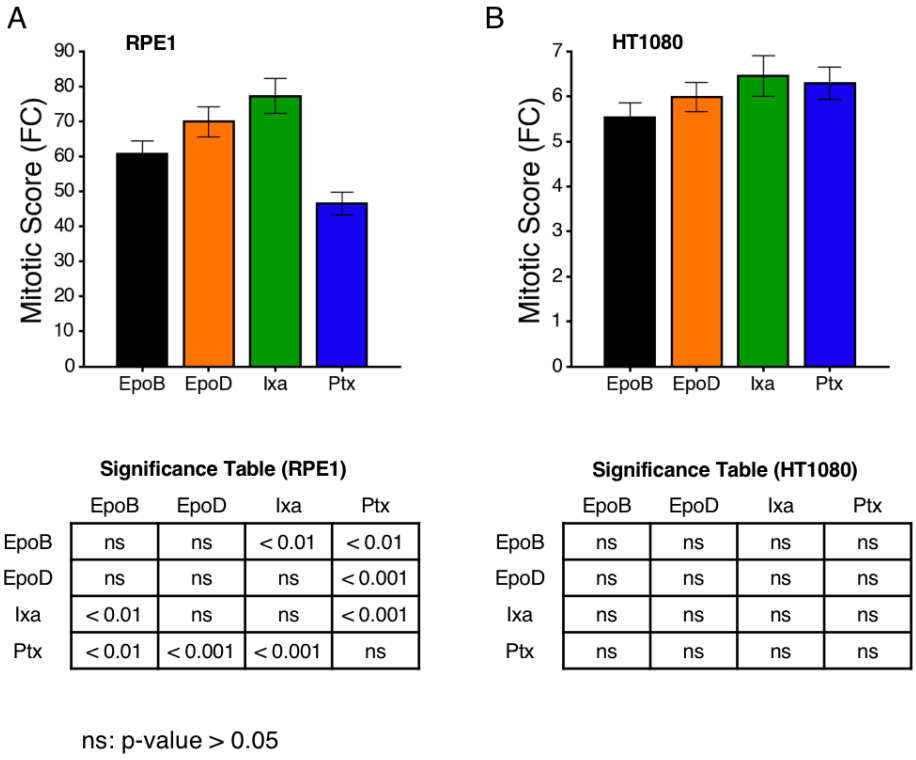

Significance Table (RPE1)

	EpoB	EpoD	Ixa	Ptx
EpoB	ns	ns	< 0.01	< 0.01
EpoD	ns	ns	ns	< 0.001
Ixa	< 0.01	ns	ns	< 0.001
Ptx	< 0.01	< 0.001	< 0.001	ns

Significance Table (HT1080)

	EpoB	EpoD	Ixa	Ptx
EpoB	ns	ns	ns	ns
EpoD	ns	ns	ns	ns
Ixa	ns	ns	ns	ns
Ptx	ns	ns	ns	ns

ns: p-value > 0.05

Figure S2.10. *Drug-induced mitotic maxima. (A) Drug-drug comparisons with respect to mitotic scoring in RPE1 (B) and HT1080 cells. For each cell line, the values have been normalized to the DMSO control value, which we denote here as fold-change (FC). Tables with p-values are shown below each plot to facilitate assessment of drug-drug differences.*

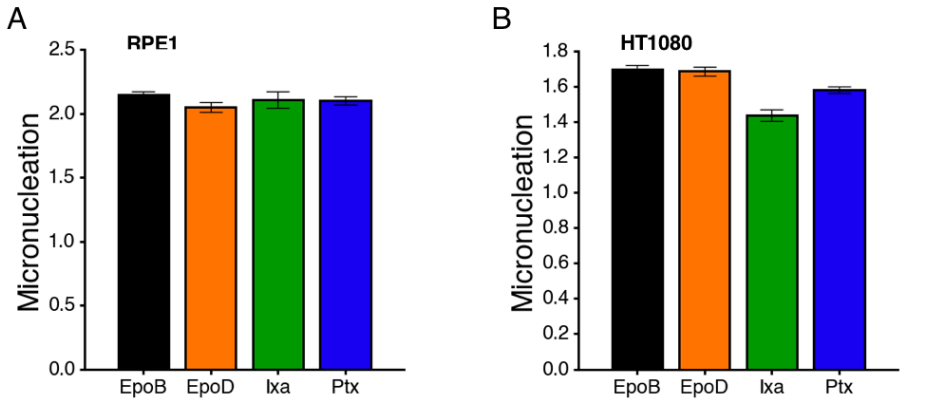

Significance Table (RPE1)

	EpoB	EpoD	Ixa	Ptx
EpoB	ns	< 0.05	ns	ns
EpoD	< 0.05	ns	ns	ns
Ixa	ns	ns	ns	ns
Ptx	ns	ns	ns	ns

Significance Table (HT1080)

	EpoB	EpoD	Ixa	Ptx
EpoB	ns	ns	< 0.001	< 0.001
EpoD	ns	ns	< 0.001	< 0.01
Ixa	< 0.001	< 0.001	ns	< 0.001
Ptx	< 0.001	< 0.01	< 0.001	ns

ns: p-value > 0.05

Figure S2.11. *Drug-induced micronucleation maxima. (A) Drug-drug comparisons with respect to micronucleation in RPE1 (B) and HT1080 cells. For each cell line, the values have been normalized to the DMSO control value, which we denote here as fold-change (FC). Tables with p-values are shown below each plot to facilitate assessment of drug-drug differences.*

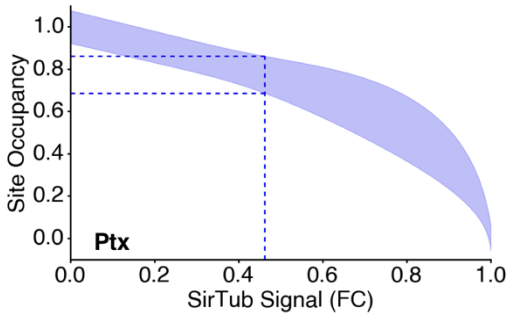

Figure S2.12. *Simulated drug site occupancy for HT1080s. Values and uncertainties from the ligand displacement assay (Fig. 2.2E, F) were used to obtain the relationship between SirTub signal fold-change and Ptx site occupancy. Shaded region denotes possible site occupancies given a known value for SirTub signal fold-change. Vertical dotted line denotes median SirTub signal fold-change in vivo after 24-hr treatment with 30 mg/kg Ptx. Horizontal lines denote the standard error spread of the in vivo site occupancy after this same dose.*

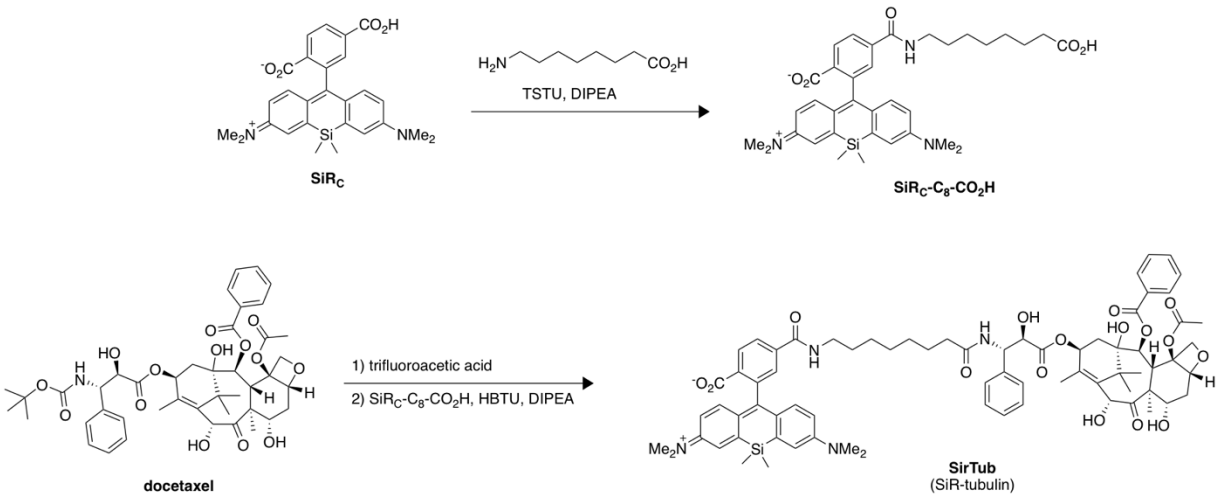

Figure S2.13. *Chemical synthesis of SirTub*

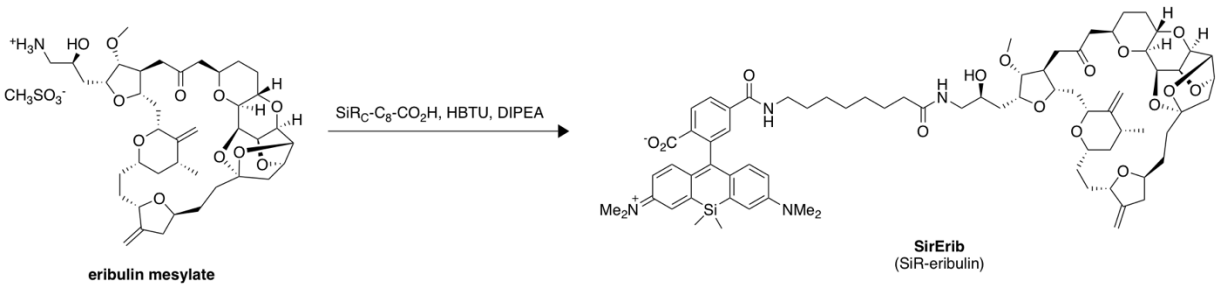

Figure S2.14. *Chemical synthesis of SirErib.*

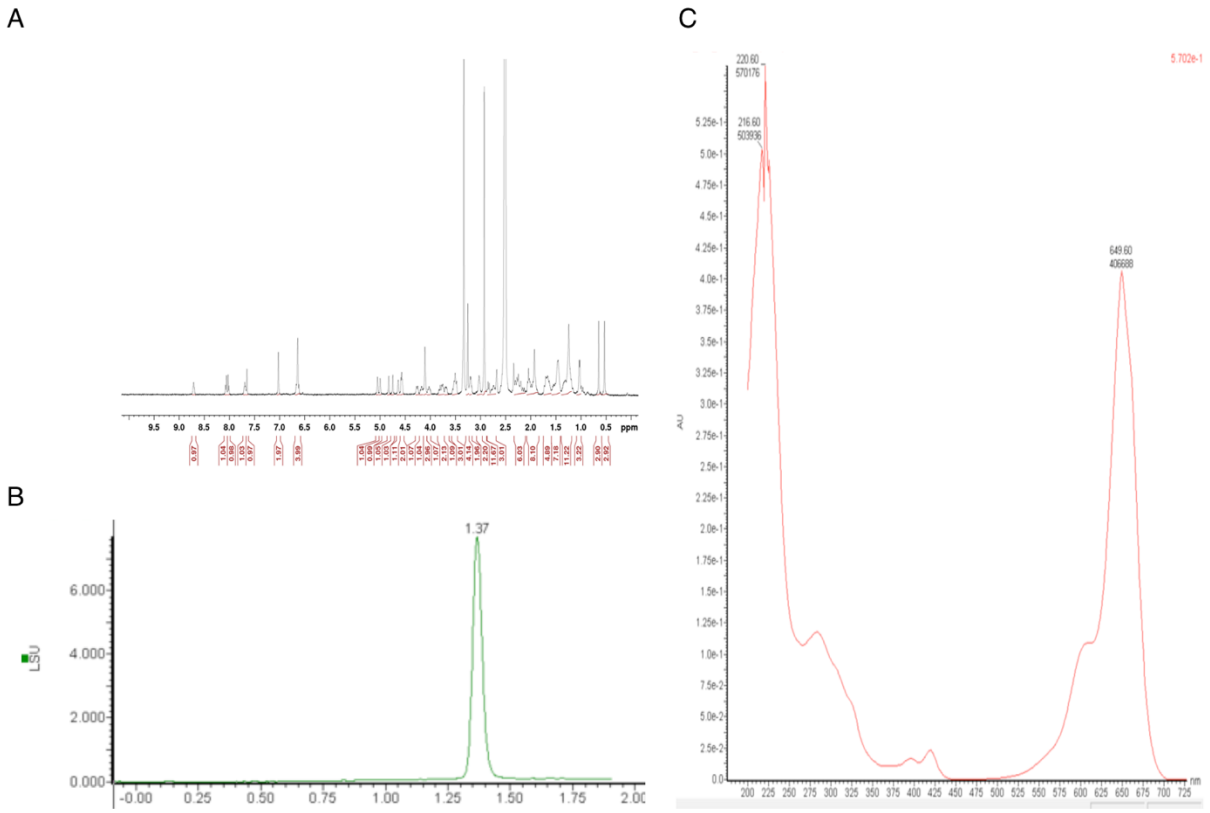

Figure S2.15. *Chemical characterization of SiR-eribulin. (A) [1]H NMR spectrum. (B) Chromatogram. ELSD signal, 0-2 min: 5-95% MeCN in water, 0.1% formic acid. (C) UV spectrum showing characteristic SiR absorption at 650 nm.*

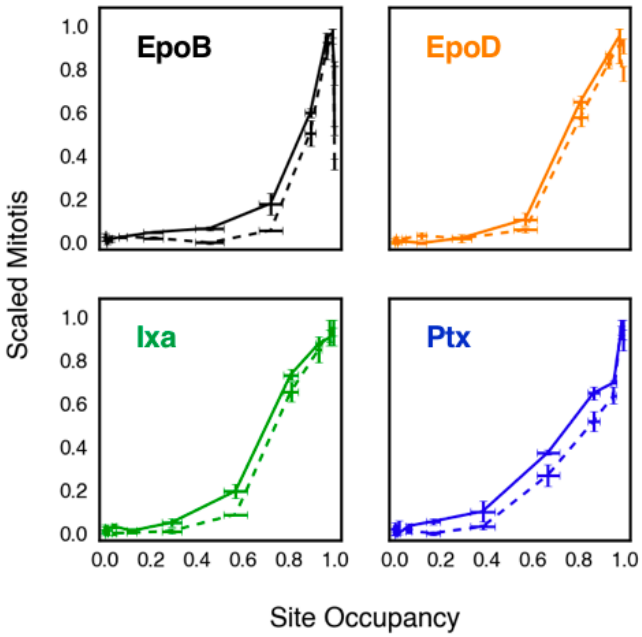

Figure S2.16. *Validation of mitotic scoring using SiR-eribulin. A 384-well plate of RPE1 cells expressing EB3-GFP was treated with the indicated drugs in triplicate. After 22 hours, mitotic cells were imaged using the EB3-GFP channel (solid lines) as in Fig. S2.5. Immediately after imaging, the same plate of cells was treated with 10 μM EpoB for 10 min. The plate was then stained with 100nM SiR-eribulin (SirErib) in the presence of 10 μM EpoB for 30 min before re-imaging. The same instrument settings were used to image the plate again but using the far-red SirErib channel (dotted lines).*

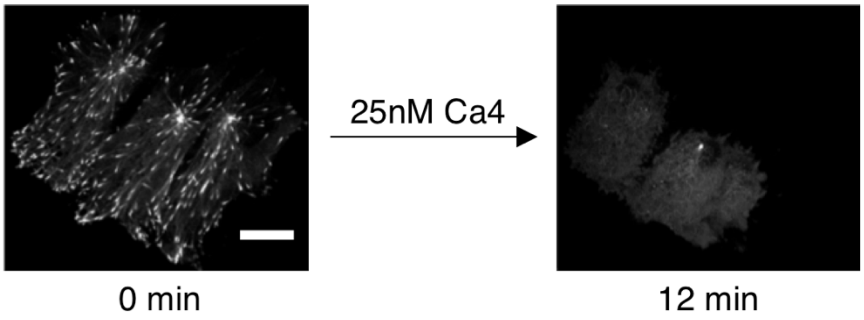

Figure S3.1. *Sample EB3 comet images before and after treatment with 25 nM Ca4. Note the more rounded morphology in the 12-min image. Scale bar = 10 μm.*

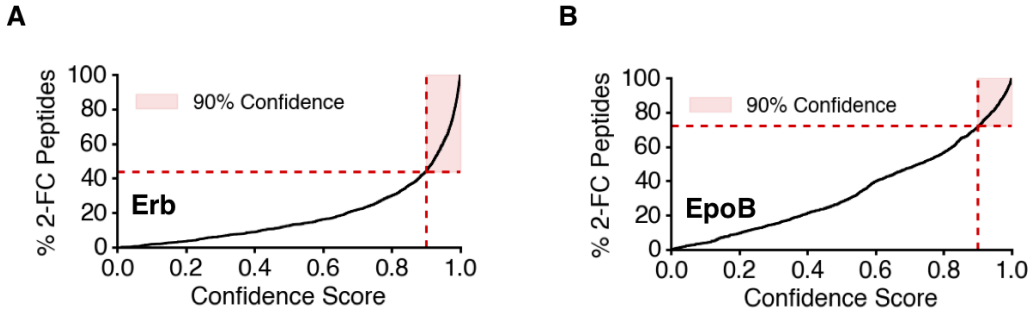

Figure S3.2. *Cumulative distribution of confidence scores with respect to all phosphopeptides having greater than 2-fold change. Shaded region denotes phosphopeptides with confidence scores greater than 90 percent. (A) Erb. (B) EpoB.*

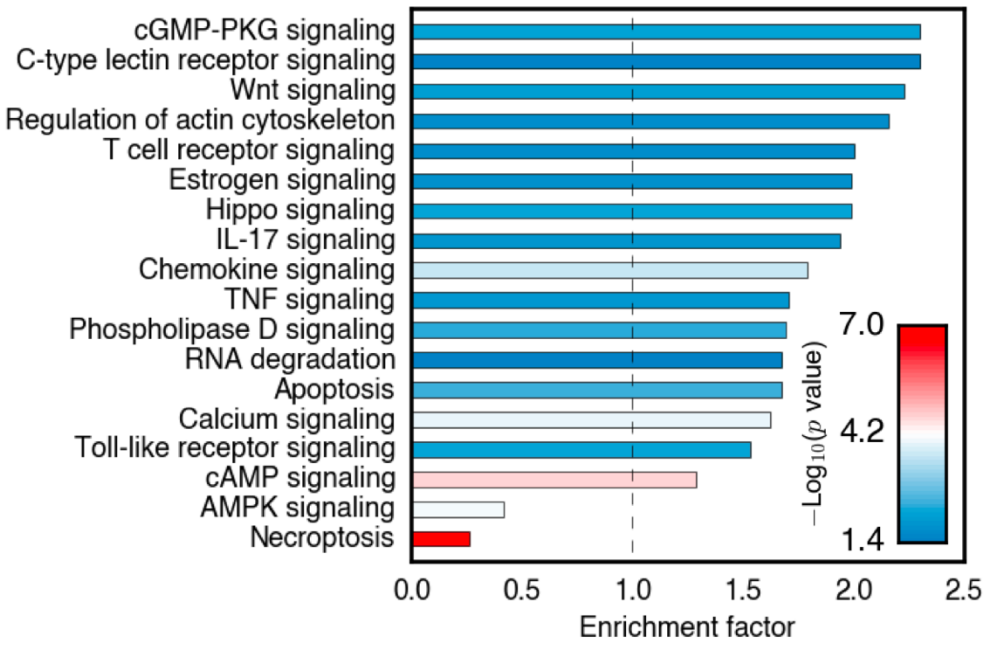

Figure S3.3. *Subset of statistically enriched KEGG pathways in the phosphoproteome induced by Erb ($p < 0.05$, Fisher's exact test). Pathways that are over-represented have enrichment factors greater than 1, whereas under-represented pathways have enrichment factors less than 1. P values are denoted by color.*

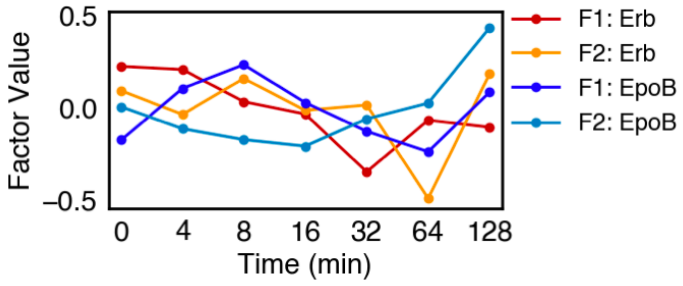

Figure S3.4. *Factor analysis data projections. For each drug, the two factors with the greatest internal variance were selected (i.e. F1 = factor 1).*

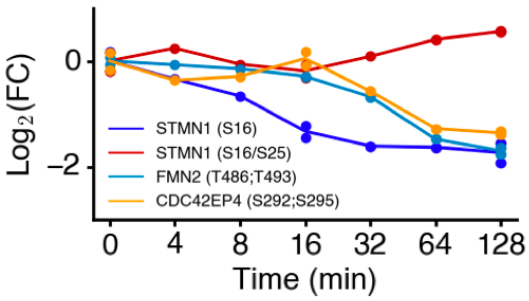

Figure S3.5. *Phosphopeptide profiles for MT and actin-relevant phosphosites stimulated by Erb. Note the opposing direction of the double phosphosite (S16/S25) for STMN1, which suggests that the loss of the singly phosphorylated peptide (S16) is due to phosphorylation of S25.*

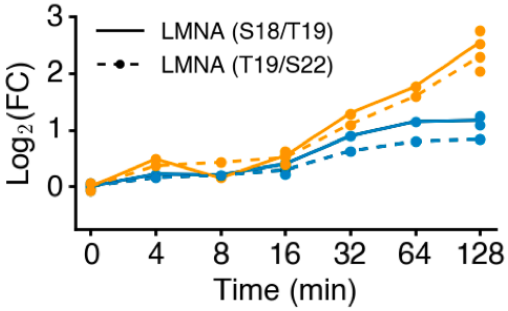

Figure S3.6. *LMNA "CDK1" sites are phosphorylated in response to Erb (blue) and EpoB (orange) treatment.*

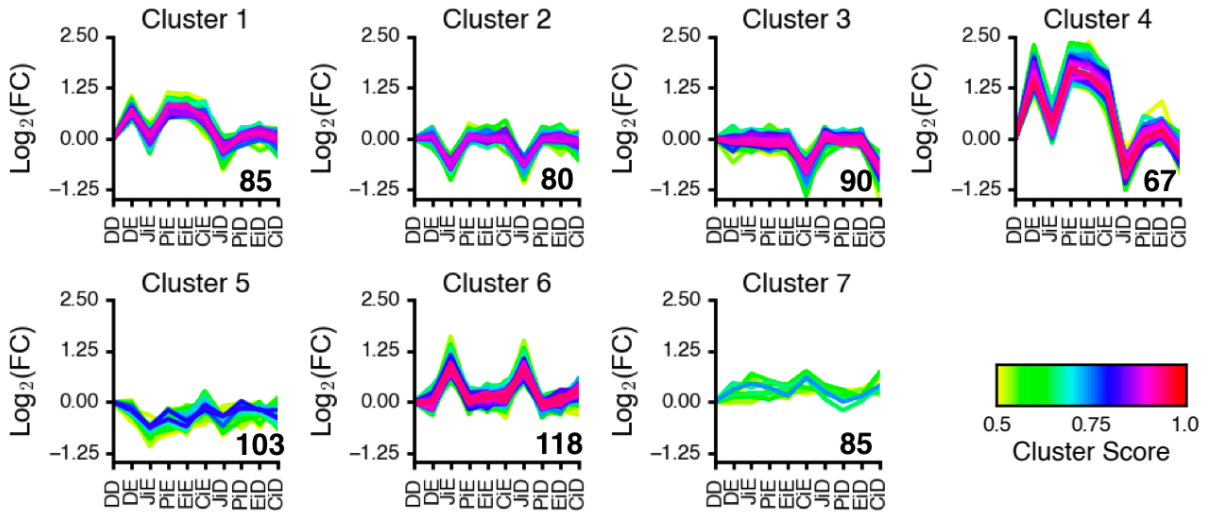

Sample annotation

DD: DMSO → DMSO
DE: DMSO → EpoB
JiE: JNK inhibitor → EpoB
PiE: p38 inhibitor → EpoB
EiE: ERK inhibitor → EpoB
CiE: CDK inhibitor → EpoB
JiD: JNK inhibitor → DMSO
PiD: p38 inhibitor → DMSO
EiD: ERK inhibitor → DMSO
CiD: CDK inhibitor → DMSO

Figure S3.7. *Fuzzy c-means clusters for combinatorial drug treatment data. Only phosphopeptides with greater than 1.5-fold change were used for the analysis. The number of peptides per cluster are annotated in bold at the bottom right corner of each plot. Cluster membership score is denoted by color.*

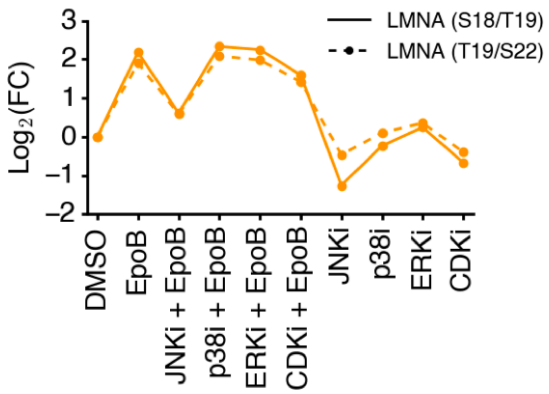

Figure S3.8. *LMNA "CDK1" sites are phosphorylated by JNK after EpoB treatment. The plot shows combinatorial drug treatments containing EpoB and inhibitors of JNK, p38, ERK, or CDKs.*

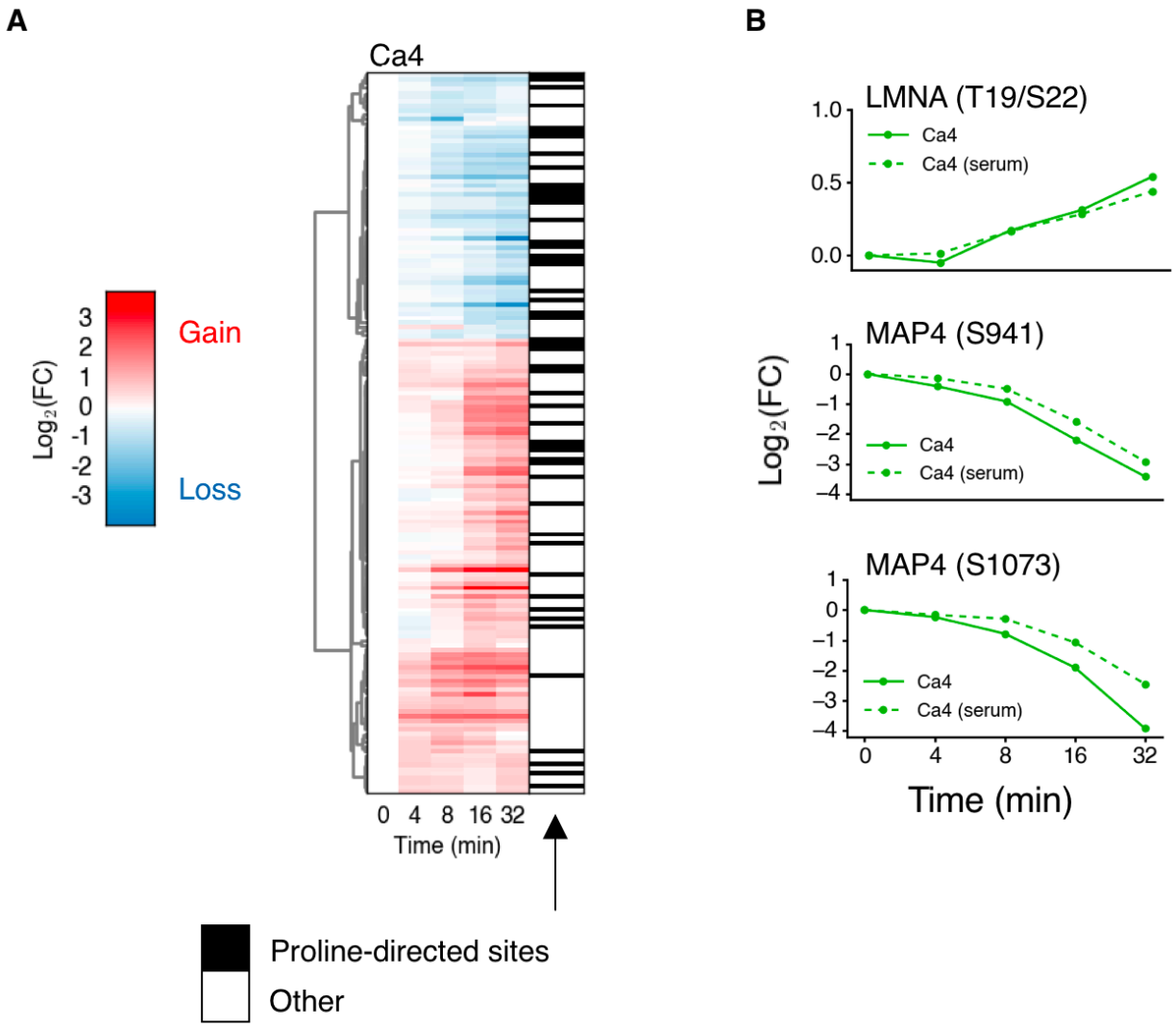

Figure S3.9: *Ca4 stimulates phospho-signaling comparable to Erb. (A) Heatmap showing phosphorylation and dephosphorylation stimulated by 400 nM Ca4. Proline-directed phosphosites are denoted by black lines. (B) Phosphopeptide profiles for sites present in LMNA and MAP4 that were previously detected for Erb.*

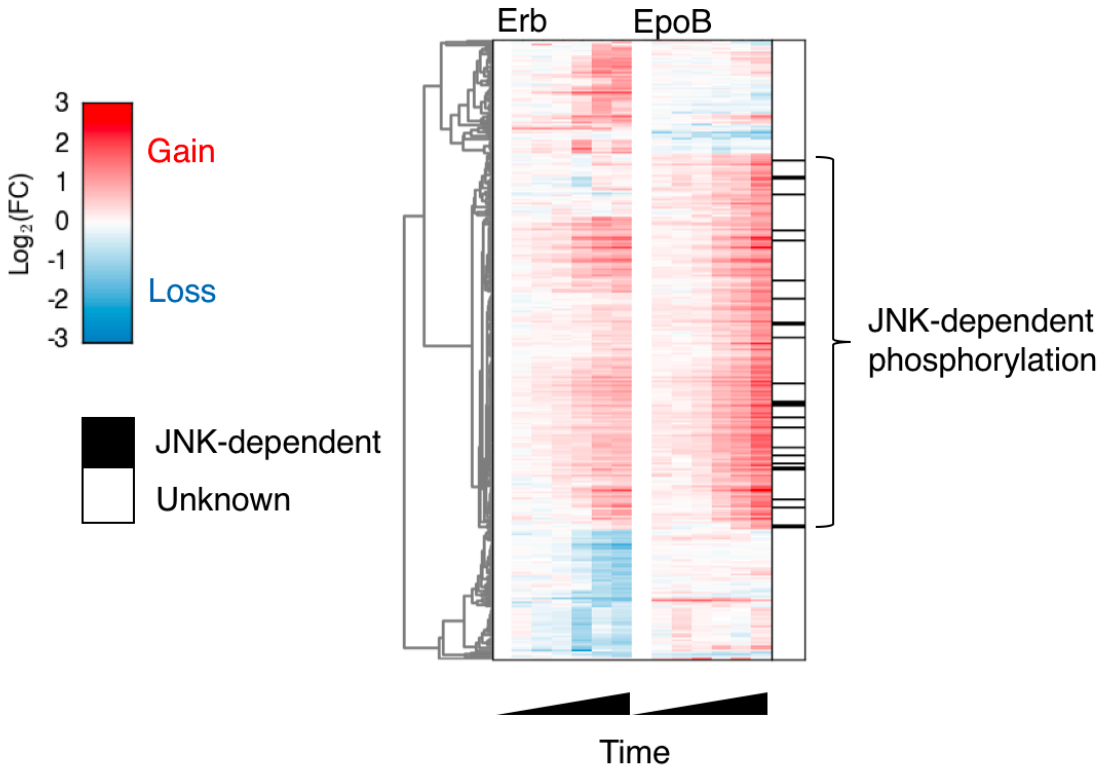

Figure S3.10: *Heatmap showing JNK-dependent phosphorylation. Only proline-directed phosphosites with confidence scores greater than 0.7 are shown. Sites verified to be JNK dependent are indicated by a black line. Note that only a proportion of peptides from the Erb/EpoB mass spec runs were detected in the combinatorial drug treatment run. Therefore, many more JNK dependent sites are likely, as hinted by this heatmap. JNK-dependent sites are denoted by black lines.*

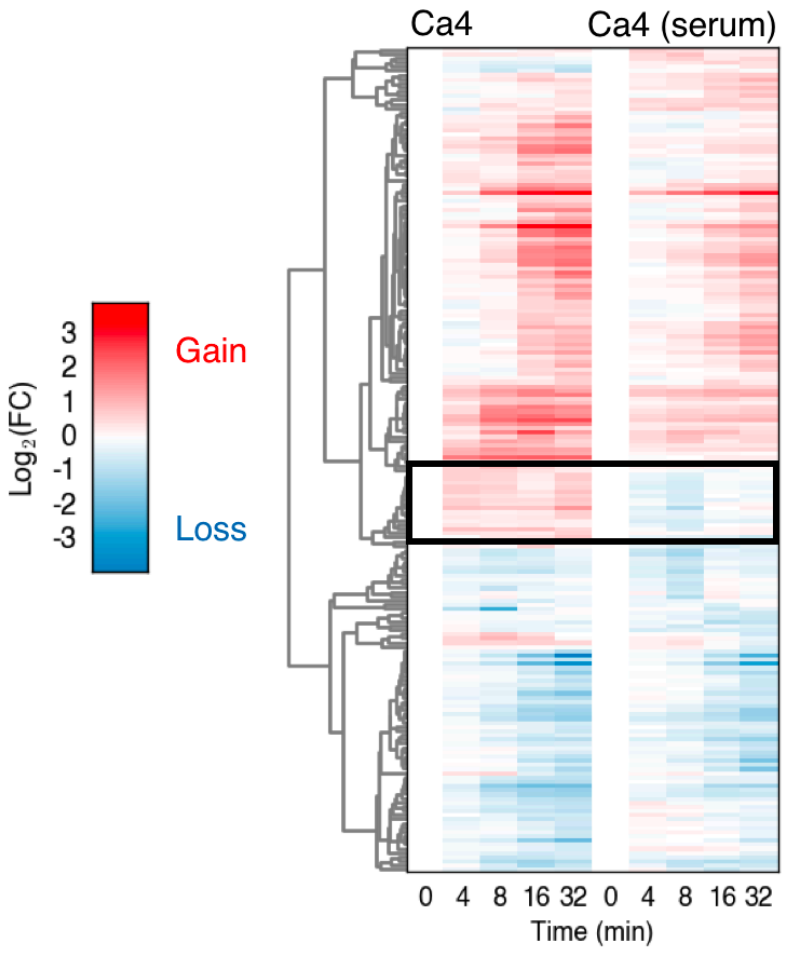

Figure S3.11: *Serum deprivation has little effect on Ca4-induced phospho-changes. Heatmap shows phosphorylation and dephosphorylation stimulated by 400 nM Ca4, with or without serum present. Black box encloses a cluster of phosphopeptides differentially regulated in the presence of serum. Note: half of these peptides belong to one protein (i.e. NUCKS1).*

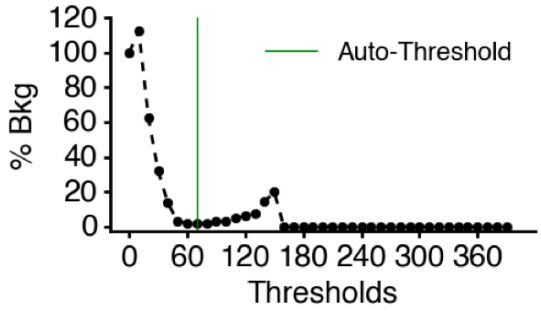

Figure S4.1. *Automated thresholding of a single cell. A range of thresholds was tested on the first (negative control) and last (positive control) time-points of the time-course (i.e. before drug treatment and after 4 μM Ca4 treatment, respectively). The ratio of positive control comets over negative control comets was taken to represent the percent of false positives, or background. The threshold was set to the first local minimum (green line).*

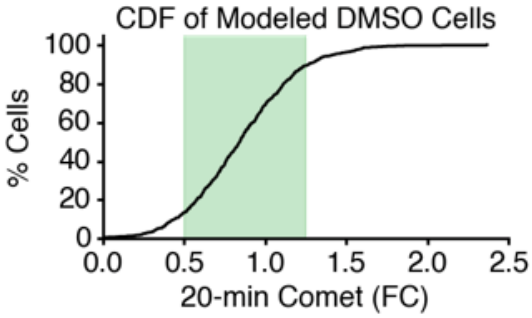

Figure S4.2. *Cumulative distribution of modeled comet loss after 20 minutes of DMSO control. Cells with at least 35 comets before drug treatment and less than 20 percent background were included in the analysis. Green shaded region corresponds to the red-boxed region in the DMSO plot in Fig. 4.4C. N = 710 cells.*

References

1. Perrett, D. From 'protein' to the beginnings of clinical proteomics. *Proteomics Clin Appl* **1,** 720–738 (2007).

2. Pauling, L., Corey, R. B. & Branson, H. R. The structure of proteins: Two hydrogen-bonded helical configurations of the polypeptide chain. *Proc Natl Acad Sci U S A* **37,** 205–211 (1951).

3. Graham, W. & Roberts, J. B. Intravenous colchicine in the management of gouty arthritis. *Ann Rheum Dis* **12,** 16–19 (1953).

4. Shelanski, M. L. & Taylor, E. W. Isolation of a protein subunit from microtubules. *J Cell Biol* **34,** 549–554 (1967).

5. Bhamidipathi, A., Lewis, S. A. & Cowan, N. J. ADP ribosylation factor-like protein 2 (Arl2) regulates the interaction of tubulin-folding cofactor D with native tubulin. *J Cell Biol* **149,** 1087–1096 (2000).

6. Cowan, N. J. & Lewis, S. A. Type II chaperonins, prefoldin, and the tubulin-specific chaperones. *Adv Protein Chem* **59,** 73–104 (2001).

7. Lewis, S. A., Tian, G. & Cowan, N. J. The alpha- and beta-tubulin folding pathways. **7,** 479–485 (1997).

8. Tian, G. *et al.* Tubulin subunits exist in an activated conformational state generated and maintained by protein cofactors. *J Cell Biol* **138,** 821–832 (1997).

9. Carlier, M. F. & Pantaloni, D. Kinetic analysis of guanosine 5'-triphosphate hydrolysis associated with tubulin polymerization. *Biochemistry* **20,** 1918–1924 (1981).

10. Nogales, E., Wolf, S. G. & Downing, K. H. Structure of the alpha beta tubulin dimer by electron crystallography. *Nature* **391,** 199–203 (1998).

11. Nogales, E., Whittaker, M., Milligan, R. A. & Downing, K. H. High-resolution model of the microtubule. *Cell* **96,** 79–88 (1999).

12. Tilney, L. G. *et al.* Microtubules: evidence for 13 protofilaments. *J Cell Biol* **59,** 267–275 (1973).

13. Hyman, A. A., Salser, S., Drechsel, D. N., Unwin, N. & Mitchison, T. J. Role of GTP hydrolysis in microtubule dynamics: information from a slowly hydrolyzable analogue, GMPCPP. *Mol Biol Cell* **3,** 1155–1167 (1992).

14. Seetapun, D., Castle, B. T., McIntyre, A. J., Tran, P. T. & Odde, D. J. Estimating the microtubule GTP cap size in vivo. *Curr Biol* **22,** 1681–1687 (2012).

15. Conduit, P. T., Wainman, A. & Raff, J. W. Centrosome function and assembly in animal cells. *Nat Rev Mol Cell Biol* **16,** 611–624 (2015).

16. Chabin-Brion, K. *et al.* The Golgi complex is a microtubule-organizing organelle. *Mol Biol Cell* **12,** 2047–2060 (2001).

17. Moritz, M., Braunfeld, M. B., Guenebaut, V., Heuser, J. & Agard, D. A. Structure of the gamma-tubulin ring complex: a template for microtubule nucleation. *Nat Cell Biol* **2,** 365–370 (2000).

18. Mitchison, T. & Kirschner, M. Dynamic instability of microtubule growth. *Nature* **312,** 237–242 (1984).

19. Maccioni, R. B. & Cambiazo, V. Role of microtubule-associated proteins in the control of microtubule assembly. *Physiol Rev* **75,** 835–864 (1995).

20. Akhmanova, A. & Hoogenraad, C. C. Microtubule plus-end-tracking proteins: mechanisms and functions. *Curr Opin Cell Biol* **17,** 47–54 (2005).

21. Belmont, L. D. & Mitchison, T. J. Identification of a protein that interacts with tubulin dimers and increases the catastrophe rate of microtubules. *Cell* **84,** 623–631 (1996).

22. Gardner, M. K., Zanic, M., Gell, C., Bormuth, V. & Howard, J. Depolymerizing kinesins Kip3 and MCAK shape cellular microtubule architecture by differential control of catastrophe. *Cell* **147,** 1092–1103 (2011).

23. Vale, R. D. Severing of stable microtubules by a mitotically activated protein in Xenopus egg extracts. *Cell* **64,** 827–839 (1991).

24. Gadadhar, S., Bodakuntla, S., Natarajan, K. & Janke, C. The tubulin code at a glance. *J Cell Sci* **130,** 1347–1353 (2017).

25. Peris, L. *et al.* Motor-dependent microtubule disassembly driven by tubulin tyrosination. *J Cell Biol* **185,** 1159–1166 (2009).

26. Bonnet, C. *et al.* Differential binding regulation of microtubule-associated proteins MAP1A, MAP1B, and MAP2 by tubulin polyglutamylation. *J Biol Chem* **276,** 12839–12848 (2001).

27. Boucher, D., Larcher, J. C., Gros, F. & Denoulet, P. Polyglutamylation of tubulin as a progressive regulator of in vitro interactions between the microtubule-associated protein Tau and tubulin. *Biochemistry* **33,** 12471–12477 (1994).

28. Lacroix, B. *et al.* Tubulin polyglutamylation stimulates spastin-mediated microtubule severing. *J Cell Biol* **189,** 945–954 (2010).

29. Valenstein, M. L. & Roll-Mecak, A. Graded Control of Microtubule Severing by Tubulin Glutamylation. *Cell* **164,** 911–921 (2016).

30. Illenberger, S. *et al.* Phosphorylation of microtubule-associated proteins MAP2 and MAP4 by the protein kinase p110mark. Phosphorylation sites and regulation of microtubule dynamics. *J Biol Chem* **271,** 10834–10843 (1996).

31. Ebneth, A., Drewes, G., Mandelkow, E. M. & Mandelkow, E. Phosphorylation of MAP2c and MAP4 by MARK kinases leads to the destabilization of microtubules in cells. *Cell Motil Cytoskeleton* **44,** 209–224 (1999).

32. Marklund, U., Larsson, N., Gradin, H. M., Brattsand, G. & Gullberg, M. Oncoprotein 18 is a phosphorylation-responsive regulator of microtubule dynamics. *EMBO J* **15,** 5290–5298 (1996).

33. Di Paolo, G., Antonsson, B., Kassel, D., Riederer, B. M. & Grenningloh, G. Phosphorylation regulates the microtubule-destabilizing activity of stathmin and its interaction with tubulin. *FEBS Lett* **416,** 149–152 (1997).

34. Gradin, H. M., Larsson, N., Marklund, U. & Gullberg, M. Regulation of microtubule dynamics by extracellular signals: cAMP-dependent protein kinase switches off the activity of oncoprotein 18 in intact cells. *J Cell Biol* **140,** 131–141 (1998).

35. Melander Gradin, H., Marklund, U., Larsson, N., Chatila, T. A. & Gullberg, M. Regulation of microtubule dynamics by Ca2+/calmodulin-dependent kinase IV/Gr-dependent phosphorylation of oncoprotein 18. *Mol Cell Biol* **17,** 3459–3467 (1997).

36. Daub, H., Gevaert, K., Vandekerckhove, J., Sobel, A. & Hall, A. Rac/Cdc42 and p65PAK regulate the microtubule-destabilizing protein stathmin through phosphorylation at serine 16. *J Biol Chem* **276,** 1677–1680 (2001).

37. Borisy, G. G. & Taylor, E. W. The mechanism of action of colchicine. Binding of colchincine-3H to cellular protein. *J Cell Biol* **34,** 525–533 (1967).

38. Jordan, M. A., Thrower, D. & Wilson, L. Effects of vinblastine, podophyllotoxin and nocodazole on mitotic spindles. Implications for the role of microtubule dynamics in mitosis. *J Cell Sci* **102,** 401–416 (1992).

39. Jordan, M. A., Toso, R. J., Thrower, D. & Wilson, L. Mechanism of mitotic block and inhibition of cell proliferation by taxol at low concentrations. *Proc Natl Acad Sci U S A* **90,** 9552–9556 (1993).

40. Derry, W. B., Wilson, L. & Jordan, M. A. Substoichiometric binding of taxol suppresses microtubule dynamics. *Biochemistry* **34,** 2203–2211 (1995).

41. Ravelli, R. B. *et al.* Insight into tubulin regulation from a complex with colchicine and a stathmin-like domain. *Nature* **428,** 198–202 (2004).

42. Hoebeke, J., Van Nijen, G. & De Brabander, M. Interaction of oncodazole (R 17934), a new antitumoral drug, with rat brain tubulin. *Biochem Biophys Res Commun* **69,** 319–324 (1976).

43. Lin, C. M. *et al.* Interactions of tubulin with potent natural and synthetic analogs of the antimitotic agent combretastatin: a structure-activity study. *Mol Pharmacol* **34,** 200–208 (1988).

44. Lin, C. M., Ho, H. H., Pettit, G. R. & Hamel, E. Antimitotic natural products combretastatin A-4 and combretastatin A-2: studies on the mechanism of their inhibition of the binding of colchicine to tubulin. *Biochemistry* **28,** 6984–6991 (1989).

45. Nogales, E., Wolf, S. G., Khan, I. A., Luduena, R. F. & Downing, K. H. Structure of tubulin at 6.5 A and location of the taxol-binding site. *Nature* **375,** 424–427 (1995).

46. Elie-Caille, C. *et al.* Straight GDP-tubulin protofilaments form in the presence of taxol. *Curr Biol* **17,** 1765–1570 (2007).

47. Nettles, J. H. *et al.* The binding mode of epothilone A on alpha,beta-tubulin by electron crystallography. *Science* **305,** 866–869 (2004).

48. Gigant, B. *et al.* Structural basis for the regulation of tubulin by vinblastine. *Nature* **435,** 519–522 (2005).

49. Amos, L. A., Jubb, J. S., Henderson, R. & Vigers, G. Arrangement of protofilaments in two forms of tubulin crystal induced by vinblastine. *J Mol Biol* **178,** 711–729 (1984).

50. Wilson, L., Jordan, M. A. & Morse, A. Interaction of vinblastine with steady-state microtubules in vitro. *J Mol Biol* **159,** 125–149 (1982).

51. Doodhi, H. *et al.* Termination of protofilament elongation by eribulin induces lattice defects that promote microtubule catastrophes. *Curr Biol* **26,** 1713–1721 (2016).

52. Saez-Calvo, G. *et al.* Triazolopyrimidines are microtubule-stabilizing agents that bind the vinca inhibitor site of tubulin. *Cell Chem Biol* **24,** 737–750 (2017).

53. Prota, A. E. *et al.* A new tubulin-binding site and pharmacophore for microtubule-destabilizing anticancer drugs. *Proc Natl Acad Sci U S A* **111,** 13817–13821 (2014).

54. Prota, A. E. *et al.* Structural basis of microtubule stabilization by laulimalide and peloruside A. *Angew Chem Int Ed Engl* **53,** 1621–1625 (2014).

55. Yang, J. *et al.* Pironetin reacts covalently with cysteine-316 of α-tubulin to destabilize microtubule. *Nat Commun* **7,** 12103 (2016).

56. Prota, A. E. *et al.* Pironetin binds covalently to αCys316 and perturbs a major loop and helix of α-tubulin to inhibit microtubule formation. *J Mol Biol* **428,** 2981–2988 (2016).

57. Rusan, N. M., Fagerstrom, C. J., Yvon, A. M. & Wadsworth, P. Cell cycle-dependent changes in microtubule dynamics in living cells expressing green fluorescent protein-alpha tubulin. *Mol Biol Cell* **12,** 971–980 (2001).

58. Gascoigne, K. E. & Taylor, S. S. How do anti-mitotic drugs kill cancer cells. *J Cell Sci* **122,** 2579–2585 (2009).

59. Jordan, M. A. & Wilson, L. Microtubules as a target for anticancer drugs. *Nat Rev Cancer* **4,** 253–265 (2004).

60. Zasadil, L. M. *et al.* Cytotoxicity of paclitaxel in breast cancer is due to chromosome missegregation on multipolar spindles. *Sci Transl Med* **6,** 229ra43 (2014).

61. Harding, S. M. *et al.* Mitotic progression following DNA damage enables pattern recognition within micronuclei. *Nature* **548,** 466–470 (2017).

62. Wang, T. H. *et al.* Microtubule-interfering agents activate c-Jun N-terminal kinase/stress-activated protein kinase through both Ras and apoptosis signal-regulating kinase pathways. *J Biol Chem* **273,** 4928–4936 (1998).

63. Shore, V. H. *et al.* Vascular endothelial growth factor, placenta growth factor and their receptors in isolated human trophoblast. *Placenta* **18,** 657–665 (1997).

64. Chen, J., Sun, W. L., Wasylyk, B., Wang, Y. P. & Zheng, H. c-Jun N-terminal kinase mediates microtubule-depolymerizing agent-induced microtubule depolymerization and G2/M arrest in MCF-7 breast cancer cells. **23,** 98–107 (2012).

65. Boldt, S., Weidle, U. H. & Kolch, W. The role of MAPK pathways in the action of chemotherapeutic drugs. *Carcinogenesis* **23,** 1831–1838 (2002).

66. Okano, J. & Rustgi, A. K. Paclitaxel induces prolonged activation of the Ras/MEK/ERK pathway independently of activating the programmed cell death machinery. *J Biol Chem* **276,** 19555–19564 (2001).

67. Kuntziger, T., Gavet, O., Manceau, V., Sobel, A. & Bornens, M. Stathmin/Op18 phosphorylation is regulated by microtubule assembly. *Mol Biol Cell* **12,** 437–448 (2001).

68. Weisenberg, R. C., Borisy, G. G. & Taylor, E. W. The colchicine-binding protein of mammalian brain and its relation to microtubules. *Biochemistry* **7,** 4466–4479 (1968).

69. Lee, J. C. & Timasheff, S. N. In vitro reconstitution of calf brain microtubules: effects of solution variables. *Biochemistry* **16,** 1754–1764 (1977).

70. Castoldi, M. & Popov, A. V. Purification of brain tubulin through two cycles of polymerization-depolymerization in a high-molarity buffer. *Protein Expr Purif* **32,** 83–88 (2003).

71. Diaz, J. F., Barasoain, I. & Andreu, J. M. Fast kinetics of Taxol binding to microtubules. Effects of solution variables and microtubule-associated proteins. *J Biol Chem* **278,** 8407–8419 (2003).

72. Wadsworth, P. & McGrail, M. Interphase microtubule dynamics are cell type-specific. *J Cell Sci* **95,** 23–32 (1990).

73. Tanaami, T. *et al.* High-speed 1-frame/ms scanning confocal microscope with a microlens and Nipkow disks. *Appl Opt* **41,** 4704–4708 (2002).

74. Chen, B.-C. *et al.* Lattice light-sheet microscopy: Imaging molecules to embryos at high spatiotemporal resolution. *Science* **346,** 1257998 (2014).

75. Matov, A. *et al.* Analysis of microtubule dynamic instability using a plus-end growth marker. *Nat Methods* **7,** (2010).

76. Boutros, M., Heigwer, F. & Laufer, C. Microscopy-based high-content screening. *Cell* **163,** 1314–1325 (2015).

77. Zhang, J. H., Chung, T. D. & Oldenburg, K. R. A simple statistical parameter for use in evaluation and validation of high throughput screening assays. **J Biomol Screen,**

78. Mann, M. & Wilm, M. Error-tolerant identification of peptides in sequence databases by peptide sequence tags. *Anal Chem* **66,** 4390–4399 (1994).

79. Eng, J. K., McCormack, A. L. & Yates, J. R. An approach to correlate tandem mass spectral data of peptides with amino acid sequences in a protein database. *J Am Soc Mass Spectrom* **5,** 976–989 (1994).

80. Nesvizhskii, A. I., Keller, A., Kolker, E. & Aebersold, R. A statistical model for identifying proteins by tandem mass spectrometry. *Anal Chem* **75,** 4646–4658 (2003).

81. Cox, J. & Mann, M. MaxQuant enables high peptide identification rates, individualized p.p.b.- range mass accuracies and proteome-wide protein quantification. *Nat Biotechnol* **26,** 1367–1372 (2008).

82. Ong, S. E. *et al.* Stable isotope labeling by amino acids in cell culture, SILAC, as a simple and accurate approach to expression proteomics. *Mol Cell Proteomics* **1,** 376–386 (2002).

83. Hsu, J. L., Huang, S. Y., Chow, N. H. & Chen, S. H. Stable-isotope dimethyl labeling for quantitative proteomics. *Anal Chem* **75,** 6843–6852 (2003).

84. Thompson, A. *et al.* Tandem mass tags: a novel quantification strategy for comparative analysis of complex protein mixtures by MS/MS. *Anal Chem* **75,** 1895–1904 (2003).

85. McAlister, G. *et al.* Increasing the multiplexing capacity of TMTs using reporter ion isotopologues with isobaric masses. *Anal Chem* **84,** 7469–7478 (2012).

86. Werner, T. *et al.* High-resolution enabled TMT 8-plexing. *Anal Chem* **84,** 7188–7194 (2012).

87. Ting, L., Rad, R., Gygi, S. P. & Haas, W. MS3 eliminates ratio distortion in isobaric multiplexed quantitative proteomics. *Nat Methods* **8,** 937–940 (2011).

88. McAlister, G. C. *et al.* MultiNotch MS3 enables accurate, sensitive, and multiplexed detection of differential expression across cancer cell line proteomes. *Anal Chem* **86,** 7150–7158 (2014).

89. Kettenbach, A. N. & Gerber, S. A. Rapid and reproducible single-stage phosphopeptide enrichment of complex peptide mixtures: application to general and phosphotyrosine-specific phosphoproteomics experiments. *Anal Chem* **83,** 7635–7644 (2011).

90. Thingholm, T. E., Jorgensen, T. J., Jensen, O. N. & Larsen, M. R. Highly selective enrichment of phosphorylated peptides using titanium dioxide. *Nat Protoc* **1,** 1929–1935 (2006).

91. Fila, J. & Honys, D. Enrichment techniques employed in phosphoproteomics. *Amino Acids* **43,** 1025–1047 (2012).

92. Lehmann, W. D. *et al.* Neutral loss-based phosphopeptide recognition: a collection of caveats. *J Proteome Res* **6,** 2866–2873 (2007).

93. Nagano, K. *et al.* Phosphoproteomic analysis of distinct tumor cell lines in response to nocodazole treatment. *Proteomics* **9,** 2861–2874 (2009).

94. Black, J. W. & Leff, P. Operational models of pharmacological agonism. *Proc R Soc Lond B Biol Sci* **220,** 141–162 (1983).

95. Cheng, Y. & Prusoff, W. H. Relationship between the inhibition constant (K1) and the concentration of inhibitor which causes 50 per cent inhibition (I50) of an enzymatic reaction. *Biochem Pharmacol* **22,** 3099–3108 (1973).

96. Stoddart, L. A., White, C. W., Nguyen, K., Hill, S. J. & Pfleger, K. D. Fluorescence- and bioluminescence-based approaches to study GPCR ligand binding. *Br J Pharmacol* **173,** 3028–3037 (2016).

97. Horwitz, S. B. Taxol (paclitaxel): mechanisms of action. *Ann Oncol* **5 Suppl 6,** S3-6 (1994).

98. Skeel, R. T. & Khlief, S. N. *Handbook of Cancer Chemotherapy*. (Lippincott Williams and Wilkins, 2011).

99. Yared, J. A. & Tkaczuk, K. H. R. Update on taxane development: new analogs and new formulations. *Drug Des Devel Ther* **6,** 371–384 (2012).

100. Fitzgerald, D. P. *et al.* TPI-287, a new taxane family member, reduces the brain metastatic colonization of breast cancer cells. *Mol Cancer Ther* **11,** 1959–1967 (2012).

101. Rohena, C. C. & Mooberry, S. L. Recent progress with microtubule stabilizers: new compounds, binding modes and cellular activities. *Nat Prod Rep* **31,** 335–355 (2014).

102. Hunt, J. T. Discovery of ixabepilone. *Mol Cancer Ther* **8,** 275–281 (2009).

103. Brunden, K. R. *et al.* The characterization of microtubule-stabilizing drugs as possible therapeutic agents for Alzheimer's disease and related tauopathies. *Pharmacol Res* **63,** 341–351 (2011).

104. Barten, D. M. *et al.* Hyperdynamic microtubules, cognitive deficits, and pathology are improved in tau transgenic mice with low doses of the microtubule-stabilizing agent BMS-241027. *J Neurosci* **32,** 7137–7145 (2012).

105. Zhang, B. *et al.* The microtubule-stabilizing agent, epothilone D, reduces axonal dysfunction, neurotoxicity, cognitive deficits, and Alzheimer-like pathology in an interventional study with aged tau transgenic mice. *J Neurosci* **32,** 3601–3611 (2012).

106. Prota, A. E. *et al.* Molecular mechanism of action of microtubule-stabilizing anticancer agents. *Science* **339,** 587–590 (2013).

107. Kellogg, E. H. *et al.* Insights into the distinct mechanisms of action of taxane and non-taxane microtubule stabilizers from cryo-EM structures. *J Mol Biol* **429,** 633–646 (2017).

108. Jordan, M. A. *et al.* Mitotic block induced in HeLa cells by low concentrations of paclitaxel (Taxol) results in abnormal mitotic exit and apoptotic cell death. *Cancer Res* **56,** 816–825 (1996).

109. Soltys, B. J. & Gupta, R. S. Interrelationships of endoplasmic reticulum, mitochondria, intermediate filaments, and microtubules--a quadruple fluorescence labeling study. *Biochem Cell Biol* **70,** 1174–1186 (1992).

110. Wang, T. H. *et al.* Microtubule dysfunction induced by paclitaxel initiates apoptosis through both c-Jun N-terminal kinase (JNK)-dependent and -independent pathways in ovarian cancer cells. *J Biol Chem* **274,** 8208–8216 (1999).

111. Darshan, M. S. *et al.* Taxane-induced blockade to nuclear accumulation of the androgen receptor predicts clinical responses in metastatic prostate cancer. *Cancer Res* **71,** 6019–6029 (2011).

112. Komlodi-Pasztor, E., Sackett, D., Wilkerson, J. & Fojo, T. Mitosis is not a key target of microtubule agents in patient tumors. *Nat Rev Clin Oncol* **8,** 244–250 (2011).

113. Weaver, B. A. How Taxol/paclitaxel kills cancer cells. *Mol Biol Cell* **25,** 2677–2681 (2014).

114. Altmann, K. H., Pfeiffer, B., Arseniyadis, S., Pratt, B. A. & Nicolaou, K. C. The chemistry and biology of epothilones - the wheel keeps turning. *ChemMedChem* **2,** 396–423 (2007).

115. Altmann, K. H., Gaugaz, F. Z. & Schiess, R. Diversity through semisynthesis: the chemistry and biological activity of semisynthetic epothilone derivatives. *Mol Divers* **15,** 383–399 (2011).

116. Chou, T. C. *et al.* Desoxyepothilone B: an efficacious microtubule-targeted antitumor agent with a promising in vivo profile relative to epothilone B. *Proc Natl Acad Sci U S A* **95,** 9642–9647 (1998).

117. Andreu, J. M. & Barasoain, I. The interaction of baccatin III with the taxol binding site of microtubules determined by a homogeneous assay with fluorescent taxoid. *Biochemistry* **40,** 11975–11984 (2001).

118. Diaz, J. F., Strobe, R., Engelborghs, Y., Souto, A. A. & Andreu, J. M. Molecular recognition of taxol by microtubules. Kinetics and thermodynamics of binding of fluorescent taxol derivatives to an exposed site. *J Biol Chem* **275,** 26265–26276 (2000).

119. Buey, R. M. *et al.* Interaction of epothilone analogs with the paclitaxel binding site: relationship between binding affinity, microtubule stabilization, and cytotoxicity. *Chem Biol* **11,** 225–236 (2004).

120. Buey, R. M. *et al.* Microtubule interactions with chemically diverse stabilizing agents: thermodynamics of binding to the paclitaxel site predicts cytotoxicity. *Chem Biol* **12,** 1269–1279 (2005).

121. Lukinavicius, G. *et al.* Fluorogenic probes for live-cell imaging of the cytoskeleton. *Nat Methods* **11,** 731–733 (2014).

122. Kuh, H.-J., Jang, S. H., Wientjes, G. & Au, J. L. Computational model of intracellular pharmacokinetics of paclitaxel. *J Pharmacol Exp Ther* **293,** 761–770 (2000).

123. Bellamy, W. T. P-glycoproteins and multidrug resistance. Annu Rev Pharmacol Toxicol. *Annu Rev Pharmacol Toxicol* **36,** 161–183 (1996).

124. Brunden, K. R., Trojanowski, J. Q., Smith, A. B. 3rd, Lee, V. M. & Ballatore, C. Microtubule-stabilizing agents as potential therapeutics for neurodegenerative disease. *Bioorg Med Chem* **22,** 5040–5049 (2014).

125. Stepanova, T. *et al.* Visualization of microtubule growth in cultured neurons via the use of EB3-GFP (end-binding protein 3-green fluorescent protein). *J Neurosci* **23,** 2655–2664 (2003).

126. Rose, W. C. Taxol-based combination chemotherapy and other in vivo preclinical antitumor studies. *J Natl Cancer Inst Monogr* **15,** 47–53 (1993).

127. Milross, C. G. *et al.* Relationship of mitotic arrest and apoptosis to antitumor effect of paclitaxel. *J Natl Cancer Inst* **88,** 1308–1314 (1996).

128. Desai, N. *et al.* Increased antitumor activity, intratumor paclitaxel concentrations, and endothelial cell transport of cremophor-free, albumin-bound paclitaxel, ABI-007, compared with cremophor-based paclitaxel. *Clin Cancer Res* **12,** 1317–1324 (2006).

129. Orth, J. D. *et al.* Analysis of mitosis and antimitotic drug responses in tumors by in vivo microscopy and single-cell pharmacodynamics. *Cancer Res* **71,** 4608–4616 (2011).

130. Chittajallu, D. R. *et al.* In vivo cell-cycle profiling in xenograft tumors by quantitative intravital microscopy. *Nat Methods* **12,** 577–585 (2015).

131. Shi, J., Orth, J. D. & Mitchison, T. J. Cell type variation in responses to antimitotic drugs that target microtubules and kinesin-5. *Cancer Res* **68,** 3269–3276 (2008).

132. Rowinsky, E. K. & Donehower, R. C. Rowinsky EK, Donehower RC (1993) The clinical pharmacology of paclitaxel (Taxol). Semin Oncol 20:16-25. *Semin Oncol* **20,** 16–25 (1993).

133. Thrower, D., Jordan, M. A. & Wilson, L. Quantitation of cellular tubulin in microtubules and tubulin pools by a competitive ELISA. *J Immunol Methods* **136,** 45–51 (1991).

134. Shannon, K. B., Canman, J. C., Ben Moree, C., Tirmauer, J. S. & Salmon, E. D. Taxol-stabilized microtubules can position the cytokinetic furrow in mammalian cells. *Mol Biol Cell* **16,** 4423–4436 (2005).

135. Yang, Z., Kenny, A. E., Brito, D. A. & Rieder, C. L. Cells satisfy the mitotic checkpoint in Taxol, and do so faster in concentrations that stabilize syntelic attachments. *J Cell Biol* **186,** 675–684 (2009).

136. Mitchison, T. J. The proliferation rate paradox in antimitotic chemotherapy. *Mol Biol Cell* **23,** 1–6 (2012).

137. Symmans, W. F. *et al.* Paclitaxel-induced apoptosis and mitotic arrest assessed by serial fine-needle aspiration: implications for early prediction of breast cancer response to neoadjuvant treatment. *Clin Cancer Res* **6,** 4610–4617 (2000).

138. Mackenzie, K. J. *et al.* cGAS surveillance of micronuclei links genome instability to innate immunity. *Nature* **548,** 461–465 (2017).

139. Mitchison, T. J., Pineda, J., Shi, J. & Florian, S. Is inflammatory micronucleation the key to a successful anti-mitotic cancer drug? *Open Biol* **7,** 170182 (2017).

140. Kim, E., Yang, K. S., Giedt, R. J. & Weissleder, R. Red Si-rhodamine drug conjugates enable imaging in GFP cells. *Chem Commun (Camb)* **50,** 4504–4507 (2014).

141. Kim, E. *et al.* Optimized near-IR fluorescent agents for in vivo imaging of Btk expression. *Bioconjug Chem* **26,** 1513–1518 (2015).

142. Holmfedt, P., Sellin, M. E. & Gullberg, M. Predominant regulators of tubulin monomer-polymer partitioning and their implication for cell polarization. *Cell Mol Life Sci* **66,** 3263–3276 (2009).

143. Dumontet, C. & Jordan, M. A. Microtubule-binding agents: a dynamic field of cancer therapeutics. *Nat Rev Drug Discov* **9,** 790–803 (2010).

144. Komlodi-Pasztor, E., Sackett, D. & Fojo, A. T. Inhibitors targeting mitosis: tales of how great drugs against a promising target were brought down by a flawed rationale. *Clin Cancer Res* **18,** 51–63 (2012).

145. Salerni, B. L., Bates, D. J., Albershardt, T. C., Lowrey, C. H. & Eastman, A. Vinblastine induces acute, cell cycle phase-independent apoptosis in some leukemias and lymphomas and can induce acute apoptosis in others when Mcl-1 is suppressed. *Mol Cancer Ther* **9,** 791–802 (2010).

146. Kothari, A., Hittelman, W. N. & Chambers, T. C. Cell cycle-dependent mechanisms underlie vincristine-induced death of primary acute lymphoblastic leukemia cells. *Cancer Res* **76,** 3553–3561 (2016).

147. MacRae, T. H. Tubulin post-translational modifications--enzymes and their mechanisms of action. *Eur J Biochem* **244,** 265–278 (1997).

148. Lee, H. S. *et al.* Phosphorylation controls autoinhibition of cytoplasmic linker protein-170. *Mol Biol Cell* **21,** 2661–2673 (2010).

149. Beausoleil, S. A., Villen, J., Gerber, S. A., Rush, J. & Gygi, S. P. A probability-based approach for high-throughput protein phosphorylation analysis and site localization. *Nat Biotechnol* **24,** 1285–1292 (2006).

150. Lowe, J., Li, H., Downing, K. H. & Nogales, E. Refined structure of alpha beta-tubulin at 3.5 A resolution. *J Mol Biol* **313,** 1045–1057 (2001).

151. Gaspari, R., Prota, A. E., Bargsten, K., Cavalli, A. & Steinmetz, M. O. Structural basis of cis- and trans-combretastatin binding to tubulin. *Chem* **2,** 102–113 (2017).

152. Schuyler, S. C. & Pellman, D. Microtubule 'plus-end-tracking proteins': The end is just the beginning. *Cell* **105,** 421–424 (2001).

153. Krendel, M., Zenke, F. T. & Bokoch, G. M. Nucleotide exchange factor GEF-H1 mediates cross-talk between microtubules and the actin cytoskeleton. *Nat Cell Biol* **4,** 294–301 (2002).

154. Chang, Y. C., Nalbant, P., Birkenfeld, J., Chang, Z. F. & Bokoch, G. M. GEF-H1 couples nocodazole-induced microtubule disassembly to cell contractility via RhoA. *Mol Biol Cell* **19,** 2147–2153 (2008).

155. Murphy, J. P., Everley, R. A., Coloff, J. L. & Gygi, S. P. Combining amine metabolomics and quantitative proteomics of cancer cells using derivatization with isobaric tags. *Anal Chem* **86,** 3585–3593 (2014).

156. Chiang, H. S. *et al.* GEF-H1 controls microtubule-dependent sensing of nucleic acids for antiviral host defenses. *Nat Immunol* **15,** 63–71 (2014).

157. Choi, J. H. *et al.* The FKBP12-rapamycin-associated protein (FRAP) is a CLIP-170 kinase. *EMBO Rep* **3,** 988–994 (2002).

158. Chou, M. F. & Schwartz, D. Biological sequence motif discovery using motif-x. **Chapter 13,** Unit 13.15-13.24.

159. Schwartz, D. & Gygi, S. P. An iterative statistical approach to the identification of protein phosphorylation motifs from large-scale data sets. *Nat Biotechnol* **23,** 1391–1398 (2005).

160. Morton, S., Davis, R. J., McLaren, A. & Cohen, P. A reinvestigation of the multisite phosphorylation of the transcription factor c-Jun. *EMBO J* **22,** 3876–3886 (2003).

161. Peter, M., Nakagawa, J., Doree, M., Labbe, J. C. & Nigg, E. A. In vitro disassembly of the nuclear lamina and M phase-specific phosphorylation of lamins by cdc2 kinase. *Cell* **61,** 591–602 (1990).

162. Waheed, F. *et al.* Extracellular signal-regulated kinase and GEF-H1 mediate depolarization-induced Rho activation and paracellular permeability increase. *Am J Physiol Cell Physiol* **298,** C1376–C1387 (2010).

163. Larsson, N., Marklund, U., Gradin, H. M., Brattsand, G. & Gullberg, M. Control of microtubule dynamics by oncoprotein 18: dissection of the regulatory role of multisite phosphorylation during mitosis. *Mol Cell Biol* **17,** 5530–5539 (1997).

164. Sontag, E., Nunbhakdi-Craig, V., Bloom, G. S. & Mumby, M. C. A novel pool of protein phosphatase 2A Is associated with microtubules and is regulated during the cell cycle. *J Cell Biol* **128,** 1131–1144 (1995).

165. Sontag, J. M., Nunbhakdi-Craig, V., White, C. L. 3rd, Halpain, S. & Sontag, E. The protein phosphatase PP2A/Bα binds to the microtubule-associated proteins Tau and MAP2 at a motif also recognized by the kinase Fyn: implications for tauopathies. *J Biol Chem* **287,** 14984–14993 (2012).

166. Wessel, D. & Flugge, U. I. A method for the quantitative recovery of protein in dilute solution in the presence of detergents and lipids. *Anal Biochem* **138,** 141–143 (1984).

167. Rappsilber, J., Mann, M. & Ishihama, Y. Protocol for micro-purification, enrichment, pre-fractionation and storage of peptides for proteomics using StageTips. *Nat Protoc* **2,** 1896–1906 (2007).

168. Paulo, J. A. *et al.* Effects of MEK inhibitors GSK1120212 and PD0325901 in vivo using 10-plex quantitative proteomics and phosphoproteomics. *Proteomics* **15,** 462–473 (2015).

169. Kaiser, H. F. The varimax criterion for analytic rotation in factor analysis. *Psychometrika* **23,** 187–200 (1958).

170. Akhmanova, A. & Steinmetz, M. O. Tracking the ends: a dynamic protein network controls the fate of microtubule tips. *Nat Rev Mol Cell Biol* **9,** 309–322 (2008).

171. Applegate, K. T. *et al.* plusTipTracker: Quantitative image analysis software for the measurement of microtubule dynamics. *J Struct Biol* **176,** 168–184 (2011).

172. Garrison, A. K. *et al.* Visualization and analysis of microtubule dynamics using dual color-coded display of plus-end labels. *PloS ONE* **7,** e50421 (2012).

173. Sironi, L. *et al.* Automatic quantification of microtubule dynamics enables RNAi-screening of new mitotic spindle regulators. *Cytoskeleton (Hoboken)* **68,** 266–278 (2011).

174. Nishimura, Y., Applegate, K., Davidson, M. W., Danuser, G. & Waterman, C. M. Automated screening of microtubule growth dynamics identifies MARK2 as a regulator of leading edge microtubules downstream of Rac1 in migrating cells. *PloS ONE* **7,** e41413 (2012).

175. Serikbaeva, A., Tvorogova, A., Kauanova, S. & Vorobjev, I. A. Analysis of microtubule dynamics heterogeneity in cell culture. in *Cellular Heterogeneity: Methods and Protocols* (eds. Barteneva, N. S. & Vorobjev, I. A.) **1745,** 181–204 (2018).

176. Lukinavicius, G. *et al.* SiR-Hoechst is a far-red DNA stain for live-cell nanoscopy. *Nat Commun* **6,** 1–7 (2015).

177. Sen, O., Saurin, A. T. & Higgins, J. M. G. The live cell DNA stain SiR-Hoechst induces DNA damage responses and impairs cell cycle progression. *Sci Rep* **8,** (2018).

178. Bollag, D. M. *et al.* Epothilones, a new class of microtubule-stabilizing agents with a Taxol-like mechanism of action. *Cancer Res* **55,** 2325–2333 (1995).

179. Buey, R. M. *et al.* Microtubule Interactions with Chemically Diverse Stabilizing Agents: Thermodynamics of Binding to the Paclitaxel Site Predicts Cytotoxicity. *Chem Biol* **12,** 1269–1279 (2005).

180. Gardner, M. K. *et al.* Rapid microtubule self-assembly kinetics. *Cell* **146,** 582–592 (2011).

181. Schwanhausser, B. *et al.* Global quantification of mammalian gene expression control. *Nature* **473,** 337–342 (2011).

182. Stage, T. B., Bergmann, T. K. & Kroetz, D. L. Clinical pharmacokinetics of paclitaxel monotherapy: An updated literature review. *Clin Pharmacokinet* **57,** 7–19 (2018).

183. Alsharedi, M., Gress, T., Dotson, J., Elmsherghi, N. & Tirona, M. T. Comparison of toxicity profile and tolerability between two standard of care paclitaxel-based adjuvant chemotherapy regimens in breast cancer. *Med Oncol* **33,** 27 (2016).

184. Torvaldson, E., Kochin, V. & Eriksson, J. E. Phosphorylation of lamins determine their structural properties and signaling functions. *Nucleus* **6,** 166–171 (2015).